

**Development of Durable Anti-Wetting and Anti-Fouling Membranes for  
Water Production via Membrane Distillation (MD)**

Tiantian Chen

A Thesis

In the Department

of

Building, Civil and Environmental Engineering

Presented in Partial Fulfillment of the Requirements

for the Degree of

Doctor of Philosophy (Civil Engineering) at

Concordia University

Montreal, Quebec, Canada

August 2021

© Tiantian Chen, 2021

**CONCORDIA UNIVERSITY**  
**SCHOOL OF GRADUATE STUDIES**

This is to certify that the thesis prepared

By: Tiantian Chen

Entitled: Development of Durable Anti-Wetting and Anti-Fouling Membranes for Water Production via Membrane Distillation (MD)

and submitted in partial fulfillment of the requirements for the degree of

**Doctor of Philosophy (Civil Engineering)**

complies with the regulations of the University and meets the accepted standards with respect to originality and quality.

Signed by the final examining committee:

_____	Chair
Dr. Kudret Demirli	
_____	External Examiner
Dr. Xianshe Feng	
_____	External to Program
Dr. Zhibin Ye	
_____	Examiner
Dr. Catherine Mulligan	
_____	Examiner
Dr. Ahmed Soliman	
_____	Thesis Co-Supervisor
Dr. Zhi Chen	
_____	Thesis Co-Supervisor
Dr. Chunjiang An	
_____	Thesis Co-Supervisor
Dr. Saifur Rahaman	

Approved by \_\_\_\_\_  
Dr. Mazdak Nik-Bakht, Graduate Program Director

September 24, 2021 \_\_\_\_\_  
Dr. Mourad Debbabi, Dean  
Gina Cody School of Engineering and Computer Science

## **Abstract**

### **Development of Durable Anti-Wetting and Anti-Fouling Membranes for Water Production via Membrane Distillation (MD)**

**Tiantian Chen, Ph.D.**

**Concordia University, 2021**

Membrane distillation (MD) has gained a growing interest in seawater desalination, wastewater treatment, and separation of volatile compounds as of late due to its low operating pressure, moderate temperature requirements, and high salt rejection. However, membrane fouling and pore wetting are two major problems that hinder maintaining long-term stable flux and salt rejection of MD when treating various feed solutions. Electrospun nanofiber membranes (ENMs) are promising for MD applications due to the discernable advantages of their high hydrophobicity and porosity. Utilization of micro/nano-particles and surface fluoro-silanization are effective modification methods to enhance anti-fouling and anti-wetting properties of MD membranes. The objective of this doctoral research is to develop effective membranes with durable fouling/wetting resistance for water production by MD. To achieve this goal, a highly hydrophobic poly(vinylidene fluoride-co-hexafluoropropylene)/ reduced graphene oxide (PVDF-HFP/ rGO) flat-sheet membrane was prepared via a facile electrospinning technique. The rGO incorporated membranes exhibited excellent stability and durability with a salt rejection of over 99.97% and an average flux of 20.37 kg/m<sup>2</sup>h using 60 g/L sodium chloride as the feed solution. To expand the application of conventional MD membranes to treat challenging wastewaters that contain low surface tension contaminants, one simple modification method was applied by utilizing fluoroalkylsilane of low surface energy on the pristine PVDF-HFP/rGO substrate to achieve surface superamphiphobicity (both superhydrophobicity and near-superoleophobicity). The resulting membranes demonstrated superamphiphobicity, confirmed by their wetting resistance evaluated with water and low surface tension liquids. The antiwetting performance of the membrane was tested through desalinating 35 g/L sodium chloride solution in the presence of a surfactant (sodium dodecyl sulfate, SDS) in the direct contact membrane distillation (DCMD) unit.

Finally, a highly permeable membrane for membrane distillation applications by employing porous MCM-48 silica as the nanofiller was developed. The addition of hydrophobic MCM-48 nanoparticles was found to significantly increase water vapor transport, with a flux enhancement 87.16% greater than that observed in the pristine PVDF-HFP membrane.

**Keywords:** membrane distillation, electrospun nanofiber membranes, superamphiphobicity, MCM-48

## **Acknowledgements**

I would like to express my deepest acknowledgement to my previous supervisor, Dr. Saifur Rahaman, who offers me such a great opportunity to study in Concordia. His skillful guidance, invaluable advice and financial support have encouraged me to move on and make progress throughout my research.

I am also extremely grateful to my present supervisors, Dr. Zhi Chen and Dr. Chunjiang An, for their kind assistance and constructive suggestions during my last stage of research program.

I extend my genuine thanks to the financial support from the Fonds de recherche du Québec – Nature et technologies (FRQNT) and Concordia University through the Faculty Research Support (FRS) program and Graduate Fellowships/Scholarships. Additionally, I appreciate all the financial support from Natural Science and Engineering Research Council of Canada (NSERC) Discovery Grant and NSERC Green-SEAM Network Grant for this work.

I want to express my sincere gratitude to my committee members, Dr. Catherine Mulligan, Dr. Zhibin Ye, Dr. Ahmed Soliman, Dr. Michelle Nokken, and Dr. Xianshe Feng for their time and insightful comments on my thesis.

Moreover, I appreciate all the supports from our technicians, especially Hong Guan and Joseph Hrib for their efforts in the installation of DCMD setup, lab instruments maintenance and repair. I would like to thank all my colleagues and teammates, especially Wen Ma, Sharmin Sultana, Nawrin Anwar, Shahidul Islam for their continuous assistance and encouragement. Finally, my special appreciation also goes out to my family for their unconditional love, understanding, and support all through my studies.

## Table of contents

List of Figures.....	x
List of Tables .....	xv
List of Abbreviations .....	xvi
Chapter 1. Introduction.....	1
1.1 Problem statement.....	1
1.2 Objectives of this study.....	3
1.3 Outline of thesis .....	4
Chapter 2. Literature review .....	6
2.1 Basics and Principles of MD.....	6
2.1.1 Principles and applications of MD.....	6
2.1.2 Membrane characteristics for application in MD .....	7
2.1.3. Membrane fabrication techniques.....	9
2.2 Major challenges in MD separation process.....	10
2.2.1 Membrane fouling.....	10
2.2.2 Membrane wetting.....	11
2.3 Developing membranes for enhanced MD performance .....	12
2.3.1 Electrospun nanofiber membranes (ENMs).....	13
2.3.2 Superhydrophobic membranes.....	16
2.3.3 Superamphiphobic membranes.....	21
Chapter 3. Experimental .....	28
3.1 Materials and chemicals.....	28
3.2 Electrospinning process .....	28
3.3 Characterizations.....	29

3.4 DCMD performance tests .....	31
Chapter 4. Highly Hydrophobic Electrospun Reduced Graphene Oxide (rGO)/PVDF-HFP Membranes for Use in Membrane Distillation .....	33
4.1 Background .....	35
4.2 Materials and methods .....	37
4.2.1 Materials and chemicals.....	37
4.2.2 Electrospun membrane preparation .....	37
4.2.3 Membrane characterization.....	38
4.2.4 Porosity .....	38
4.2.5 Membrane performance evaluation (DCMD Performance) .....	38
4.3 Results and discussion .....	39
4.3.1 Membrane morphology.....	39
4.3.2 Successful incorporation of rGO investigated by Raman spectra, TGA, and XPS analysis.....	40
4.3.3 Contact angle and liquid entry pressure of water (LEPw).....	43
4.3.4 Porosity, Pore size, Pore size distribution.....	44
4.3.5 DCMD performance (short-term).....	46
4.3.6 Long-term stability.....	48
4.3.7 Reported permeate flux and salt rejection of different electrospun nanofibrous membranes used for desalination.....	49
4.3.8 Proposed mechanism for enhanced stability of rGO incorporated membrane .....	50
4.4 Summary .....	51
Chapter 5. Development of Robust and Superamphiphobic Membranes using Reduced Graphene Oxide (rGO)/PVDF-HFP Nanocomposite Mats for Membrane Distillation .....	52
5.1 Background.....	54

5.2 Materials and methods .....	56
5.2.1 Chemicals and materials .....	56
5.2.2 Preparation of superamphiphobic nanofibrous membranes.....	56
5.2.3 Membrane characterization.....	57
5.2.4 Stability of surface coating .....	58
5.2.5 Membrane distillation experiments.....	58
5.3 Results and discussion .....	60
5.3.1 The effect of POTS coating on membrane surface morphology .....	60
5.3.2 Successful POTS functionalization confirmed by XPS and FTIR spectra .....	61
5.3.3 Evaluation of wettability and robustness of the membranes.....	64
5.3.4 Membrane properties and DCMD performance .....	69
5.4 Summary.....	75
Chapter 6. Mesoporous MCM-48 Silica Nanospheres Incorporated PVDF-HFP Membrane with Highly Enhanced Permeate Flux in Membrane Distillation Process.....	77
6.1 Background.....	79
6.2 Materials and methods .....	81
6.2.1 Chemicals and materials .....	81
6.2.2 Preparation of functionalized MCM-48 nanoparticles.....	81
6.2.3 Preparation of pristine PVDF-HFP and hybrid PVDF-HFP/MCM-48 electrospun nanofibrous membranes.....	82
6.2.4 Characterization methods.....	82
6.2.5 Direct contact membrane distillation experiments.....	83
6.3 Results and discussion .....	84
6.3.1 Characterization of MCM-48 nanoparticles .....	84
6.3.2 Characterization of hybrid membranes.....	89

6.3.3 Enhancement of gas permeability and DCMD performance of hybrid membranes....	95
6.3.4 Proposed mechanism of water vapor permeation through the hybrid membrane.....	98
6.3.5 Long-term stability of the PVDF-HFP/MCM-48 hybrid membrane.....	99
6.4 Summary.....	99
Chapter 7 Conclusions, contributions and future work.....	101
7.1 Conclusions.....	101
7.2 Contributions.....	103
7.3 Future work.....	103
References.....	105
Appendices.....	125

## List of Figures

<b>Figure 1. 1</b>	Contributions of desalination techniques around the world. <sup>6</sup> .....	2
<b>Figure 2. 1</b>	Schematic representation of the direct contact membrane distillation process. <sup>16</sup> .....	6
<b>Figure 2. 2</b>	The fouling sites on a membrane can be divided into surface fouling (external) or pore blocking (internal). <sup>32</sup> .....	11
<b>Figure 2. 3</b>	A schematic presentation of various forms of membrane wettability in MD process: (A) non-wetted; (B) surface-wetted; (C) partial-wetted; and (D) fully-wetted. <sup>38</sup> .....	12
<b>Figure 2. 4</b>	Typical electrospinning set-up consisting of nozzle, high voltage power supply, and grounded collector. <sup>40</sup> .....	14
<b>Figure 2. 5</b>	(A) Leaves with water droplets on them, (B) Scanning electron microscopy of a Lotus leaf microstructure. <sup>47,48</sup> .....	17
<b>Figure 2. 6</b>	General scheme of membrane fabrication using the dip-coating technique. <sup>54</sup> .....	19
<b>Figure 2. 7</b>	Schematic of layer-by-layer technique. <sup>57</sup> .....	20
<b>Figure 2. 8</b>	Schematic mechanism of silanization reaction. <sup>59</sup> .....	21
<b>Figure 2. 9</b>	Schematic illustration of a droplet placed onto (A) a flat substrate and (B, C) rough substrates. Depending on the roughness of the surface, the droplet is either in the so-called (B) Wenzel regime or the (C) Cassie-Baxter regime. (D) A surface with the re-entrant structure. <sup>64</sup> ....	23
<b>Figure 2. 10</b>	Two strategies towards the fabrication of superamphiphobic surfaces: pre-roughening + post-fluorination and pre-fluorination + post-roughening.....	24
<b>Figure 3. 1</b>	Setup for LEP measurements: (1) nitrogen cylinder, (2) pressured container, (3) membrane cell, (4) pressure regulator, (5) pressure meter, and (6) outlet.....	30
<b>Figure 3. 2</b>	Schematic diagram of the DCMD set-up.....	32
<b>Figure 4. 1</b>	Graphical Abstract.....	34
<b>Figure 4. 2</b>	SEM images for (A) PVDF-HFP, (B) PVDF-HFP-rGO membranes and corresponding diameter distribution of nanofibers (C and D).....	40
<b>Figure 4. 3</b>	Raman spectra of pure PVDF-HFP and PVDF-HFP-rGO membrane.....	41

<b>Figure 4. 4</b> TGA analysis of pure PVDF-HFP and PVDF-HFP-rGO membrane.....	42
<b>Figure 4. 5</b> (A) XPS survey scans and (B) F/C, O/C ratio of pure PVDF-HFP, PVDF-HFP-rGO membrane.....	43
<b>Figure 4. 6</b> Comparison of contact angle and LEPw of pure PVDF-HFP, PVDF-HFP-rGO membrane.....	44
<b>Figure 4. 7</b> Porosity of pure PVDF-HFP and PVDF-HFP-rGO membrane.....	45
<b>Figure 4. 8</b> Comparison of pore size distribution of (A) PVDF-HFP and (B) PVDF-HFP-rGO membrane.....	46
<b>Figure 4. 9</b> (A) Permeate flux versus time for the PVDF-HFP-rGO membrane (with a thickness of 390 $\mu\text{m}$ ) under a temperature difference of 35 $^{\circ}\text{C}$ and 50 $^{\circ}\text{C}$ . (B) Permeate flux versus time for PVDF-HFP-rGO membranes with different thicknesses (150 $\mu\text{m}$ and 390 $\mu\text{m}$ ). Feed water was 60 g/L NaCl solution circulated at 0.75 LPM with a feed temperature of 75 $^{\circ}\text{C}$ and a distillate temperature of 25 $^{\circ}\text{C}$ . (C) Pure water flux versus time for the pure PVDF-HFP, PVDF-HFP-rGO membrane ( $\Delta T=50$ $^{\circ}\text{C}$ ). Feed water was 60 g/L NaCl solution circulated at 0.75 LPM with a feed temperature of 75 $^{\circ}\text{C}$ and a distillate temperature of 25 $^{\circ}\text{C}$ .....	48
<b>Figure 4. 10</b> (A) Flux and (B) permeate conductivity vary with operating time in long-term DCMD experiments. Feed water was 60 g/L NaCl solution circulated at 0.75 LPM with a temperature of 75 $^{\circ}\text{C}$ , the distillate temperature was 25 $^{\circ}\text{C}$ with the flow rate of 0.75 LPM.....	49
<b>Figure 4. 11</b> Schematic of proposed mechanism for PVDF-HFP-rGO membrane.....	51
<b>Figure 5. 1</b> Graphical Abstract.....	53
<b>Figure 5. 2</b> The schematic procedure for preparation of PH-rGO-POTS functionalized membranes through a dip-coating strategy. The PH-rGO electrospun nanofibrous mat was immersed in a mixture of POTS and ethanol for 36 h, followed by thermal treatment at 120 $^{\circ}\text{C}$ for 4 h after rinsing with deionized water. ....	57
<b>Figure 5. 3</b> SEM images and corresponding fiber diameter distribution of (A, C) PH-rGO and (B, D). PH-rGO-POTS membranes.....	61
<b>Figure 5. 4</b> (A) XPS survey and (B) FTIR spectra of the pristine PH-rGO and the PH-rGO-POTS membranes.....	62

<b>Figure 5. 5</b> The cross-sectional EDS mapping images of Si element on the PH-rGO-POTS membrane.....	63
<b>Figure 5. 6</b> XPS O1s spectra of (A) pristine membrane and (B) PH-rGO-POTS membrane.....	64
<b>Figure 5. 7</b> Contact angle profile of water and diiodomethane drops on the PH-rGO and the PH-rGO-POTS membranes.....	65
<b>Figure 5. 8</b> (A) Non-sticky test, PH-rGO-POTS membrane was inserted into dye solution and then taken out. (B) The roll-off behavior of the water droplets on the PH-rGO-POTS membrane at the horizontal state. (C) Self-cleaning behavior of the PH-rGO-POTS membrane.....	66
<b>Figure 5. 9</b> Contact angles of the PH-rGO-POTS membrane facing with different water-ethanol mixtures. “Wicking” means that the membrane was wetted by the testing liquids immediately, and no stable contact angles could be measured. The error bars stand for the standard deviations of contact angle measurements. The water-ethanol mixtures with different surface tensions are prepared following a published protocol. <sup>164</sup> .....	67
<b>Figure 5. 10</b> Water contact angle (black) and Diiodomethane contact angle (red) of PH-rGO-POTS membranes after challenging with (A) boiling water for 4h, (B) sonication for 60 min, (C) strong acid (HCl, pH=2) for 110 h, and (D) base solution (NaOH, pH=12) for 110 h. The error bars in the figures stand for standard deviation. Insets are optical photos of PH-rGO-POTS membranes after various treatments.....	69
<b>Figure 5. 11</b> The LEP value for the membrane samples in this work.....	70
<b>Figure 5. 12</b> (A) Water flux of the PH-rGO-POTS membranes under various temperature differences; the temperature of the feed varied from 35 °C to 65 °C, while the permeate side was kept as constant, 15.0 °C. (B) Water flux of the PH-rGO-POTS membrane under different NaCl concentrations with the temperature difference maintained at 50 °C. The error bars in the figures stand for standard deviation. The flow rate of feed and permeate streams were both 0.75 LPM. ....	71
<b>Figure 5. 13</b> (A) Water flux and (B) permeate conductivity of PH-rGO (unmodified substrate), PH-POTS (control), and PH-rGO-POTS membranes in DCMD. A 3.5 wt% NaCl solution with increased addition of SDS from 0.1 mM to 0.3 mM was used as feed solution maintained at 65 °C and deionized water was used as a permeate cooling solution maintained at 15 °C. (C) Long-term	

stability of PH-rGO-POTS membranes in the presence of mixed foulants (35 g/L NaCl, 20 mM CaCl<sub>2</sub>, 20 mM Na<sub>2</sub>SO<sub>4</sub>, 100 mg/L humic acid sodium salt, 10 mg/L machine oil and 0.05 mM SDS). The flow rate of feed and permeate streams were both 0.75 LPM.....72

**Figure 5. 14** (A) Contact angles of the PH-POTS membrane with different ethanol concentrations. (B) Diiodomethane contact angle (grey) and LEP (blue) of the PH-POTS membrane.....74

**Figure 6. 1** Graphical Abstract.....78

**Figure 6. 2** Schematic representation of synthesis of MCM-48 nanospheres.....81

**Figure 6. 3** (A, D, G) SEM images, (B, E, H) TEM images and (C, F, I) particle size distribution of prepared MCM-48 nanoparticles using various amounts of F127 as the particle dispersion agent. ....85

**Figure 6. 4** (A) FTIR spectroscopy for the bare and modified nanoparticles. The contact angle image of the silica nanoparticle (B) before and (C) after modification.....88

**Figure 6. 5** The detailed microstructure of the fabricated membranes. (A, B, C, D) Surface morphology of the fabricated membranes visualized by SEM and probed by AFM (inset). (E) High-magnification TEM image of pristine PVDF-HFP membrane. (F, G, H, I) HAADF-STEM images of PVDF-HFP/MCM-48 hybrid membrane with the corresponding STEM-EDS mapping analysis (J, L, K, M, N). ....90

**Figure 6. 6** Fiber diameter distribution of the electrospun nanofibrous membranes (A) Pristine and (B) Hybrid membrane. ....91

**Figure 6. 7** TGA profile for bare, vinyl- MCM-48.....92

**Figure 6. 8** FTIR spectroscopy for pristine and hybrid membranes.....93

**Figure 6. 9** (A) Small-angle XRD patterns of synthesized nanoparticles, and (B) the wide-angle XRD patterns of different membranes. Inset image shows the small-angle XRD patterns of the respective samples.....94

**Figure 6. 10** Water contact angle of the pristine and hybrid membranes.....95

**Figure 6. 11** (A) Gas permeability of electrospun membranes at different applied pressures and (B) mean pore size of the pristine and hybrid membranes.....96

**Figure 6. 12** Water flux of pristine and hybrid membranes in DCMD process. A 35g/L NaCl solution was used as feed solution maintained at 55 °C and deionized water was used as a permeate cooling solution maintained at 15 °C. The flow rate of feed and permeate streams were both 0.7 LPM.....97

**Figure 6. 13** Long-term stability of PVDF-HFP/MCM-48 hybrid membranes using (A) a 35 g/L NaCl solution and (B) a mixture of 35 g/L NaCl + 1.26 g/L CaCl<sub>2</sub> with the feed solution maintained at 55 °C and deionized water as the cooling solution maintained at 15 °C. The flow rate of feed and permeate streams were both 0.7 LPM.....99

## List of Tables

<b>Table 2. 1</b> Characteristic properties of commercial polymer materials commonly used for MD membranes. <sup>27</sup> .....	9
<b>Table 2. 2</b> Effect of solution, process and other parameters on the fiber formation during electrospinning .....	15
<b>Table 4. 1</b> Comparison with different electrospun nano-fibrous membranes used for desalination. ....	50
<b>Table 5. 1</b> Elemental composition of resultant membranes .....	62
<b>Table 5. 2</b> Comparison of amphiphobic membranes for membrane distillation .....	75
<b>Table 6. 1</b> Structural parameters of MCM-48 nanoparticles using different amounts of F127.....	86
<b>Table 6. 2</b> Comparisons of flux enhancement between the current work and reference studies. ....	98

## List of Abbreviations

MD	Membrane distillation	NPs	Nanoparticles
ENMs	Electrospun nanofiber membranes	CNTs	Carbon nanotubes
PVDF- HFP	Poly (vinylidene fluoride-co-hexafluoropropylene)	Ag	silver
rGO	reduced Graphene Oxide	TiO <sub>2</sub>	Titanium dioxide
SDS	Sodium dodecyl sulfate	WCA	Water contact angle
DCMD	direct contact membrane distillation	DC	Direct current
FRQNT	Fonds de recherche du Québec – Nature et technologies	AC	Alternative current
FRS	Faculty Research Support	RF	Radiofrequency
NSERC	Natural Science and Engineering Research Council of Canada	MW	Microwave
MED	Multi-effect distillation	CVD	Chemical vapor deposition
MSF	Multi-stage flash	LBL	Layer-by-layer
MVC	Mechanical vapor compression	POSS	Polyhedral oligomeric silsesquioxane
RO	Reverse osmosis	UF	Ultrafiltration
NF	Nanofiltration	HFP	Hexafluoropropene
ED	Electrodialysis	TEP	Triethyl phosphate
FO	Forward osmosis	GO	Graphene oxide
PRO	Pressure retarded osmosis	LEPw	Liquid entry pressure of water
MF	Microfiltration	DMAc	Dimethylacetamide
LEP	Liquid entry pressure	SEM	Scanning electron microscopy
POTS	Perfluorooctyltriethoxysilane	XPS	X-ray photoelectron spectroscopy
AGMD	Air gap membrane distillation	TGA	Thermal gravimetric analysis

VMD	Vacuum membrane distillation	CFP	Capillary flow porometer
SGMD	Sweeping gas membrane distillation	PMI	Porous Materials Inc.
PP	Polypropylene	Pd	Palladium
PTFE	Polytetrafluoroethylene	Si	Silicon
PVDF	Polyvinylidene fluoride	SiNPs	Silica nanoparticles
PSD	Pore size distribution	FDTS	Perfluorodecyltrichlorosilane
TIPS	Thermally induced phase separation	TEOS	Tetraethyl orthosilicate
NIPS	Nonsolvent induced phase separation	C <sub>2</sub> H <sub>5</sub> OH	Ethyl alcohol
VIPS	Vapor induced phase separation	NH <sub>4</sub> OH	Ammonium hydroxide
CaCO <sub>3</sub>	Calcium carbonate	CaCl <sub>2</sub>	Calcium chloride
CaSO <sub>4</sub>	Calcium sulfate	NaSO <sub>4</sub>	Sodium sulphate
CA	Cellulose acetate	NaCl	Sodium chloride
PVA	Poly(vinyl alcohol)	EDS	Energy-dispersive X-ray spectroscopy
PAN	Polyacrylonitrile	FTIR	Fourier transform infrared spectroscopy
PET	Polyethylene terephthalate	ATR	Attenuated total reflectance
PS	Polystyrene	ΔT	Temperature difference
Psf	Polyether sulfone	VTEOS	Vinyltriethoxysilane
PU	Polyurethane	CTAB	Cetyltrimethylammonium bromide
HAADF	High-angle annual dark field	STEM	Scanning transmission electron microscopy
AFM	Atomic force microscope	BET	Brunauer-Emmett-Teller
LPM	Liter per minute	TEM	Transmission electron microscopy

# Chapter 1. Introduction

## 1.1 Problem statement

The global shortage of fresh water, due to increasing industrialization, urbanization, climate change and human population growth, greatly impacts the quality of life. At present, over 1.1 billion people have a limited access to potable water and are suffering from the corresponding adverse effects.<sup>1</sup> Efficient and cost-effective approaches to produce fresh water for human consumption and irrigation are urgently needed and have been researched extensively in response to the growing demand.<sup>2</sup> Desalination and water reuse are considered as reliable methods to alleviate water scarcity by augmenting alternative water resources, such as seawater, brackish water, wastewater, and other impaired waters.<sup>3</sup>

Currently, the most widely applied desalination technologies can be classified into two types: thermal (phase change) and membrane-based processes (**Figure 1.1**).<sup>4</sup> Thermal processes are based on the principles of evaporation and condensation. Simply put, water is heated to the evaporation state, then the salts are removed while clean water is produced through the water vapor condensation.<sup>5</sup> Conventional processes include multi-effect distillation (MED), multi-stage flash (MSF), and mechanical vapor compression (MVC). The membrane separation technology uses a semi-permeable membrane to separate water from solutes. Reverse osmosis (RO), nanofiltration (NF), and electrodialysis (ED) are the most common used membrane processes. Particularly, RO accounts for 69% of the desalination plants worldwide.<sup>6</sup>

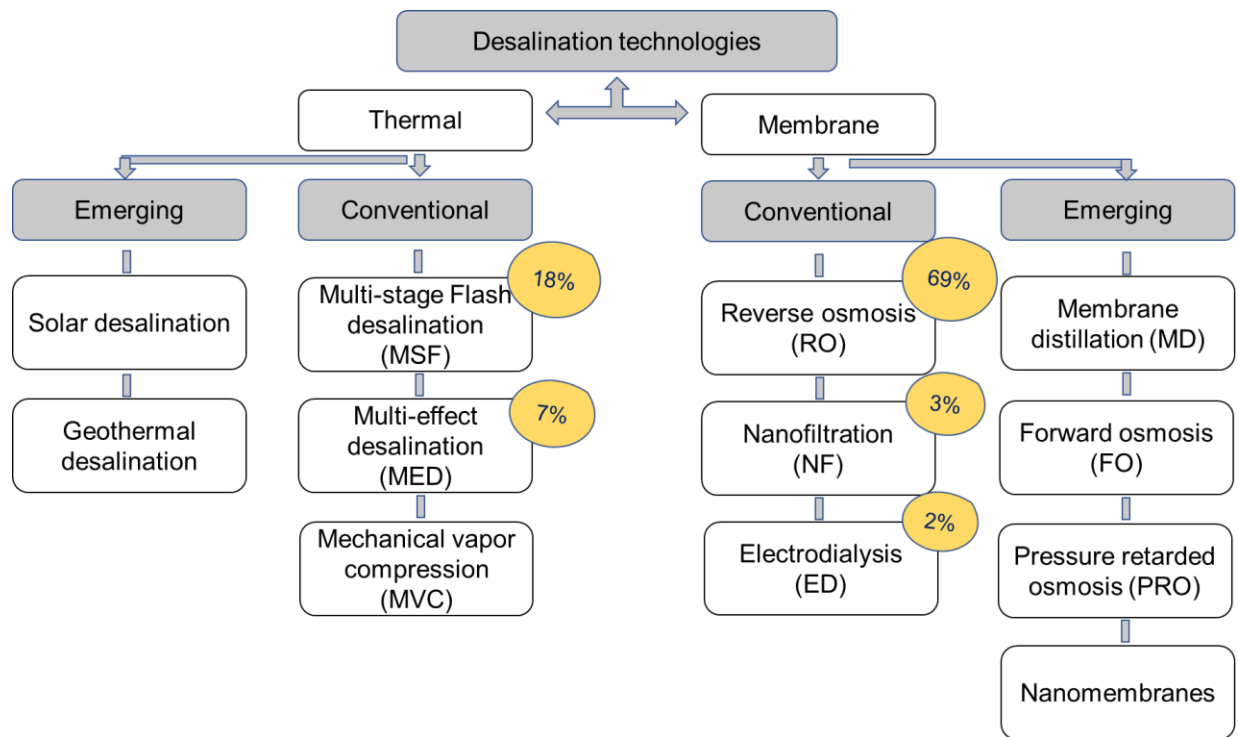


**Figure 1. 1** Contributions of desalination techniques around the world.<sup>6</sup>

However, conventional desalination technologies are energy intensive and are ultimately linked to fossil fuels which are non-renewable and diminish fast. Energy consumption generally amounts to 50%–60% of the total water costs for the RO process.<sup>7</sup> In addition, many kinds of industrial wastewater which always have very high salinity pose a challenge to the present popular technologies.<sup>8</sup>

MD is expected to be a promising substitute for conventional treatment processes. MD is an emerging thermally driven, membrane-based technology to produce fresh water effectively and efficiently. In the MD process, a hydrophobic microporous membrane is used to only allow vapor molecules passing through. The driving force for MD separation is a partial vapor pressure gradient across the membrane, typically deriving from the temperature differential between the hot feed and cold permeate streams.<sup>9</sup> MD is particularly suitable to desalinate highly saline brines where the salinity is beyond the practical limit of RO (~70,000 ppm), such as RO brines, coal seam gas water, and shale gas/oil produced wastewater, due to its relative insensitivity to salt concentration and a theoretical 100% salt rejection.<sup>10</sup> Low working temperature (40-85 °C) distinguishes MD

from conventional thermal distillation (60-110 °C), making it possible to utilize low-grade heat sources, such as waste heat or solar thermal energy, significantly reduces the cost.<sup>11</sup>

Despite such attractive advantages, MD is still in an early developmental stage and has not been widely applied in industrial and commercial settings. One of the major difficulties in MD processes is the lack of appropriate MD membranes. Hydrophobic microfiltration (MF) membranes are widely used in the field of MD. However, these membranes are not specifically optimized for MD as they always suffer from low flux, insufficient wetting resistance, and high fouling/scaling tendency. Membrane fouling is generally caused by attachment of humic acid, proteins, and oily substances onto the hydrophobic membrane through hydrophobic-hydrophobic interactions. Moreover, deposition of inorganic species (scaling) will cause further complications. Membrane wetting is another challenge that affects stable desalination performance of MD membranes. This phenomenon occurs when the trans-membrane pressure exceeds the liquid entry pressure (LEP), which is affected by liquid surface tension, membrane hydrophobicity, pore size, and pore shape.<sup>12</sup> In addition, conventional hydrophobic microporous membranes used in MD processes can be easily wetted by low surface tension contaminants (i.e., oil, alcohols, and surfactants) which often present in highly saline industrial waste streams, contaminating the distillate and jeopardizing water treatment quality.

Many approaches have been employed to cope with the above issues, such as, engineering amphiphobic surfaces, fabricating composite hydrophobic/hydrophilic membranes, and blending with functional inorganic fillers. However, those attempts always involve multiple steps, usage of special equipment (e.g., chemical vapor deposition reactors and plasma chambers), time-consuming modifications.<sup>13,14</sup> And the resulted membranes exhibit limited stabilities and low flux. Therefore, this study is focused on the development of novel membrane materials and fabrication techniques, as well as surface modification methods for water production via MD. Major efforts have been made to improve the membrane permeability, fouling and wetting resistance.

## **1.2 Objectives of this study**

As summarized above, membrane distillation (MD) is a promising thermally driven, membrane-based technology as an effective and efficient separation approach to produce fresh water in zero liquid discharge. Particularly, MD is suitable to desalinate hypersaline solutions, such as RO brine

and shale gas produced wastewater owing to its insensitivity to salts concentration and 100% theoretical salt rejection. Currently, there is a lack of appropriate MD membranes. Hydrophobic microfiltration (MF) membranes developed through phase inversion and stretching processes are widely used in the field of MD. However, these membranes are not specifically optimized for MD. This research aims to develop practically applicable, effective and durable membranes for the application in MD treating various kinds of feed solutions. In particular, the following aspects are comprehensively investigated:

- (1) Evaluation of inorganic fillers incorporated composite membranes on the membrane hydrophobicity and anti-wetting properties in the treatment of hypersaline solutions.
- (2) Exploration of superamphiphobic membranes via surface modifications on the substrate and their effectiveness in the challenging wastewaters disposal.
- (3) Application of mesoporous silica nanoparticles in the fabrication of high permeable membranes.

### **1.3 Outline of thesis**

Chapter 2 reviews the principles, applications, and major challenges of MD process. Membrane materials, fabrication techniques, and modification strategies for MD application are also introduced.

Chapter 3 presents the fabrication and characterization of highly hydrophobic electrospun reduced graphene oxide (rGO)/PVDF-HFP membranes. The effect of rGO incorporation on membrane surface morphology, physicochemical properties (e.g., contact angle, liquid entry pressure, pore size) and separation performance was evaluated. Long-term stability of fabricated membranes was investigated through a direct contact membrane distillation (DCMD) process using the feed solution with high salinity (60 g/L sodium chloride).

Chapter 4 demonstrates the facile superamphiphobicity modification on the nanofibrous substrate to render the necessary chemical and physical properties for anti-wetting performance. Low surface energy fluoroalkylsilane perfluorooctyltriethoxysilane (POTS) was selected as the modifier and coated on the nanocomposite membrane through a simple dip-coating process. The superamphiphobic stability was challenged in various treatment scenarios. Anti-wetting properties

were compared with control membranes using a model surfactant (sodium dodecyl sulfate, SDS) -containing saline solution as the feed.

Chapter 5 describes the application of mesoporous MCM-48 silica nanospheres as the nanofiller to enhance MD membrane permeability. MCM-48 silica nanoparticles with controlled particle sizes were prepared under mild conditions and hydrophobilized with vinyl groups. A novel hybrid PVDF-HFP/MCM-48 electrospun nanofibrous membrane was obtained by incorporating vinyl-modified MCM-48 nanoparticles into the PVDF-HFP polymer matrix. The addition of hydrophobic MCM-48 nanoparticles was found to significantly increase water vapor transport. Not only is this the first attempt to fabricate PVDF-HFP/MCM-48 nanofibrous membranes by electrospinning, but also the first to employ MCM-48 based membranes in MD processes.

Chapter 6 outlines the contributions and conclusions of this thesis. Limitations of this work and recommendations for future research are also presented.

## Chapter 2. Literature review

### 2.1 Basics and Principles of MD

#### 2.1.1 Principles and applications of MD

MD is a thermally driven separation process, in which only vapor molecules are able to pass through a porous hydrophobic membrane. This separation process is driven by the vapor pressure differences existing across the porous hydrophobic membrane surfaces.<sup>15</sup>

As illustrated in **Figure 2.1**, the hydrophobic nature of the MD membrane prevents the feed liquid from entering the membrane pores due to surface tension. First initiated by evaporation of the feed liquid at the phase boundary, the volatile components in the hot feed vaporize and then diffuse across the dry membrane pores. The vapors then condense on the permeate side.<sup>16</sup>

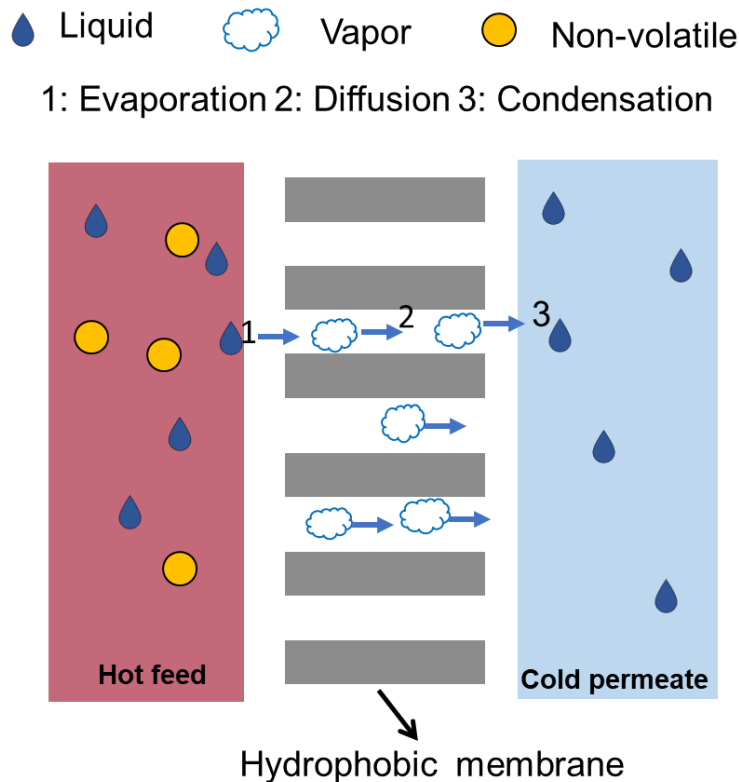


**Figure 2. 1** Schematic representation of the direct contact membrane distillation process.<sup>16</sup>

The possible configurations of MD process are divided into four types depending on the way the permeate side is processed: direct contact membrane distillation (DCMD), air gap membrane

distillation (AGMD), vacuum membrane distillation (VMD), and sweeping gas membrane distillation (SGMD).<sup>17</sup> Each configuration has its own advantages and disadvantages, however, DCMD is the most studied configuration in the lab due to its simplicity in both design and operation.<sup>18</sup>

Compared with other membrane separation processes, the main competitive advantages of MD are as follows:<sup>19</sup> (1) Theoretically, a 100% rejection of inorganic ions, macromolecules, and other non-volatile compounds; (2) Relatively low operating temperatures below the normal boiling point of the feed solution (40-85 °C); (3) Lower operating pressures than conventional pressure-driven membrane separation processes; (4) Insensitivity to feed concentration for seawater desalination; and (5) Potential to utilize low grade heat such as solar energy or waste heat.

MD was originally utilized in desalination processes as an alternative to RO and other thermal desalination techniques.<sup>20</sup> Then, with a better understanding of the heat and mass transfer principles due to research over the last decade, MD processes have received worldwide attention from both academia and industry because of its unique advantages. Many other interesting applications of MD have been proposed, such as removal of boron and arsenic from aqueous solutions, wastewater treatment, separation of volatile compounds, concentration of fruit juices, production of chemicals, and in medical procedures.<sup>21,22</sup>

### **2.1.2 Membrane characteristics for application in MD**

The role of the membrane design and structure is crucial for high efficiency MD processes. An optimized membrane specifically designed for MD could further improve the performance. In particular, the ideal characteristics needed for membranes are as follows:

#### **(1) Surface hydrophobicity**

A hydrophobic medium is a requisite according to the definition of the MD process. Highly hydrophobic materials only allow vapor to pass, preventing water from wetting the inside of the membrane. The currently available membranes used commercially and in academic research are made mainly of polypropylene (PP), polytetrafluoroethylene (PTFE), and polyvinylidene fluoride (PVDF).<sup>23</sup> The surface could be made hydrophobic by using materials with a low surface energy or by modifying the surface into rougher surfaces with hierarchical nanostructure surface morphology.<sup>24</sup>

## (2) Thickness

In MD, permeate flux is inversely proportional to the membrane thickness. However, while mass transfer is improved by reducing the membrane thickness, more heat loss also occurs, thereby reducing the driving force. Hence, an optimal thickness exists, balancing mass transport (permeate flux) and driving force (heat efficiency), which is always larger for higher salinity feed water.<sup>25,26</sup>

## (3) Membrane pore size and pore size distribution (PSD)

Permeate flux increases proportionally with increases in pore size. However, small pore size is needed to avoid pore wetting. Thus, an optimal pore size has to be balanced in terms of high permeate flux and effective pore wetting resistance. Pore sizes for MD membranes usually range from 100 nm to 1  $\mu\text{m}$ .<sup>27</sup> Some studies indicate PSD should be as narrow as possible to enhance MD performance while others conclude PSD has little effect on the flux.<sup>28</sup>

## (4) Liquid entry pressure (LEP)<sup>29</sup>

LEP is the minimum transmembrane pressure where liquids will penetrate the pores of the membrane. To avoid MD pore wetting, the hydrostatic pressure must be lower than the LEP. However, even though the operating pressure is lower than the LEP, pore wetting can still occur when fouling occurs at the membrane surface. In MD process, the LEP should be maintained as high as possible. The LEP value depends mainly on the material hydrophobicity and membrane pore size (Cantor–Laplace equation 2-1).

$$\text{LEP} = (-4B_g \sigma \cos \theta) / d_{\max}$$

where LEP is the liquid entry pressure of pure water in Pa,  $B_g$  is a pore geometric factor,  $\sigma$  is the surface tension of the solution ( $\text{N m}^{-1}$ ),  $\theta$  is contact angle in degrees between the solution and membrane surface,  $d_{\max}$  is the largest pore size in m.

## (5) Porosity<sup>30</sup>

Higher porosity results in less conductive heat loss through the membrane, therefore, a higher driving force, higher flux, and higher energy efficiency can be achieved. However, high porosity membranes with low mechanical strength tend to degrade under even mild operation pressure, resulting in the decline of membrane performance. The recommended porosity value is 80-90%.

## (6) Thermal conductivity<sup>31</sup>

High thermal conductivities increase heat transfer and reduce vapor flux due to reduced interface temperature differences; therefore, the thermal conductivity of the membrane should be minimal. Membranes with high porosity and thickness tend to have lower thermal conductivity. The standard values of membrane materials used in MD range from 0.04 to 0.06  $\text{W}\cdot\text{m}^{-1}\cdot\text{K}^{-1}$ .

### 2.1.3. Membrane fabrication techniques

Hydrophobic microfiltration (MF) membranes are widely used in the field of MD. Stretched and phase inverted membranes are both commercially available for this purpose. However, these membranes are not specifically optimized for MD, which usually have large pores and low porosity, consequently suffering from low permeate flux, although optimization is expected to dramatically improve the process performance. Among the materials investigated or utilized for MD membranes, hydrophobic polymers are preferred due to their easy fabrication, modification, and scale-up as well as their low costs. Different fabrication processes, such as phase inversion including thermally induced phase separation (TIPS), nonsolvent induced phase separation (NIPS) and vapor induced phase separation (VIPS), melt extrusion stretching, sintering, and electrospinning have been developed for the fabrication of MD membranes (see **Table 2.1**).<sup>21</sup>

**Table 2. 1** Characteristic properties of commercial polymer materials commonly used for MD membranes.<sup>27</sup>

Polymer	Surface energy (*10 <sup>-3</sup> Nm <sup>-1</sup> )	Thermal conductivity (W·m <sup>-1</sup> ·K <sup>-1</sup> )	Thermal stability	Chemical stability	Fabrication methods
PTFE	9 - 20	0.25	Good	Good	Sintering Melt-extrusion
PP	30	0.17	Moderate	Good	Melt-extrusion TIPS
PVDF	30.3	0.19	Moderate	Good	NIPS, TIPS Electrospinning

## 2.2 Major challenges in MD separation process

Despite the potential of MD in the production of clean water, membrane fouling and wetting are major obstacles in the widespread use of this separation technology. Fouling is a serious problem that will affect MD performance and can cause major damages and costs in the MD process, especially in long-term operation. In addition to fouling, membrane wetting is another challenge that affects stable flux performance and salt rejection.

### 2.2.1 Membrane fouling

Fouling, in general, is the accumulation of unwanted deposits on the surface - or inside the pores - of the membrane that degrades its permeation flux performance. Fouling can take place both externally and internally (see **Figure 2.2**).<sup>32</sup> External fouling refers to the formation of deposits on the outer surface, while internal fouling occurs when foulant deposits are formed inside the pores of the membrane.

The foulants found in MD process can be divided into inorganic, organic, and biological foulants.<sup>33</sup> Inorganic fouling - usually termed as scaling - is the most studied fouling as it is one of the major challenges that hinder the full-scale operation of MD for desalination.<sup>34</sup> The three most common scalants in MD are calcium carbonate ( $\text{CaCO}_3$ ), calcium sulfate ( $\text{CaSO}_4$ ), and silicate. In real MD processes, a mixed fouling is most likely to occur. Fouling mechanisms depend on several factors, such as solution characteristics of feed waters, membrane surface properties, foulant properties, and operational conditions.<sup>35</sup>

Fouling may cause partial membrane wetting or severe membrane damage. It has also been reported that fouling deposits can lower the hydrophobicity of the surface.<sup>36</sup>

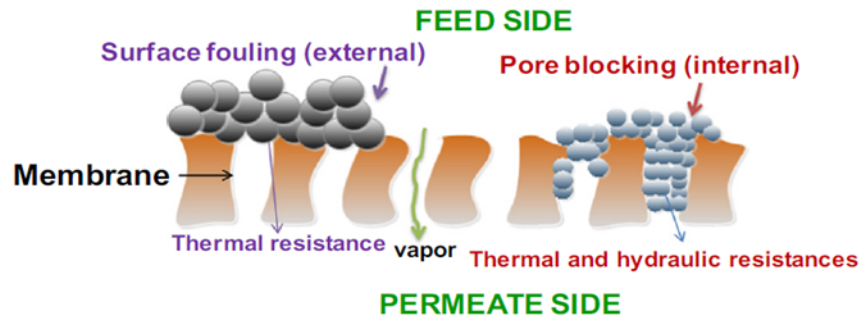


**Figure 2. 2** The fouling sites on a membrane can be divided into surface fouling (external) or pore blocking (internal).<sup>32</sup>

Currently, pre-treatment and membrane cleaning are the main techniques to control fouling.<sup>37</sup> Developing anti-fouling membranes has also been utilized to mitigate membrane fouling and will be discussed in detail in the following section 2.3.

### 2.2.2 Membrane wetting

In addition to fouling, membrane wetting is another obstacle that may lead to long-term MD operation inefficiency. As shown in **Figure 2.3**, there are four different degrees of membrane wetting:<sup>38</sup> (1) non-wetted, (2) surface wetted, (3) partial-wetted, and (4) fully-wetted. Surface wetting (**Figure 2.3 B**) happens at the surface of the membrane, with the membrane maintaining a gap for the vapor to pass through, where the vaporization process can proceed to the permeate side. Under this degree of wetting, no leakage of feed occurs, thus high-quality distillate can be produced. In the case of partial wetting (**Figure 2.3 C**), some portions of the membrane are open for water to pass through, while other pores have decreased gaps for water vapor. Therefore, a decreased water purity will occur in the permeate side. The MD process may continue until large areas of open pores occur. Fully-wetted membranes (**Figure 2.3 D**) leads to complete MD performance inefficiency and low quality permeate is formed as the feed just flows through the membrane.

As mentioned before, LEP is the critical pressure at which the liquid starts to penetrate the pores of the membrane, which is a quantitative measure of wettability. To avoid membrane wetting, a membrane material with higher LEP is preferred. Increasing the contact angle using hydrophobic

or superhydrophobic materials, or reducing pore sizes, are effective methods. Fouling is the main cause of pore wetting; however, some factors such as the presence of surfactants in the solution can also increase membrane wetting.<sup>38</sup>

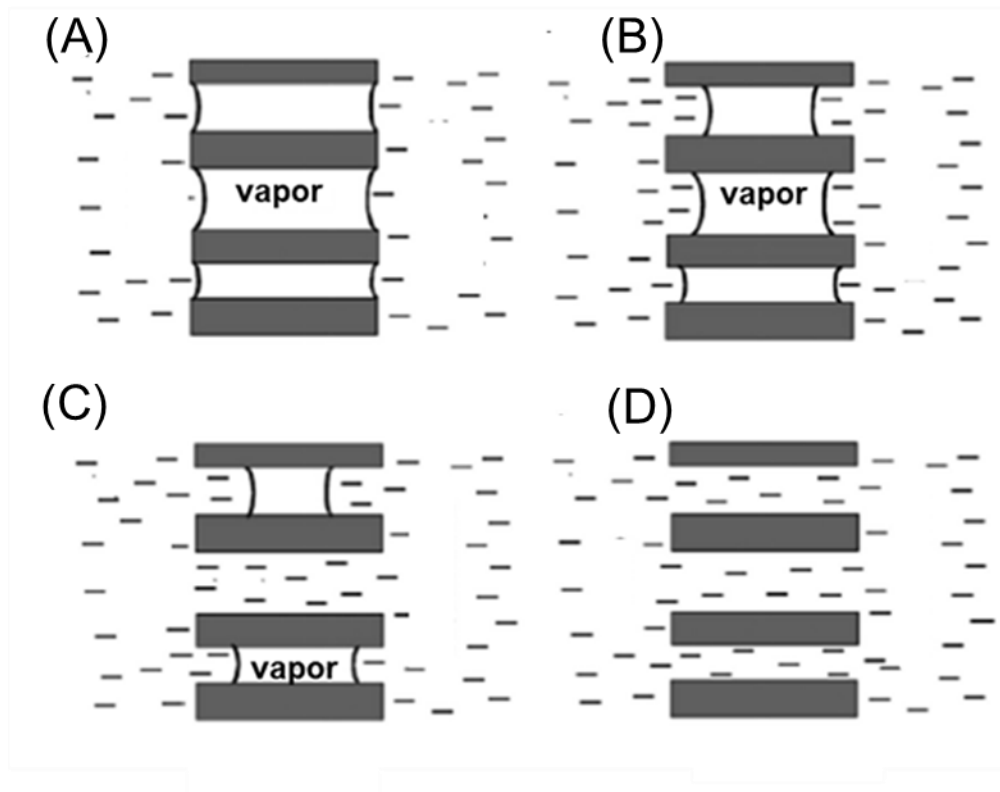


**Figure 2. 3** A schematic presentation of various forms of membrane wettability in MD process: (A) non-wetted; (B) surface-wetted; (C) partial-wetted; and (D) fully-wetted.<sup>38</sup>

### 2.3 Developing membranes for enhanced MD performance

Recently, nanotechnology has gained significant attention in its application for desalination and the treatment of both water and wastewater. Many researchers are now realizing the attractive properties and functionalities of the membranes by employing nanofibers and nanoparticles, with applicability in membrane preparation, fabrication, and modification. For instance, electrospun nanofiber membranes have been reported in many studies recently and have shown very interesting results. This report will discuss the preparation and characteristics of electrospun nanofiber membranes (ENMs) for water treatment in the MD separation process. Considerable efforts have been devoted to improving the hydrophobicity of the membranes by incorporating various

modifications. The main objective of the modification is to incorporate/enhance hydrophobic character to the membrane surface. Particularly, when the wettability of the membrane surface is shifted toward superhydrophobicity with a static water contact angle greater than  $150^\circ$  and a sliding angle less than  $10^\circ$ , the interaction between the feed water solution and membrane surface could be reduced, thereby reducing the fouling propensity. Superhydrophobic surfaces have characteristic of self-cleaning, which means that particles adhered to the surface can be removed easily while the droplet is rolling off. However, one critical concern of hydrophobic surfaces is how to enhance their oil-repellency. To expand the application of traditional MD membranes to desalinate challenging feed water like shale gas produced wastewater containing low surface tension contaminants, amphiphobic modification can be more effective to prevent the contact between contaminants and the membrane surface. The use of fluorosilanes and deposition of micro/nano particles have gained popularity for such modifications. High thermal stability, mechanical strength, and low surface energy are the main attractions for use of these modifiers.

### **2.3.1 Electrospun nanofiber membranes (ENMs)**

Electrospinning is a versatile membrane preparation method, which can fabricate nanofibers in a non-woven mat form by applying a high voltage to the polymer solution or melt.<sup>39</sup> The diagram of a typical electrospinning setup is shown in **Figure 2.4**, with the polymer solution placed inside a syringe and pressure applied by a pump. Once the electric field overcomes the surface tension of the polymer solution, a jet is ejected from the nozzle, the solvent is evaporated, and solidified nanofibers are deposited on the grounded collector. The collected nanofibrous mat is usually further dried in an oven or in the open air.<sup>40</sup> The mat formed shows very high porosity, excellent hydrophobicity, very good interconnectivity, and very high surface to volume ratio making them interesting candidates for desalination applications. The major challenge in electrospinning is the optimization of these parameters to obtain nanofibers with the desired morphologies and properties. **Table 2.2** summarizes the effect of solution, processes, and other parameters on the fiber formation during electrospinning.

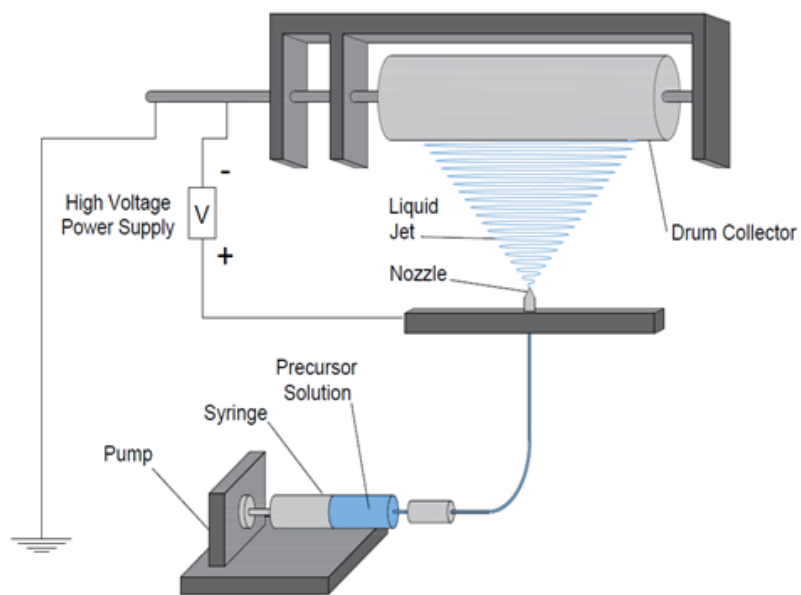


**Figure 2. 4** Typical electrospinning set-up consisting of nozzle, high voltage power supply, and grounded collector.<sup>40</sup>

**Table 2. 2** Effect of solution, process and other parameters on the fiber formation during electrospinning.

<b>Parameter</b>	<b>Effect/observation</b>
<b>Solution concentration</b>	<ul style="list-style-type: none"> <li>• Increasing concentration results in bigger fibers</li> <li>• Very low concentration can form beads on fibers</li> </ul>
<b>Molecular weight</b>	<ul style="list-style-type: none"> <li>• More bead formation at low molecular weight</li> <li>• Increasing molecular weight produces bigger and smoother fibers</li> </ul>
<b>Viscosity</b>	Increasing fiber diameter with the increase of viscosity
<b>Conductivity</b>	Thinner fibers are formed with the increase of conductivity
<b>Surface tension</b>	Low surface tension generates smooth and uniform fibers at low electric fields
<b>Applied voltage</b>	Generally, fiber diameter is decreased with the increase in applied voltage
<b>Feed rate</b>	<ul style="list-style-type: none"> <li>• Very high feed rate produces beads on fibers while very low feed rate cannot continuously produce fibers</li> <li>• Typical feed rate is below 3 mL/h</li> </ul>
<b>Distance to collector</b>	<ul style="list-style-type: none"> <li>• Too far or too near would result in bead formation</li> <li>• Needs sufficient time to elongate and dry</li> </ul>
<b>Temperature</b>	Increased temperature results in decreased fiber diameter
<b>Humidity</b>	High humidity can induce internal porosity of fiber

The properties of nanofibers can be tailored according to the need of layer thickness, fiber diameter, porosity, and functionalities by manipulating the electrospinning parameters, material selection, and post-processing treatments. Depending on the desired properties, electrospinning can be done via solution or melt electrospinning. In solution electrospinning, polymers are dissolved in a solvent or a solvent mixture, which is the commonly used type because of its easy preparation and set-up. A few notable polymers from a pool of over 200 potential polymers that have been electrospun include nylon-6, cellulose acetate (CA), poly(vinyl alcohol) (PVA), polyacrylonitrile (PAN), polyethylene terephthalate (PET), polystyrene (PS), polyether sulfone (Psf), polyurethane (PU), and polyvinylidene fluoride (PVDF). Some examples of membrane prepared through the electrospinning process along with their characteristics have been reported.<sup>41-43</sup>

Moreover, different functional materials can be incorporated into the nanofibers during or after their spinning thus incorporating multi-functionality into the fibers. Several nanoparticles (NPs) such as carbon nanotubes (CNTs), graphene, silver (Ag) NPs, titanium dioxide (TiO<sub>2</sub>) NPs, and iron oxide NPs have been incorporated or decorated on/in nanofibers via direct dispersion of NPs in polymer solution prior to electrospinning.<sup>44,45</sup> It is known that if nanoparticles are properly and uniformly loaded in a substrate such as nanofibers, it could dramatically improve the overall properties and performance of the composite material. The incorporation of nanoparticles could affect the mechanical, thermal, and surface properties of the material, including increasing or decreasing the wettability of the surface.

### **2.3.2 Superhydrophobic membranes**

To control fouling, researchers have tried feed pretreatment, increasing feed flow rate, hydraulic and chemical cleaning, altering the hydrophilicity of the membrane surface, reducing roughness, and changing the membrane surface charges.<sup>46</sup> Since these techniques impose additional cost and energy usage, a more efficient way of fouling mitigation is greatly needed. Shifting the wettability of the surface toward superhydrophobicity could reduce the interaction between the feed water solution and membrane surface, thereby reducing the fouling propensity.

Inspired by the lotus effect, a superhydrophobic membrane with water contact angle (WCA) above 150° and lower sliding angle can be fabricated to overcome pore wetting, in which a hierarchical structure of the surface created by micro- and nano- structures can enhance surface hydrophobicity by introduction of air pockets between the rough surface and water drop.

#### **(1) Basics of superhydrophobicity**

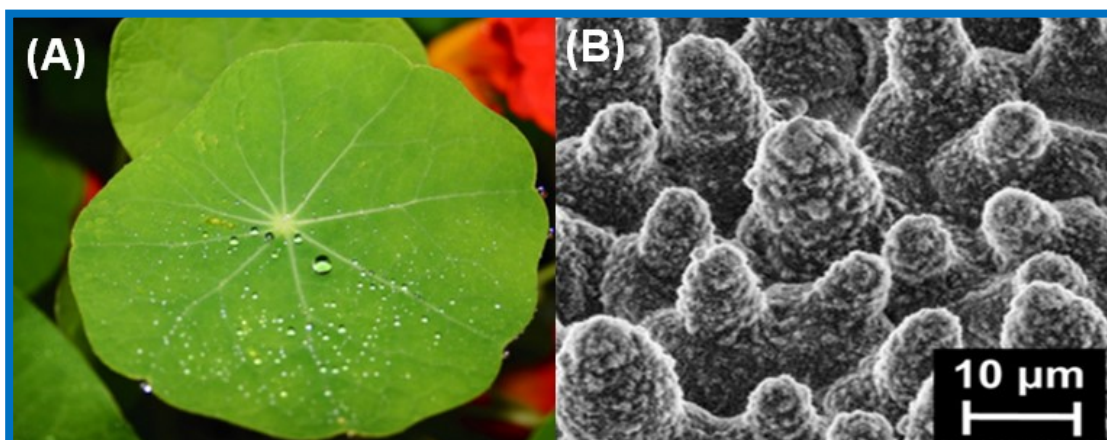


**Figure 2. 5** (A) Leaves with water droplets on them, (B) Scanning electron microscopy of a Lotus leaf microstructure.<sup>47,48</sup>

The surface of the lotus leaf exhibits a complex structure that incorporates both nano- and micro-scale roughness (see **Figure 2.5 A** and **B**). The plant's self-cleaning mechanism arises from valleys-like microstructure covered with nanoparticles of a hydrophobic wax material. Wettability is an important property of a solid surface, and the contact angle is commonly used to characterize the surface wettability. When a water droplet rests on a solid surface, three interfacial forces (liquid-vapor surface tension, solid-vapor interfacial tension, and solid-liquid interfacial tension) are in a thermodynamic balance.<sup>49</sup> These balanced forces determine whether the droplet spreads into a thin film or reaches to an equilibrium shape. The surface wettability of solid is governed by both chemistry and geometrical structure of the surface. Surface chemistry dictates the surface tensions at microscopic level but geometrical structure governs how these forces act upon the liquid.<sup>49</sup> Surface modification is one of the ways to improve the roughness and modify the chemistry of the surface to obtain a superhydrophobic material. Therefore, surface wettability can be tuned by varying one of these two parameters. Reducing the surface free energy by the functionalization of low surface energy materials (particularly fluorosilanes) is the most common practice for the generation of superhydrophobic surfaces. Alternatively, attempts have been made to generate a hierarchical nanostructure surface morphology with multilevel surface roughness in order to modulate surface wettability toward extremes.<sup>50</sup>

## (2) Methods for producing superhydrophobic surfaces

A variety of techniques such as plasma treatment, layer-by-layer assembly, dip coating, and electrospray were used to fabricate superhydrophobic surfaces. These routes can generate superhydrophobic surfaces via reducing the surface free energy of a rough surface or roughening a low surface energy material or a combination of both.<sup>50</sup>

(a) Plasma treatment

Plasma is an ionized gas, considered as the ‘fourth state of matter’. In order to create (excite) plasma, enough energy has to be supplied to the gas to cause its ionization.<sup>51</sup> Typically, the energy is supplied through a source of direct (DC) or alternative current (AC), radiofrequency (RF), or even microwave power (MW). It is possible to deposit very thin films or change the degree of hydrophilicity-hydrophobicity by changing plasma parameters, or even induce surface roughening. Plasma is a ‘dry’ technique free of the use of organic solvents, suitable to fabricate superhydrophobic surfaces in an environmentally friendly manner, which could be realized by either plasma deposition of a rough superhydrophobic material (e.g., hydrocarbon compounds, fluorosilane compounds and organosilicon precursors) or for roughening of a low surface energy material.<sup>52</sup> Although very interesting systems have been reported, several issues must be taken into account for future applications.<sup>53</sup> First of all, thermal plasma is typically limited to surfaces that are not sensitive to high temperature, while the cold plasma technology requires complex and expensive vacuum equipment and pumps. Furthermore, such processes are typically ‘batch’, rendering difficult their incorporation in already existing industrial lines. Finally, the conformity and especially the durability of the coatings should be considered, where practically no studies have been reported.

(b) Dip coating

Dip coating method involves the coating of a support layer by immersing it in the bath of a dilute solution followed by cross-linking and drying the coated layer using heat treatment.<sup>54</sup> When the membrane is taken out of the bath, a thin functional coating is deposited on the substrate membrane, and the solvent is removed by evaporation (**Figure 2.6**).<sup>54</sup> The coating property is influenced by several experimental parameters such as pH, temperature, adhesion of the solution, and presence of additives. Membranes fabricated by this technique can be used in gas separation, pervaporation, membrane distillation, and NF/RO applications. Compared with conventional thin film forming processes such as chemical vapor deposition (CVD) or sputtering, dip coating requires considerably less equipment and is potentially less expensive. However, the most important

advantage of dip coating over conventional coating methods is the ability to tailor the micro/nanostructured surface of the deposited film. Generally, the surface roughness is generated by adding various micro/nanoparticles of  $\text{TiO}_2$ ,  $\text{SiO}_2$ , and  $\text{ZnO}$  in different substances with low surface energy.<sup>55</sup> The dip coating process is used for manufacturing superhydrophobic surfaces from many types of materials. In many investigations, due to the presence of materials with low surface energy in the dip coating process, there is no other hydrophobic modification process required.

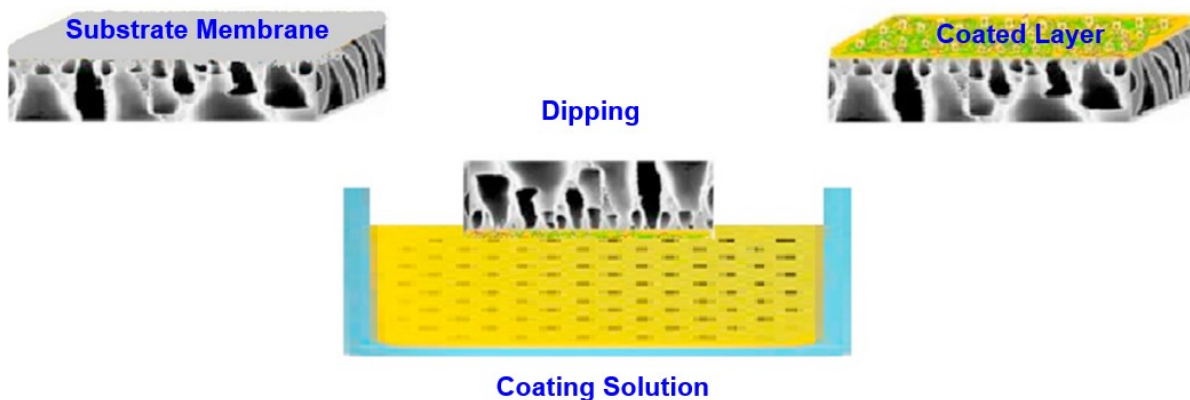


**Figure 2. 6** General scheme of membrane fabrication using the dip-coating technique.<sup>54</sup>

(c) Layer by layer assembly

The layer-by-layer (LBL) assembly technique is known as a simple and versatile method to fabricate thin multilayers with tunable composition, thickness, and morphology for targeted functionalization of solid surface (**Figure 2.7**). This technique usually involves processes where multiple layers are alternatively deposited on the solid surface, followed by solution rinse to remove the physically adsorbed materials. The driving force for LBL assembly is diverse, including electrostatic interaction, hydrogen bond interaction, coordination interaction, hydrophobic interaction, covalent bonds, amongst others.<sup>56</sup> The most deeply studied driving force for LBL assembly is the electrostatic interaction between oppositely charged species (mainly polyelectrolytes). In each assembly step, a polyelectrolyte layer is adsorbed on the charged substrate and reverses the surface charge so that in the next assembly step a polyelectrolyte layer with opposite charge can be adsorbed. Layers of oppositely charged species (polymers, particles, surfactants, etc.) are deposited one after another to create a multi-layer coating bound together through electrostatic interactions. Two steps emerged to obtain artificial surfaces with

superhydrophobicity:<sup>57</sup> (1) creating micro/nano-scale rough structure on substrate surface through LBL deposition of synthetic polyelectrolytes (eg. poly(acrylic acid), poly(allylamine hydrochloride)) and inorganic particles (eg. SiO<sub>2</sub>, TiO<sub>2</sub>); and (2) lowering the surface energy through deposition of a final fluoroalkylsilane layer on top of the LBL stack. However, some of the mentioned steps had to be conducted several times to reach suitable roughness, which further indicates that this procedure is not only entirely complicated but also lengthy.

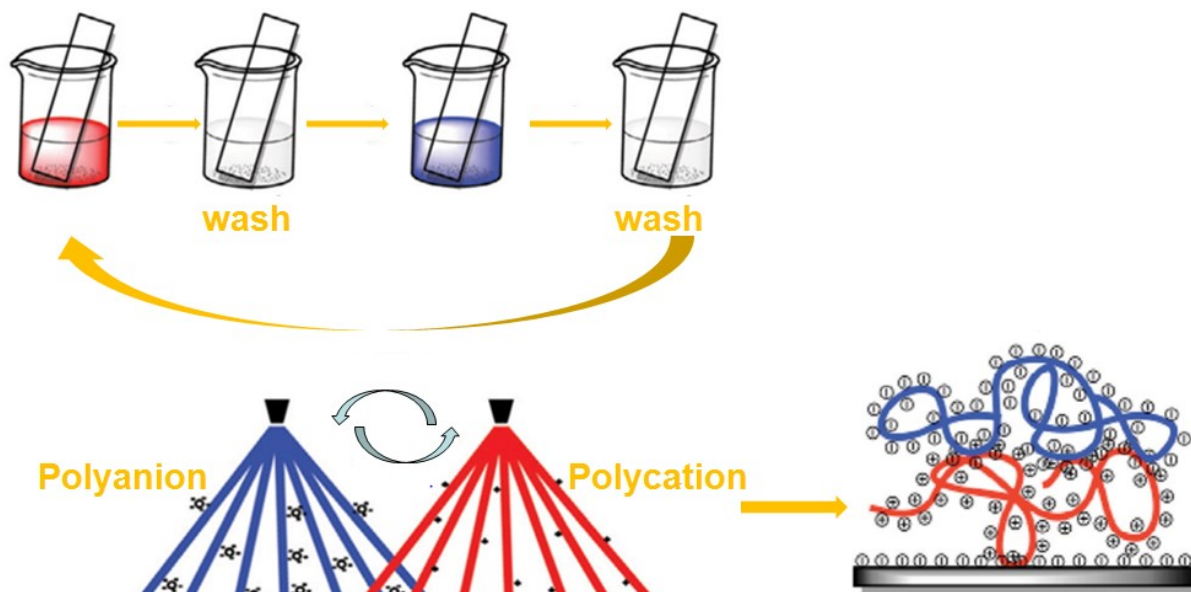


**Figure 2. 7** Schematic of layer-by-layer technique.<sup>57</sup>

(d) Electrospay

Electrospay is a simple, inexpensive, and convenient process for producing coated layers in an ambient environment in a highly reproducible manner from solutions. When the viscosity of the solutions is low enough, the solutions are sprayed in the shape of droplets, usually creating a very rough and particulated layer on a substrate. In this regard, electrospay deposition can be an appropriate method for producing rough layers, consequently exhibiting excellent superhydrophobicity. Generally, to turn the electrospinning process to electrospaying, higher voltage, lower distance, and less dense solutions are used.<sup>58</sup> Under these conditions, the spinning jet is destabilized and thereby fine droplets are formed on the collector. However, there are still several challenges to be faced, as electrospaying techniques are very sensitive to the liquid physical properties and the electric field in the vicinity of the emitter tip. Moreover, the nanofiber continuity is a main issue before widespread application of the electrospay technique.

### (e) Silanization

Silanization is a versatile technique to introduce surface functional groups on nanoparticles or membranes. It is considered as an ideal modification method, as it can be performed under mild conditions without any particular or expensive equipment. The reaction mechanism is schematically shown in **Figure 2.8**.<sup>59</sup> Generally, silanization reaction starts with the activation of silane molecules, which means the silanes (Si-OR) need to be hydrolyzed first to generate silanol (Si-OH). Then condensation reactions will occur between the silanol groups and the hydroxyl groups on the materials, leading to the formation of stable polymeric structure on the material surface.

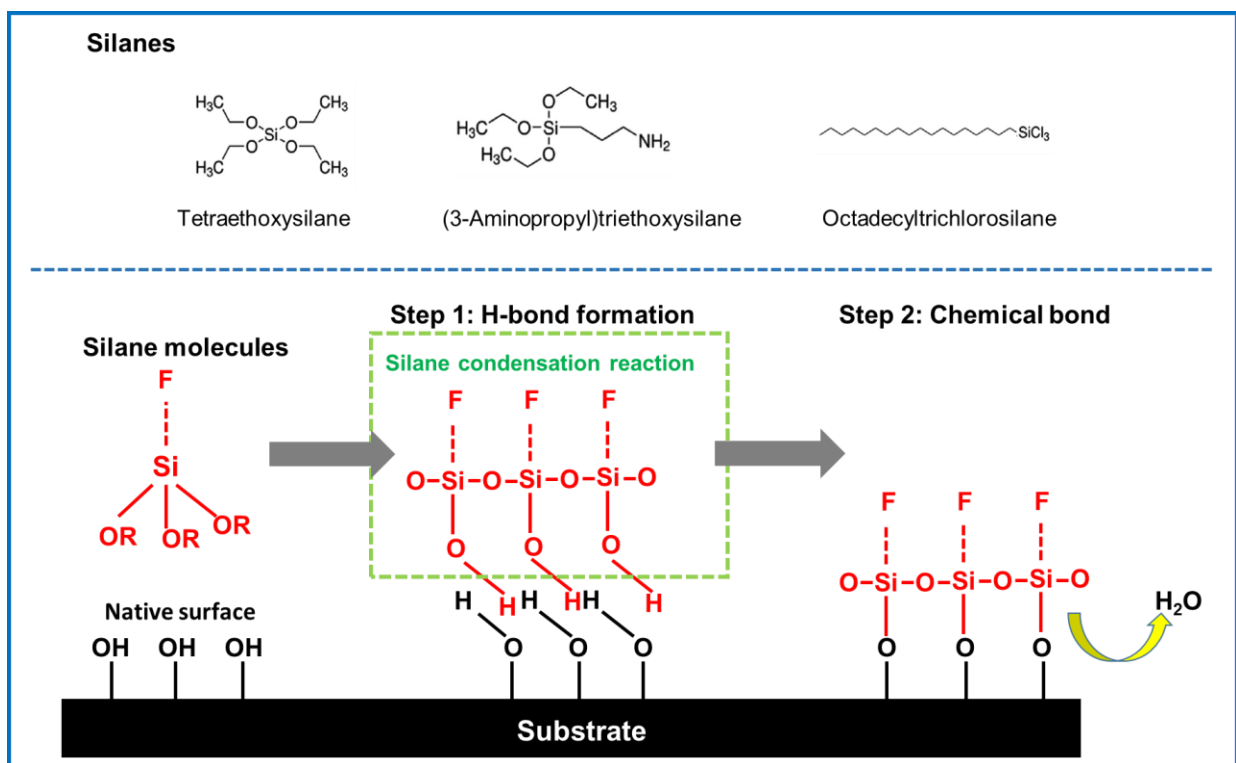


**Figure 2. 8** Schematic mechanism of silanization reaction.<sup>59</sup>

### 2.3.3 Superamphiphobic membranes

A superhydrophobic or super water-repellent surface shows large WCA and low sliding angle (SA). As a matter of fact, water drops easily roll off the surface producing a self-cleaning action, thus rinsing the dirt and debris particles. Although great breakthroughs on water-repellent surface have been made, the surface still has strong affinity to oil or surfactant and could be seriously

contaminated by hydrophobic or amphiprotic foulant. For the challenging feed water containing low surface tension contaminants such as oily substances and surfactants, amphiphobic modification can be more effective to prevent the contact between contaminants and membrane surface. Therefore, to satisfy the requirements of practical application, the superamphiphobic membranes, i.e., both superhydrophobic and near-superoleophobic with comprehensive wetting resistance, are in urgent demand.<sup>60</sup> If this is done, such water- and oil-repellent surfaces would impart a promising potential for the engineering of robust anticontamination, antisticking, and self-cleaning materials.<sup>61</sup>

This section summarizes the research in this field, describes different techniques towards the fabrication of superamphiphobic surfaces by combining design of surface roughness and surface chemistry, and a variety of existing functional applications.

(1) Different techniques towards the fabrication of superamphiphobic surfaces by combining design of surface roughness and surface chemistry

Oils and other organic liquids usually exhibit a higher solid surface attraction due to their lower surface tension compared to water. Therefore, it is much more difficult to construct oleophobic surfaces, especially oleophobic surfaces than superhydrophobic surfaces. In order to fabricate an amphiphobic surface, the surface energy of the solid surface should be lower than that of oil. The wettability of solid substrates is usually governed by their surface free energy and surface geometrical structures. Two different models, the so-called Wenzel regime<sup>62</sup> (**Figure 2.9 B**) and Cassie-Baxter regime<sup>63</sup> (**Figure 2.9 C**), were developed to explain the wetting behavior on a rough surface. In the Wenzel regime, surface roughness can promote either wettability ( $WCA < 90^\circ$ ) or non-wettability ( $WCA > 90^\circ$ ) depending on the chemical properties of the surface. Interestingly, if the surface is composed of small protrusions that cannot be filled by the liquid and are thus filled with air (i.e., trapping of air underneath the liquid droplet), the wetting phenomenon can be described by the Cassie-Baxter regime. In such a case, the liquid touches only the top of the surface with very limited contact area. The corresponding WCA is always much higher than that of a flat surface composed of the same material since the pores are filled with air, which is hydrophobic. Hence, surface topography plays a very profound effect on the wettability.

Tuteja et al. demonstrated that re-entrant surface curvature with semicircular ridges and grooves (**Figure 2.9 D**), in conjunction with chemical composition and roughened texture, are critical

factors in the design of amphiphobic surfaces that display excellent wetting resistance to a number of liquids with low surface tension.<sup>64</sup> For a liquid drop that is placed on the re-entrant structures, the net traction on the liquid vapor interface is directed upward, which supports the metastable Cassie state for the composite solid-liquid-air interface at thermodynamic equilibrium.<sup>64</sup> A variety of methods have been employed to create re-entrant structures on several substrate materials to impart surface amphiphobicity with low surface tension.<sup>65</sup>

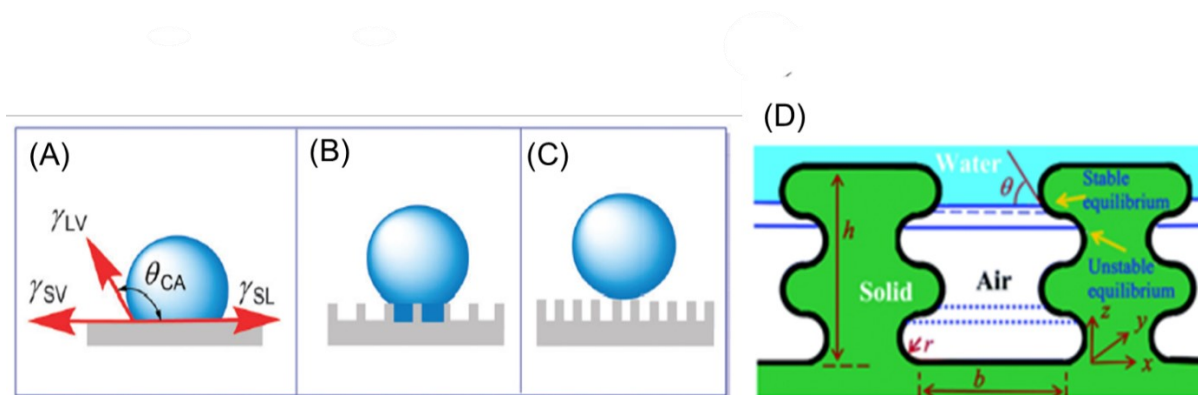


**Figure 2. 9** Schematic illustration of a droplet placed onto (A) a flat substrate and (B, C) rough substrates. Depending on the roughness of the surface, the droplet is either in the so-called (B) Wenzel regime or the (C) Cassie-Baxter regime. (D) A surface with the re-entrant structure.<sup>64</sup>

In order to obtain superamphiphobic surfaces, it is essential to control both the surface chemical composition and the surface geometry. Up to now, a wide variety of superamphiphobic surfaces have been constructed by using different synthesis strategies. In this section, I will mainly focus on the recent developments in the design and fabrication of superamphiphobic surfaces. Many synthesis strategies used in superhydrophobic systems can be adopted to design superamphiphobic materials. Two steps are involved: the generation of micro/nano-scale roughness and the functionalization with low surface energy materials (mainly fluorinated molecules). Depending on the sequence of the above two steps in the preparation process of a superamphiphobic surface, the fabrication strategies can be mainly classified into two strategies (**Figure 2.10**): (1) the ‘pre-roughening + post-fluorinating’ technique, and the (2) ‘pre-fluorinating + post-roughening’ technique.

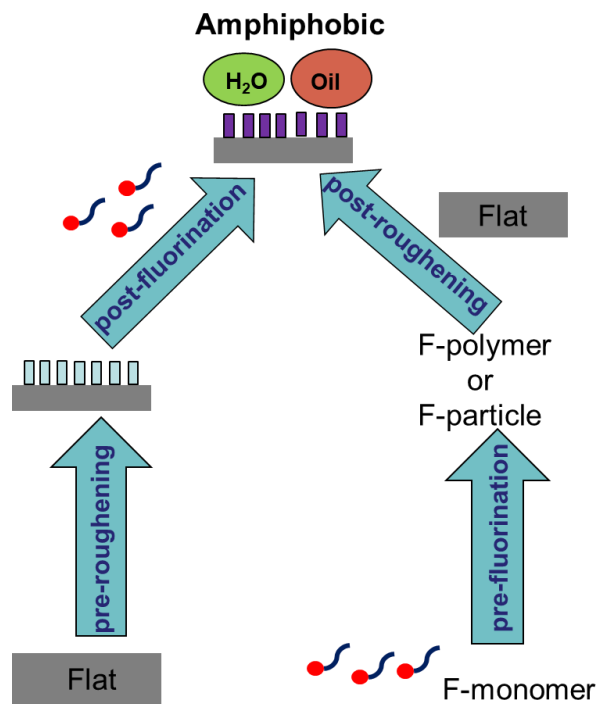


**Figure 2. 10** Two strategies towards the fabrication of superamphiphobic surfaces: pre-roughening + post-fluorination and pre-fluorination + post-roughening.

(a) Pre-roughening + post-fluorinating

Functionalization with nanoparticles represents an important method to generate nanoscale roughness on a substrate. The nanoparticles can be silica nanoparticles,<sup>66</sup> carbon nanotubes,<sup>67</sup> TiO<sub>2</sub> nanoparticles,<sup>68</sup> and so on. Silica nanoparticle is a common type of nanomaterial that is inexpensive and frequently used in the fabrication of surface roughness. For carbon nanotubes (CNTs), numerous applications have been found in many areas of science and engineering because of their excellent electronic, mechanical, and chemical properties. Recently, they were used to create surface roughness to impart super-repellant properties to the resultant surfaces. Aside from silica nanoparticles and carbon nanotubes, carbon nanoparticles such as carbon nanofibers, graphene-based materials, as well as other inorganic particles such as nano ZnO and CuO have also been reported to generate surface roughness.<sup>69</sup> In addition, etching is a facile and inexpensive method that is frequently used in creating surface roughness.<sup>70</sup> Depending on the nature of the substrate, etching techniques can be classified into the following types: acid etching, base etching, electrochemical etching, ion etching, plasma etching, amongst others. Furthermore, sol-gel

synthesis, sputter deposition, lithography, and other strategies can be applied to construct surface roughness.<sup>71</sup>

After surface roughness is created, the substrates must be further chemically modified with low-surface-energy materials, normally fluorinated compounds, to achieve superamphiphobicity. Generally, a fluorinated layer can normally be produced by depositing molecular perfluoroalkane with a functional group at one terminal.<sup>72</sup> However, it can be also achieved by coating a fluorinated-polymer solution.

#### (b) Pre-fluorinating + post-roughening

Pre-fluorinating + post-roughening represents another strategy to fabricate superamphiphobic surfaces. In such a case, fluorinated polymers or nanoparticles were synthesized first and subsequently applied to substrates via spin-coating, spray-coating, dip-coating, electrospinning, sol-gel transition, or other techniques, generating roughened structures with a low-surface-energy layer on the surface.

Spinning or spraying fluorinated silica nanoparticles,<sup>73,74</sup> spraying fluorinated carbon nanotubes,<sup>23</sup> electrospinning a blend of a fluoroalkyl polyhedral oligomeric silsesquioxane (POSS),<sup>75</sup> or a common polymer are frequently used for the surface modification of a flat surface.

#### (2) A variety of existing functional applications of amphiphobic surfaces

With the increasing demand for functional materials with excellent anti-wetting ability, a great deal of interest has been focused on the development of superamphiphobic surfaces displaying a wide range of applications. The discussion below will focus on how surface superamphiphobic modification brings about new functions related to membrane process such as anti-wetting, self-cleaning, and anti-bacterial activity which are not readily available for current membrane materials.

##### (a) Anti-wetting

There is no doubt that most applications of superamphiphobic surfaces are based on their versatile function in anti-wetting, and all the other applications are derived from this significant function. Superamphiphobic surfaces display characteristics of both superhydrophobicity and superoleophobicity, and thereby they share most of the functions as superhydrophobic surfaces. However, compared with superhydrophobic surfaces, the biggest advantage of superamphiphobic surfaces is their antiwetting ability not only for pure water but also for low surface tension liquids

like detergent solution, underground water, shale gas produced wastewater, sea water, and organic 'oils' like hexane, hexadecane, toluene, mineral oil, and cooking oil. The antiwetting function can be applied to many traditional materials such as glass,<sup>76</sup> steel,<sup>77</sup> textile,<sup>78</sup> fabric,<sup>79</sup> paper,<sup>80</sup> and so on, protecting their surfaces from being wetted, contaminated, or fouled by water and oil pollutants. Besides, superamphiphobic modifications bring about not only the antiwetting function but also other derived functions such as self-cleaning, anti-fogging, anti-bacterial activity, corrosion resistance, and oil transportation, some of which will be discussed in the following sections.

#### (b) Self-cleaning

Self-cleaning coatings can be broadly classified into two major types: photocatalysis-induced superhydrophilic coatings and superhydrophobic or superamphiphobic coatings with superhydrophobicity. In superhydrophilic coatings ( $WCA < 5^\circ$ ), the surface is cleaned by the sheeting effect of water and by breaking down the complex organic substances into carbon dioxide and water. In contrast, in superhydrophobic or superamphiphobic surfaces, the air pockets that get trapped between the nanostructured substrate and the water droplet result in the formation of a composite solid/air/liquid interface, which leads to an increase in CA of the liquid droplet, thereby facilitating the de-wetting of the surface and enabling the droplet to roll off easily, taking away the dirt and other pollutants.<sup>81</sup>

#### (c) Anti-bacterial growth properties

In addition to extreme non-wettability, superamphiphobic surfaces also exhibit antibacterial activity. The antibacterial properties of superamphiphobic sol-gel coatings for cotton fabrics by using *E.coli* bacteria as a model exhibited a long-lasting antibacterial effect without the addition of any antibacterial agents.<sup>82</sup> The antibacterial activity test revealed that the reduction of the bacteria on superamphiphobic cotton fabrics was nearly 100%. In Huang's group,<sup>83</sup> superamphiphobic cellulose filter paper was confirmed to show effective inhibition of bacteria adhesion by using alkaline etching to enhance the surface roughness, followed by depositing ultrathin titania films via a facile surface sol-gel process, and subsequently surface treatment with fluoroalkylsilane. Due to the combination of surface roughness and low surface energy of the fluoroalkylsilane monolayers, the naturally hydrophilic filter paper was converted into superamphiphobic.

#### (3) Limitations for current superamphiphobic surfaces

By combining the design of surface roughness and surface chemistry, a variety of different techniques towards the fabrication of superamphiphobic surfaces have been developed. Nevertheless, there are still lots of challenges that need to be addressed. First of all, a majority of the fabrication methods are limited to laboratory research and not suitable for practical production. Meanwhile, many of these methods require expensive preparation and time-consuming procedures. In addition, the lifetime of superamphiphobicity is another important issue which needs to be considered for practical applications. Finally, most superamphiphobic surfaces face the problem of poor mechanical stability. They cannot find practical use without enough mechanical stability.

## Chapter 3. Experimental

The permeability and long-term stability of MD membranes are closely related to the physical-chemical properties of the membrane surface. Therefore, the resultant membranes should be characterized to evaluate basic physiochemical properties and surface wettability. In this chapter, general information about the frequently used chemicals, materials, and characterization techniques are presented. In addition, the electrospinning setup for nanofibrous membranes fabrication is briefly introduced. Finally, the DCMD configuration for water purification and membrane performance evaluation are illustrated.

### 3.1 Materials and chemicals

The sources of chemicals for dope solution preparation utilized in the electrospinning process are listed below. PVDF-HFP (average  $M_w$ :  $\sim 400,000$ ), dimethylacetamide (DMAc), were purchased from Sigma-Aldrich (Oakville, ON, Canada) and used without any pretreatment. Acetone (ACS reagent grade) was purchased from Fisher-Scientific (Ottawa, ON, Canada). Single layer rGO nanosheets, with a thickness of 0.7-1.2 nm and a length of 300-800 nm, were purchased from Cheap Tubes Inc. (Grafton, VT, USA).

The chemicals used for feed solutions in DCMD tests are listed below. Deionized (DI) water was prepared using a Milli-Q purification system (Millipore, Billerica, MA). Sodium chloride (NaCl  $\geq 99.5$  wt%) and calcium chloride ( $\text{CaCl}_2 > 85$  wt%, anhydrous, 4-8 mesh) were purchased from Fisher-Scientific (St Laurent, QC, Canada).

### 3.2 Electrospinning process

Electrospinning technique was applied here to fabricate the inorganic/organic composite membranes in Chapter 4 and Chapter 6, or the nanofibrous substrate in Chapter 5. The needle-to-collector electrospinning set-up (vertical configuration) in the lab consists of four main components (**Figure A-1**): (1) the high voltage power supply for charging the dope solution; (2) the syringe pump containing dope solution; (3) the spinneret for ejecting nanofibers; and (4) the grounded drum, acting as the conductive substrate used to collect the charged fibers. However, using this metallic collector alone, the detachment of the nanofibrous mat is difficult. Alternatively, the drum can be covered with an additional material to gather the electrospun fibers which will be

later removed. Aluminum foil and non-woven fabrics are commonly used for this purpose. The covering materials can affect the arrangement of the resulting fibers. Therefore, the membrane morphology and pore size. Both the process parameters (applied voltage, feed rate, rotating speed for the drum collector, and distance to collector) and dope parameters (polymer concentration and solvents) were adjusted during the electrospinning process to obtain the ideal nanofibrous mats for testing.

### **3.3 Characterizations**

#### **(1) Surface morphology (SEM and AFM) and surface chemistry (XPS and ATR-FTIR)**

Membrane surface morphology and chemical composition are two major factors determining surface wettability and thus are discussed first. Electrospinning was applied to fabricate composite nanofibrous membranes as this technique has been demonstrated as a versatile process to prepare MD membranes with high hydrophobicity, high porosity, and controllable thickness. Moreover, electrospun mats with three-dimensional nanofibrous network provide a re-entrant structure, critical for improving surface superamphiphobicity. The surface morphology of the membrane could be observed via scanning-electron microscopy (SEM, FE-SEM; FEI company, USA), samples were coated with a thin 4 nm layer of palladium (Pd) before observation by microscopy. The surface topography could be measured via atomic force microscope (AFM, Oxford Instruments-Asylum Research, Santa Barbara, CA, USA). The average roughness (Ra) values were obtained using the “Gwyddion” software. In order to confirm the molecular level modification, X-ray photoelectron spectroscopy (XPS, SK-Alpha) was applied to test the elemental content, thereby indicating the surface domain chemical composition. Furthermore, XPS could be applied to analyze a single elemental peak and then test for the content of a certain functional group on the surface, before and after modification. Finally, to find the existence of chemical bonds on the membrane surface, the Attenuated total reflection - Fourier transform infrared spectroscopy (ATR-FTIR) were utilized and thereby indicated the interaction between modifiers and membrane surface. FT-IR was performed with a Nicolet 6700 / Smart iTR (Thermo Scientific, Waltham, MA, USA) equipped with an attenuated total reflectance single logic (ATR) accessory.

#### **(2) Maximum pore size, mean pore size and pore size distribution**

An appropriate mean pore size and a narrow pore size distribution are suggested for the permeability and selectivity of MD membranes. Higher permeate flux can be obtained at larger pore sizes, however, smaller pore sizes are also needed to avoid pore wetting. The pore size distribution should be as narrow as possible to prevent solutes from feed side passing through the membrane. The mean pore size and pore size distribution of the as-prepared membranes were characterized by using a capillary flow porometer (CFP-1500AE, Porous Materials Inc. (PMI), Ithaca, NY, USA) based on the wet/dry flow method, where membranes were first wetted using a wetting liquid called Galwick (surface tension: 15.9 mN/m) and then placed in a sealed chamber through which gas flows. The maximum pore size of the membranes was characterized by the bubble point pressure test.

### (3) Liquid entry pressure of water (LEP<sub>w</sub>) measurement

The liquid entry pressure of water (LEP<sub>w</sub>) was measured by placing the membrane in a dead-end filtration cell. Compressed nitrogen was used to apply pressure to the cell. Pressure was recorded when the first drop of water came out from the cell. The experiment was carried out three times using different membranes fabricated under the same conditions. The results were averaged to provide a final LEP<sub>w</sub> value. LEP<sub>w</sub> measurement system is shown in **Figure 3.1**.

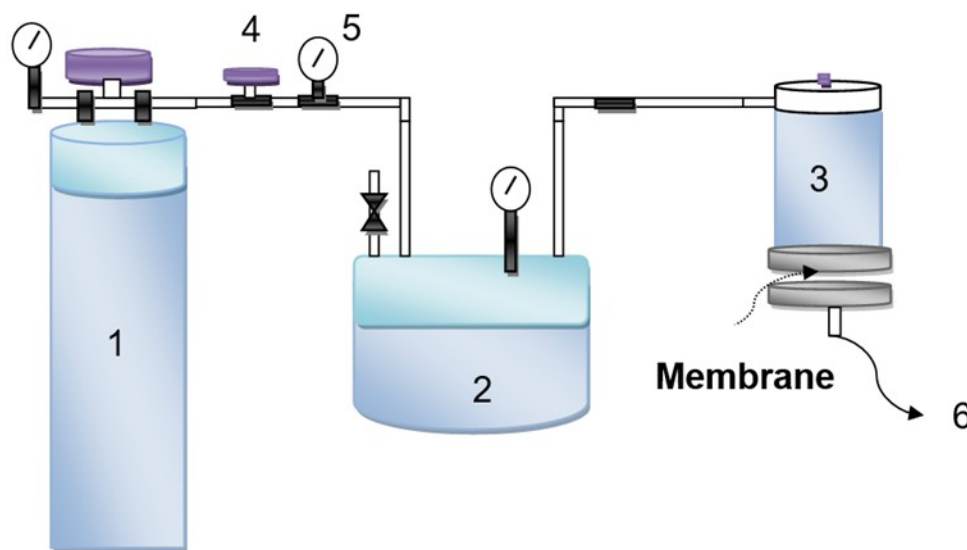


**Figure 3. 1** Setup for LEP measurements: (1) nitrogen cylinder, (2) pressured container, (3) membrane cell, (4) pressure regulator, (5) pressure meter, and (6) outlet.

### (4) Surface wettability (Contact angle)

The surface wettability of the membrane before and after modification could be evaluated via observation of contact angles between membrane surface and liquids interfaces. The liquid repellency of a surface is determined by its contact angle with the selected tested liquids. In this research, surface wetting of the membranes was evaluated by contact angle measurements of deionized water ( $\gamma = 72.5$  mN/m, diiodomethane ( $\gamma = 50.1$  mN/m) and water-ethanol mixtures ( $\gamma = 53.4\sim 22.2$  mN/m) using a video contact angle system (VCA; AST Products, Inc., Billerica, MA, USA). The static contact angles were measured by using the system software (VCA optima XE). The water sliding angles were measured by tilting the fixed membrane samples until the water droplet (10  $\mu$ L) started to move on the surface. At least three desiccator-dried samples were selected for contact angle measurements and a minimum of three points were measured for each sample. The data was averaged between the samples.

### 3.4 DCMD performance tests

Evaluation of DCMD performance was conducted with the apparatus shown in **Figure 3.2**. A picture of the DCMD set-up is presented in **Figure A-2**. The flat-sheet membrane, with an effective area of 34 cm<sup>2</sup> (8.5 cm  $\times$  4 cm), was tightly affixed into the PTFE membrane cell (CF042P-FO, Sterlitech Corporation, USA). The hot feed solution was maintained in a constant temperature water bath. The feed and cold solution were respectively moved at the same speed across the bottom and upper face of the membrane cell with the help of two gear pumps (GH-75211-10, Cole-parmer, Canada) at around 0.8 psi (GH-68930-12, Cole-Parmer, Canada). The circulation feed and permeate rate were detected by two flowmeters (0.1-1 LPM, McMaster-CARR, Canada) and held at a constant value. The experiments were first carried out with 3.5 w.t.% NaCl solution to determine the water flux of the membranes. Subsequently, feed solutions containing various kinds of contaminants were employed to investigate salt rejection. The operational temperature was monitored at the inlet and outlet of the module using four thermocouples (SCPSS-032u-6, OMEGA, Canada) connected to a thermometer (EW-91427-00, Cole-Parmer, Canada). The weight gain in the cold side was recorded at a fixed time interval by a digital analytical balance. The conductivity of salts in the distillate was investigated with an electric conductivity meter (Oakton Instruments, Vernon Hills, IL, USA). The permeate flux,  $J$ , of the prepared membrane was calculated according to the following equation (3-1):

$$J = \frac{\Delta M}{A\Delta t}$$

where  $J$  is the permeate flux ( $\text{kg m}^{-2} \text{h}^{-1}$ ),  $\Delta M$  is the quantity of distillate (kg),  $A$  is the effective membrane area ( $\text{m}^2$ ) and  $\Delta t$  is the operation time (h). The salt rejection  $R$  was calculated by the following equation (3-2):

$$R = \frac{C_f - C_p}{C_f} \times 100\%$$

where  $C_f$  and  $C_p$  are the concentration of the feed and permeate, respectively.

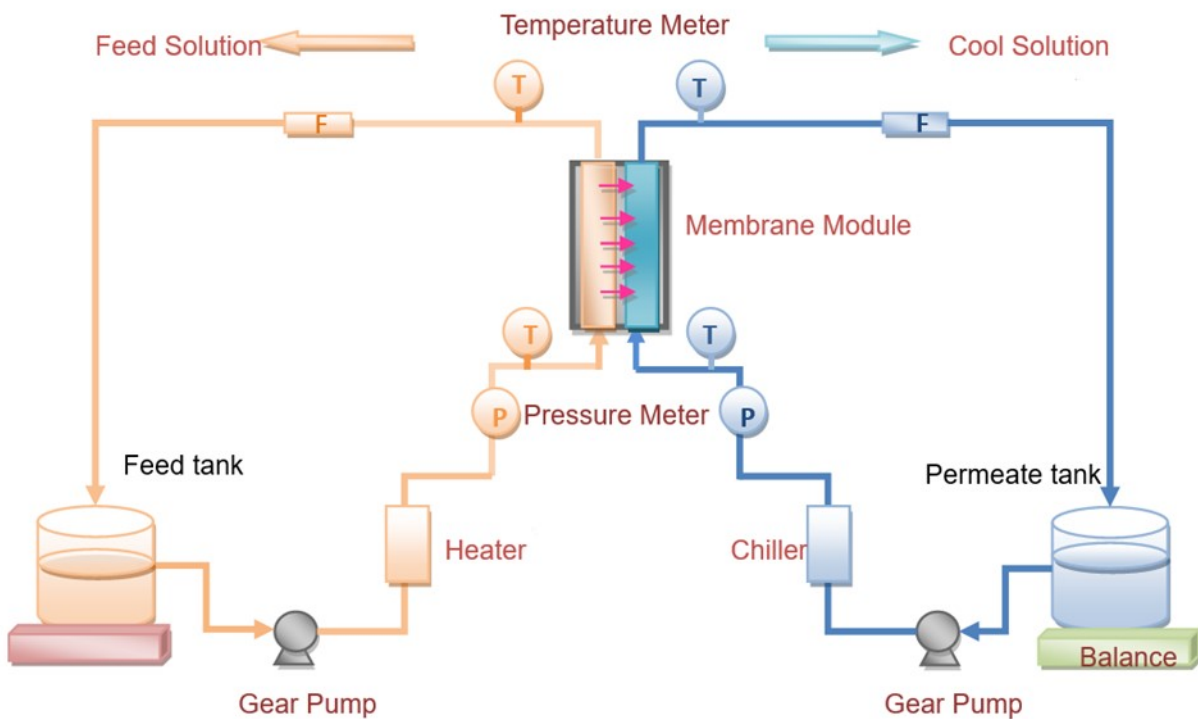


**Figure 3. 2** Schematic diagram of the DCMD set-up.

## **Chapter 4. Highly Hydrophobic Electrospun Reduced Graphene Oxide (rGO)/PVDF-HFP Membranes for Use in Membrane Distillation**

Membrane distillation has seen a growing amount of industrial interest due to its low operating pressure, minimal temperature requirements, and high salt rejection. This body of work involves the fabrication of a microporous nanocomposite membrane with enhanced hydrophobicity for use in direct contact membrane distillation (DCMD). Reduced graphene oxide/poly (vinylidene fluoride-co-hexafluoropropylene) (rGO/ PVDF-HFP) flat-sheet membranes were prepared via a facile electrospinning technique. These fabricated membranes were characterized using techniques including SEM, XPS, TGA test, liquid entry pressure (LEP), and contact angle measurement in order to investigate the effect of rGO incorporation on membrane surface morphology and physicochemical properties. Results demonstrated that a maximum water contact angle of  $139^\circ$  was achieved with an increased LEP up to 103.42 kPa. Anti-scaling and anti-wetting performance of fabricated membranes were investigated with 60 g/L sodium chloride for 2520 min. The rGO-incorporated membranes exhibited excellent stability and durability with a salt rejection of over 99.97% and an average flux of  $20.37 \text{ kg m}^{-2} \text{ h}^{-1}$ , indicating the promise of rGO-based hydrophobic membranes for applications in desalination, wastewater disposal, and food processing.

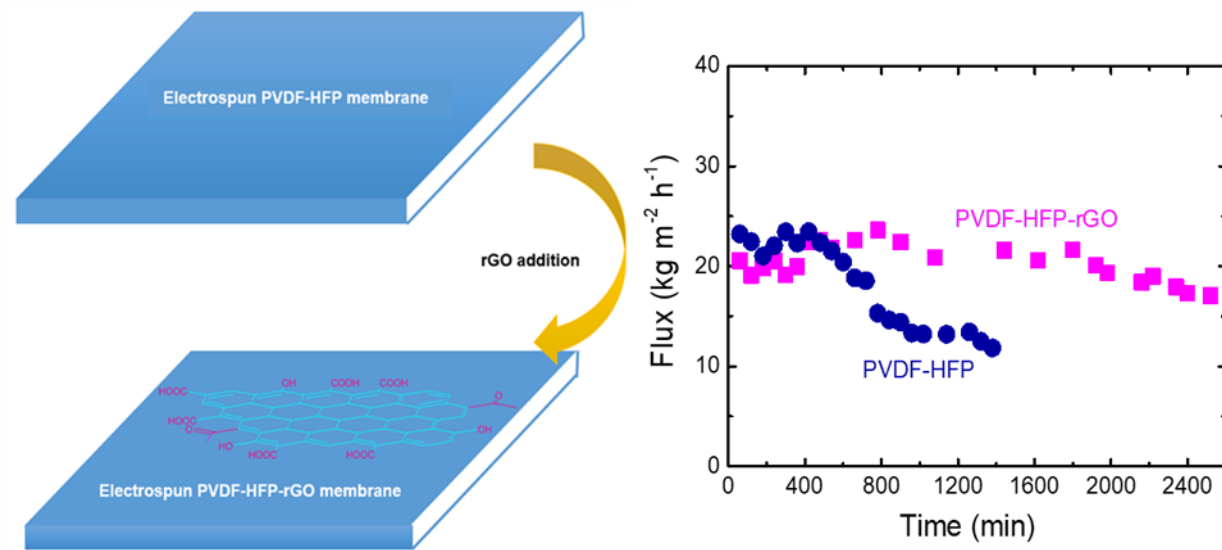


**Figure 4. 1** Graphical Abstract

## 4.1 Background

Membrane-based technologies play an important role in water and wastewater treatment as well as desalination. Currently, several membrane-based technologies, such as reverse osmosis (RO), nanofiltration (NF), ultrafiltration (UF), and microfiltration (MF), are widely used.<sup>84,85</sup> Among them, RO is the most energy-efficient technology for seawater desalination which is the benchmark for any new desalination technology.<sup>8</sup> In comparison with RO, MD is expected to be a cost-effective technology due to its low heat and operating pressure demands, showing potential for the use of waste heat.

Membrane Distillation (MD) shows promise for use in turning highly saline water into potable water with mild operating conditions required (low operating pressure and temperature) while theoretically offering complete (100%) salt rejection.<sup>86,87</sup> This process is driven by a vapor pressure difference between porous hydrophobic membrane surfaces, through which only water vapor molecules can pass.<sup>88</sup>

Poly (vinylidene fluoride-co-hexafluoropropylene) (PVDF-HFP) is a copolymer that has been identified as a potential material for use in membrane applications.<sup>89</sup> In comparison with poly(vinylidene fluoride) (PVDF), which is one of the most commonly used materials for MD membrane fabrication, PVDF-HFP has lower crystallinity due to the incorporation of a hexafluoropropene (HFP) comonomer into the main molecular backbone.<sup>90</sup> It is also believed that the presence of HFP groups results in an increase of fluorine content and provides PVDF-HFP with better hydrophobic chains.<sup>91</sup> Therefore, PVDF-HFP is a prime candidate for use in MD applications.

Little work has been conducted where PVDF-HFP was used to produce MD membranes. Among those that do exist, Sufyan Fadhil et al<sup>92</sup> prepared PVDF-HFP flat sheet membranes for DCMD via phase inversion using triethyl phosphate (TEP) as an ecological solvent. They found that all membranes prepared from different concentrations of PVDF-HFP exhibited a similar sponge-like structure, and a DCMD permeation of  $16.1 \text{ kg m}^{-2} \text{ h}^{-1}$  and a salt rejection of 99.3% were observed across all membranes.

In various fields, the use of graphene-based materials—particularly graphene oxide (GO) and reduced graphene oxide (rGO)—has been growing, due to their specific 2D structure, and unique mechanical and electrical properties.<sup>93,94</sup> Although rGO has been widely proposed for applications ranging from conductive thin films<sup>95</sup> to nanofiller materials<sup>96</sup> to versatile platforms for anchoring

functional polymers, very limited efforts have been devoted to incorporating them into the fields of wastewater treatment and desalination via MD separation processes.<sup>97</sup> Improving surface wetting resistance and hydrophobicity by using rGO films has been demonstrated both theoretically and experimentally.<sup>98</sup> This material is hydrophobic due to high density of carbon atoms in its surface. Experimental reports have shown that the contact angle of rGO can reach 125°.<sup>99</sup> In addition, the hexagonal honeycomb lattice found in a sp<sup>2</sup>-bonded carbon graphene scaffold can serve as effective sorption sites for water vapor while still repelling water molecules.<sup>100</sup> Therefore, rGO may be a suitable reinforcement candidate for the realization of high contact angle and flux with polymer, ceramic, and metal matrix composites in MD applications.<sup>101</sup> Moreover, rGO nanosheets demonstrate excellent antifouling properties.<sup>102</sup> The potential application of GO in water desalination and purification has also been explored.<sup>103-105</sup> However, the practical application of rGO is challenging because it is difficult to identify affordable and scalable graphene frameworks while still maintaining the desired molecular and ion sieving performance.<sup>105</sup>

Recently, electrospun membranes have gained considerable attention in energy production and environmental applications such as filtration, catalysis, and solar cells.<sup>106</sup> The unique features of these non-woven membranes include controllable membrane thickness and higher porosity, which are achieved by various solution viscosities, applied electrical potentials, and controlled flow rates of dope solutions.<sup>107</sup> Due to these unique properties, non-woven electrospun membranes have been applied in water filtration and chemical separation processes.<sup>108,109</sup> Moreover, electrospun PVDF membranes have also been proposed for use in MD.<sup>110</sup> However, the LEPw (liquid entry pressure of water) values of most electrospun nanofiber membranes being used in MD are lower than 100 kPa, a higher LEP is desired to improve wetting resistance.<sup>111</sup>

The objective of this research is to incorporate rGO with hydrophobic PVDF-HFP in order to fabricate highly hydrophobic flat-sheet membranes for MD. To the best of our knowledge, there is no comparable studies in the literature concerning the fabrication of electrospun membranes composed of both PVDF-HFP and rGO for MD applications. Electrospun membranes, PVDF-HFP-rGO, were prepared with different thicknesses at varying electrospinning times. These membranes were used for desalination via direct contact membrane distillation (DCMD). Fabricated membranes were characterized using different techniques such as SEM, XPS, TGA test, LEPw, pore size distributions and contact angle measurement to investigate the effect of rGO

incorporation on surface morphology and physicochemical properties. Finally, anti-scaling and anti-wetting performance were evaluated with 60 g/L sodium chloride for 2520 min.

## **4.2 Materials and methods**

### **4.2.1 Materials and chemicals**

PVDF-HFP, DMAc, acetone, and reduced graphene oxide were used to prepare the dope solution. NaCl and DI water were used to prepare the feed solution during the DCMD performance tests. Detailed information about the chemicals was described in Chapter 3.1.

### **4.2.2 Electrospun membrane preparation**

A picture of the electrospinning system is presented in **Figure A-1**. The dope solution was prepared by dissolving PVDF-HFP (3.0 g) in a 20 mL of mixture of DMAc/acetone (8/12, V/V). The mixture of rGO and PVDF-HFP was prepared by suspending 30 mg (0.15 wt%) of rGO in the aforementioned mixture by probe sonication (Branson 3510, Shanghai, China) for 10 min, then stirred overnight on a hot plate at 45 °C.

The main challenge of electrospinning the PVDF-HFP/ rGO suspension is the limited solubility of rGO in DMAc/acetone. Nonetheless, due to the sonication treatment and the increase in the solution viscosity, the prepared solution was stable enough for electrospinning before the agglomeration of the nano-sheets. The solvent ratio of DMAc/Acetone varied from 8/2 (v:v) to 2/3 (v:v) to generate uniform nanofibers. Only under the ratio of 2:3, continuous fibers ejected from the nozzle and finally formed a smooth nanofibrous mat on the collector (**Table A-1**).

30 mL of each solution were loaded into a Luer-lock syringe (Vitaneedle, MA). Electrospinning of the dope solutions was conducted using a Nanospinner (NE300, Inovenso, Turkey). Polymeric solutions were delivered to the metallic nozzle at a flow rate of 2.0 mL/h. High voltage (25 kV) was applied between the nozzle and the electrically grounded metallic drum. The distance between nozzle tip and collector (12 cm), temperature (24 °C) and relative humidity (25 %) were held constant during the process.

### 4.2.3 Membrane characterization

The morphology of pristine PVDF-HFP and rGO-incorporated membranes were observed by SEM. Fiber diameter distribution and frequency were measured via ImageJ software. The elemental compositions of the membranes were evaluated by XPS. The presence of rGO was confirmed via Raman spectroscopy (Invia Reflex-Renishaw). Thermal properties of the membranes were characterized by thermal gravimetric analysis (TGA Q5000 V3.15). Surface hydrophobicity of the membranes was evaluated by contact angle measurements of deionized water using the VCA video contact angle system. The mean pore size and distribution were examined by capillary flow porometer. LEPw was measured by the home-made filtration system (detailed information was described in Chapter 3.3).<sup>112</sup>

### 4.2.4 Porosity

The flat-sheet membrane porosity ( $\varepsilon$ ) was determined by the gravimetric method and calculated by the following equation (4-1).

$$\varepsilon = \frac{W_w - W_d}{\rho_l A l}$$

where  $W_w$  is the weight of the wet membrane,  $W_d$  is the weight of the dry membrane,  $\rho_l$  is the liquid density. Isopropyl alcohol (Fisher Scientific, USA) was used as the wetting liquid, as it can penetrate the pores of the hydrophobic membrane while water cannot.  $A$  is effective area of the membrane (2.83 cm<sup>2</sup>),  $l$  is the membrane thickness.

### 4.2.5 Membrane performance evaluation (DCMD Performance)

Evaluation of membrane performance was conducted with lab-scale DCMD set-up (detailed information was described in Chapter 3.4). The circulation feed and permeate rate were detected by two flowmeters (0.1-1 LPM, McMaster-CARR, Canada) and held at a constant 0.75 LPM. The experiments were first carried out with DI water to determine the pure water flux of the membranes. Subsequently, 60 g/L of NaCl solution was employed as feed solution to investigate salt rejection. The inlet temperature of the hot feed varied from 50 °C to 75 °C, while the cold side was held at a constant 25 °C. The conductivity of NaCl in the distillate was investigated with an electric conductivity meter. The permeate flux and salt rejection of the prepared membrane were calculated.

## 4.3 Results and discussion

### 4.3.1 Membrane morphology

Pristine and composite PVDF-HFP nanofibers were successfully synthesized via electrospinning. Morphology and fiber diameter distribution were investigated by SEM analysis and the results are presented in **Figure 4.2**. It can be seen from **Figure 4.2 A-B** that both the PVDF-HFP and rGO-incorporated mats possessed very smooth fiber surfaces, without any observable beads in their structure. Furthermore, pristine PVDF-HFP nanofibrous membranes produced by electrospinning of 15.0 wt% PVDF-HFP polymer solution contained fibers with diameters in the range of  $225.42 \pm 24.99$  nm (**Figure 4.2 C**). However, by adding rGO into the dope solution, thinner fibers were formed with the mean size of  $164.94 \pm 52.98$  nm due to the conductivity increase of the dope solution (**Figure 4.2 D**). The SEM micrographs demonstrated that the incorporation of rGO into the PVDF-HFP precursor solution significantly influenced the morphology of the nanofibers.

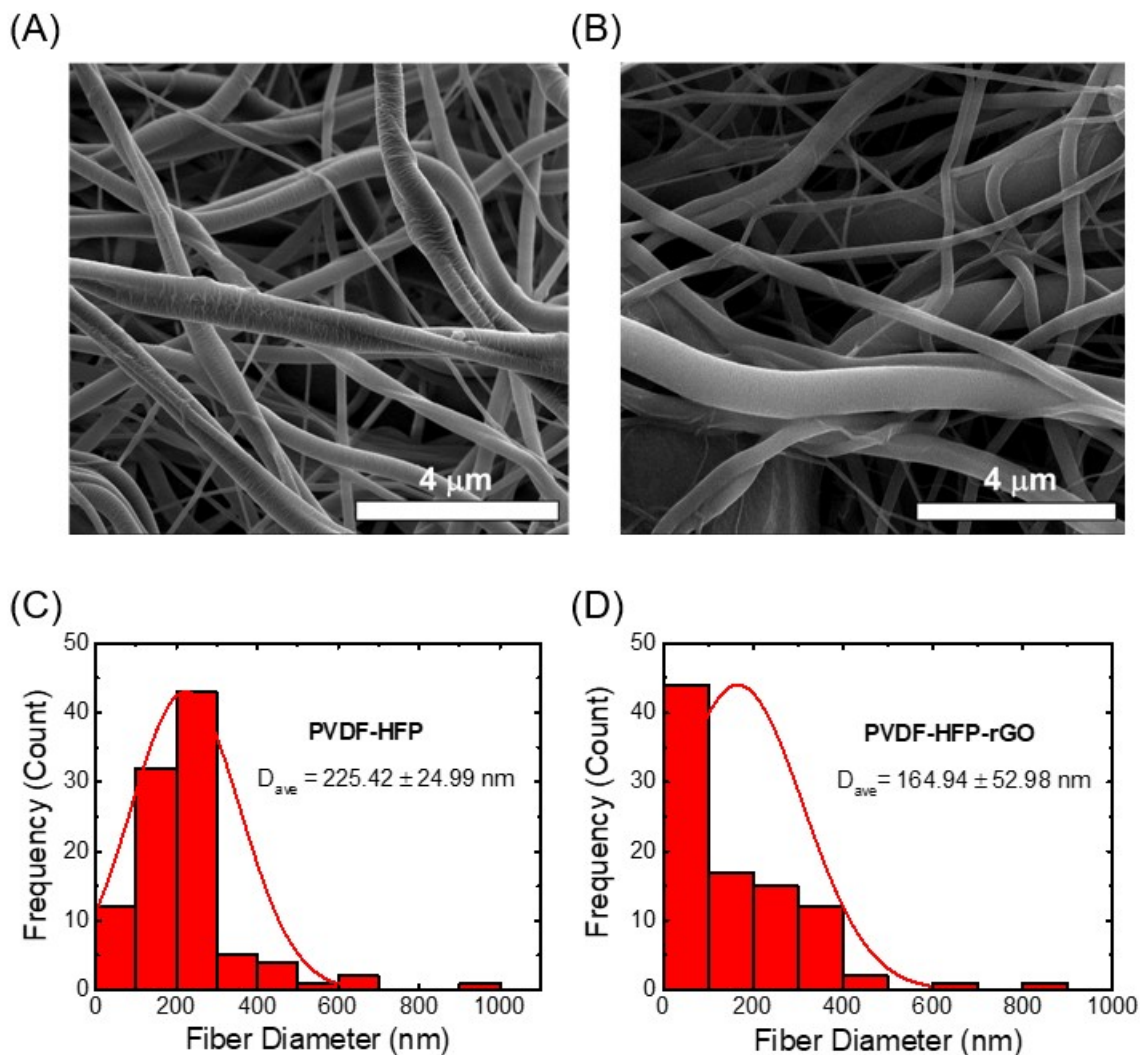


**Figure 4. 2** SEM images for (A) PVDF-HFP, (B) PVDF-HFP-rGO membranes and corresponding diameter distribution of nanofibers (C and D)

### 4.3.2 Successful incorporation of rGO investigated by Raman spectra, TGA, and XPS analysis

Raman spectroscopy was used to further investigate the changes of reduced graphene oxide nanosheets in combination with polymeric chains and the corresponding impact on the PVDF-HFP structure. The typical features of graphene-based materials under the Raman spectra are the D band (about  $1344\text{ cm}^{-1}$ ) attributable to the multiple photo scattering of defects or amorphous carbon, and the G band (about  $1600\text{ cm}^{-1}$ ) attributable to the stretching of conjugated double bonds of  $sp^2$  hybridization.<sup>113,114</sup> The intensity ratio of G band and D band (defect) characterizes the number of

defects and impurities in rGO.<sup>115,116</sup> The  $I_G/I_D = 1.20$  showed suitable crystal structure of the composite membrane and supported the successful incorporation of rGO into the PVDF-HFP matrix (**Figure 4.3**).

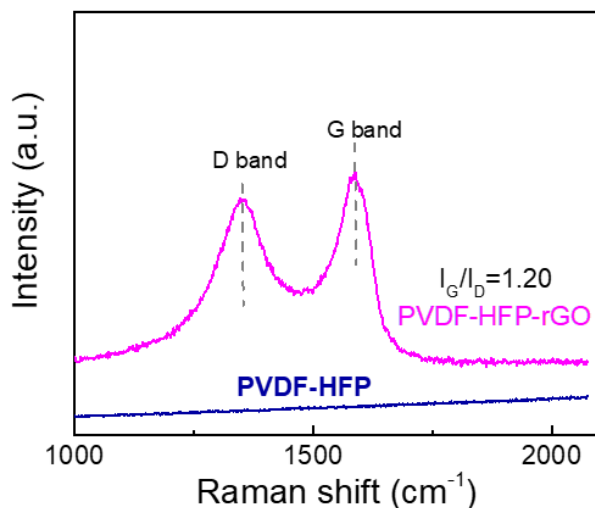


**Figure 4. 3** Raman spectra of pure PVDF-HFP and PVDF-HFP-rGO membrane.

The effect of rGO on the thermal stability of PVDF-HFP matrices was investigated by TGA analysis (**Figure 4.4**). TGA of pristine PVDF-HFP and rGO/PVDF-HFP composite membranes are shown in Figure 2B. Major weight loss of the two samples took place at 450 °C, which could be attributed to the decomposition of the PVDF-HFP matrix in these two samples.<sup>117</sup> There is no obvious difference in the decomposition temperature of pure PVDF-HFP and PVDF-HFP-rGO, which means the introduction of the rGO layers did not significantly affect the thermal stability of the polymer matrix.

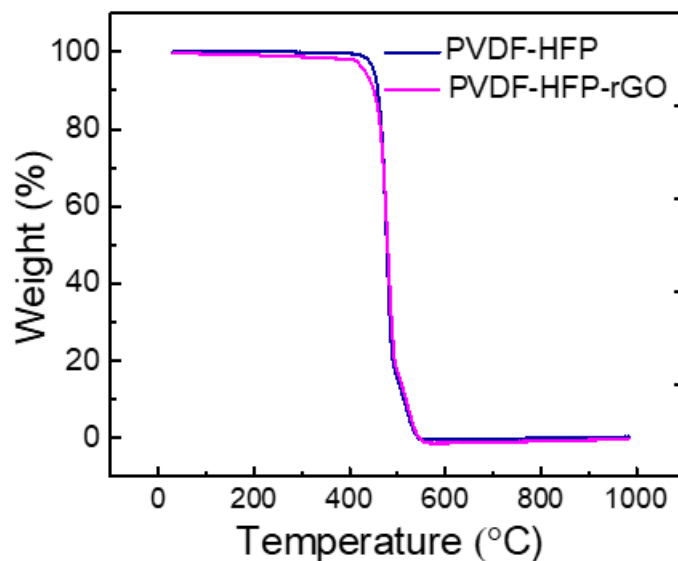


**Figure 4. 4** TGA analysis of pure PVDF-HFP and PVDF-HFP-rGO membrane.

Elemental composition of pristine and modified membranes was studied by XPS analysis and is presented in **Figure 4.5 A-B**. Results indicate the presence of C and F atoms in the pristine PVDF-HFP membrane without any trace of O atoms. The samples of reduced graphene oxide were purchased from the Cheap Tubes Company (Brattleboro, Vermont, USA). According to the product manual, elemental analysis obtained by XPS: C: 91.05%, O: 8.01%, H: 0.94%, therefore the O/C ratio in rGO is 8.8%. By incorporating rGO nanosheets into the dope solution, the intensity of the C2p peak at 293 eV increased, with another peak appearing at 520 eV, corresponding to oxygen-containing functional groups of rGO (**Figure 4.5 A**). The changes of F/C and O/C ratios in different membranes were presented in **Figure 4.5 B**. The F/C ratio decreased from 1.28 for the pristine PVDF-HFP membrane to 0.98 for the PVDF-HFP-rGO composite membrane, which could be attributed to the high density of carbon atoms in the reduced graphene oxide scaffold after successful incorporation of rGO into the polymer matrix. Moreover, the O/C ratio clearly increased in the PVDF-HFP-rGO composite membrane resulting from the epoxy, carboxyl, and hydroxyl groups in the rGO.

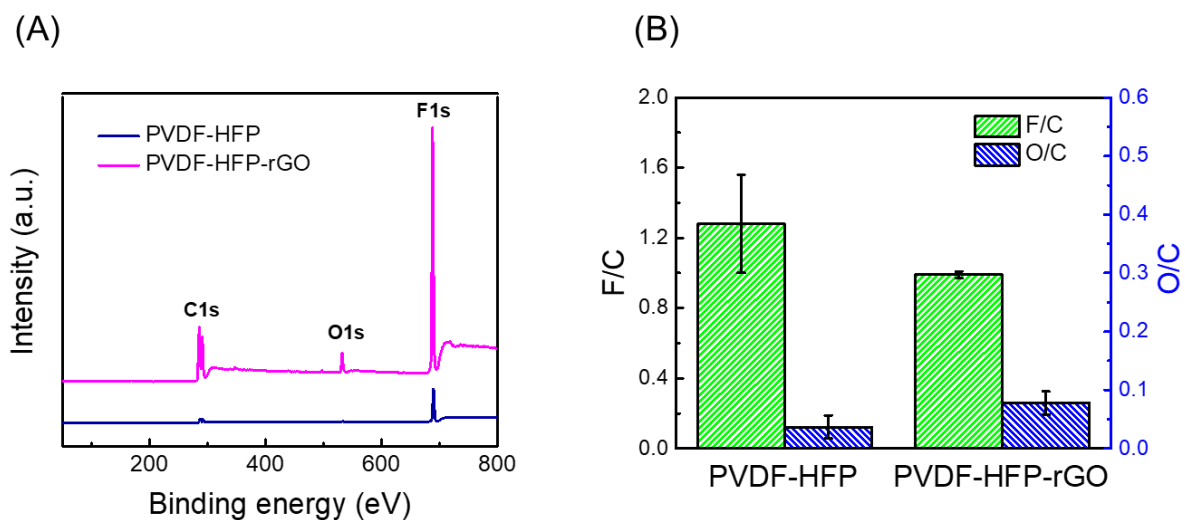


**Figure 4. 5** (A) XPS survey scans and (B) F/C, O/C ratio of pure PVDF-HFP and PVDF-HFP-rGO membrane.

### 4.3.3 Contact angle and liquid entry pressure of water (LEPw)

In general, hydrophobicity is evaluated by water contact angle, and a higher hydrophobic surface exhibits a larger contact angle. As noted, fluoropolymers usually exhibit low surface energy, which may be attributed to intensive electronegative characteristics of the element fluorine. Thus, its attractive force in relation to other substances is weak.<sup>118</sup> Due to its fluorinated composition, the electrospun PVDF-HFP nanofibrous membrane exhibited high water contact angle values around 123° (**Figure 4.6**), which confirmed its inherent hydrophobicity. Hydrophobicity was improved by introducing rGO into the polymer matrix whereby the contact angles of the PVDF-HFP-rGO membranes increased to 139°. The observed rise in hydrophobicity suggests that the incorporation of rGO significantly affected membrane wettability, as the water contact angle increased significantly.

Liquid entry pressure (LEP) is the minimum transmembrane pressure where liquids will penetrate the pores of the membrane. To avoid MD pore wetting, the hydrostatic pressure must be lower than the LEP. In the MD process, the LEP should be maintained as high as possible. The LEP value depends mainly on the material hydrophobicity and membrane pore size. The average liquid entry pressure of water (LEPw) for a pure PVDF-HFP membrane and PVDF-HFP/rGO composite membrane are shown in **Figure 4.6**. It was observed that that the PVDF-HFP-rGO membrane presented a higher LEPw value of 103.42 kPa than the original membrane (34.4 kPa), regardless

of its relatively higher porosity (**Figure 4.7**). This can be mainly attributed to the increased hydrophobicity of the rGO membrane with a high-water contact angle of  $139^\circ$  (a thickness of  $390\ \mu\text{m}$ ), which creates sufficient air pockets on the membrane surface and effectively improves the water penetrating resistance of the membrane. The LEPw value of the PVDF-HFP-rGO membrane is impressive, as most electrospun nanofiber membranes used in MD possess LEPw values lower than  $100\ \text{kPa}$ .<sup>111,119</sup>

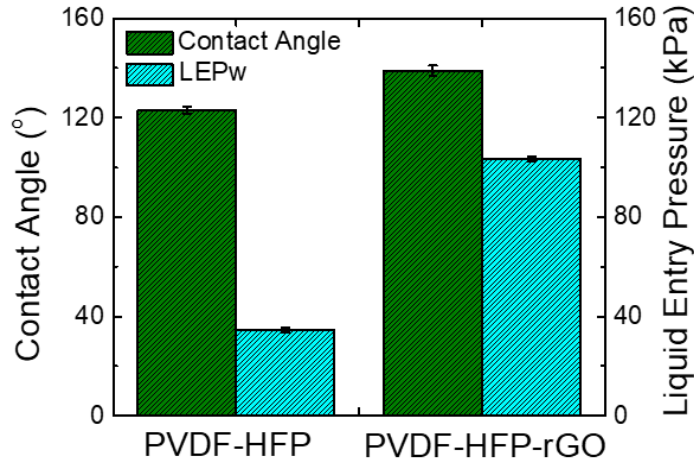


**Figure 4. 6** Comparison of contact angle and LEPw of pure PVDF-HFP and PVDF-HFP-rGO membrane.

#### 4.3.4 Porosity, Pore size, Pore size distribution

It is generally agreed that higher porosity results in less conductive heat losses through the membrane, therefore, a higher driving force and higher flux can be achieved.<sup>120</sup> MD membrane porosity values range from 30 to 85%.<sup>121</sup> As shown in **Figure 4.7**, PVDF-HFP and PVDF-HFP-rGO membranes both have the reasonably high porosities required for MD applications (79.25% and 76.45%), which can be attributed to the interconnected, open structures of the electrospun nanofiber membranes. The incorporation of rGO into the PVDF-HFP polymer matrix has very little influence on the porosity of the prepared membrane.

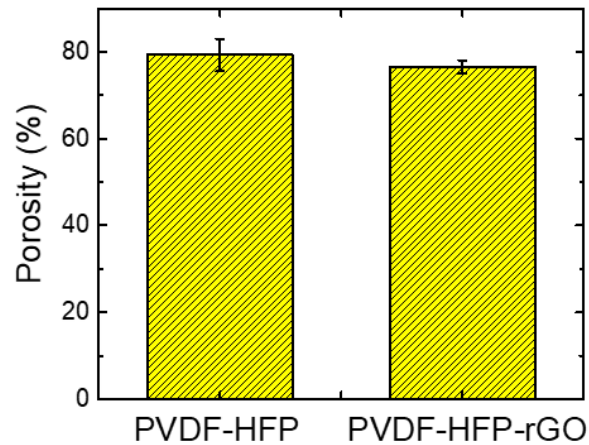


**Figure 4. 7** Porosity of pure PVDF-HFP and PVDF-HFP-rGO membrane.

Importantly, an appropriate mean pore size and a narrow pore size distribution were suggested for the permeability and selectivity of MD membranes. Higher permeate flux can be obtained at larger pore sizes, however, smaller pore sizes are also needed to avoid pore wetting. It was suggested that pore sizes should be below  $0.5 \mu\text{m}$  to avoid pore wetting.<sup>122</sup> In general, the larger fiber diameter will result in the larger pore size.<sup>123</sup> The pore size distribution should be as narrow as possible to prevent solutes from feed side passing through the membrane.<sup>124</sup> As shown in **Figure 4.8**, PVDF-HFP-rGO membranes contained a narrow distribution of pore sizes in the range of  $0.20\sim 0.92 \mu\text{m}$  with a mean pore size of  $0.47 \mu\text{m}$ . While the pristine PVDF-HFP membrane showed a relatively broader pore size distribution from  $0.22$  to  $1.22 \mu\text{m}$  with a mean pore size of  $0.55 \mu\text{m}$ . Its larger fiber diameter indicates a correlation between pore size and fiber diameter in accordance with the previous SEM analysis. The maximum pore size reduces from  $1.22$  to  $0.92 \mu\text{m}$  after rGO incorporation, a higher LEP shown in section **4.4.3** can be obtained with smaller maximum pore size from the Cantor-Laplace equation.

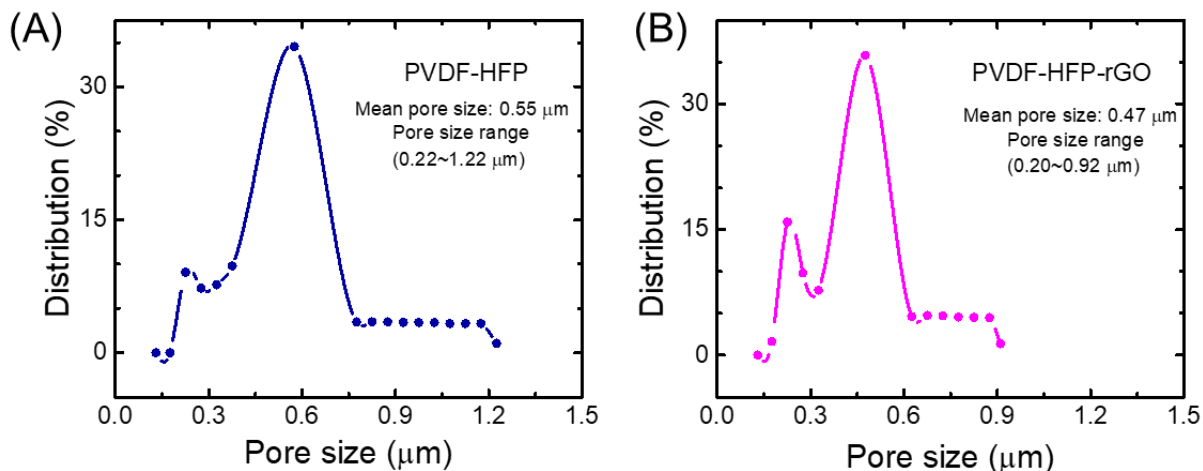


**Figure 4. 8** Comparison of pore size distribution of (A) PVDF-HFP and (B) PVDF-HFP-rGO membrane.

#### 4.3.5 DCMD performance (short-term)

Transmembrane temperature led to a significant impact on permeate flux, producing a flux around  $11.42 \text{ kg m}^{-2} \text{ h}^{-1}$  at  $\Delta T=35^\circ\text{C}$  and  $20.53 \text{ kg m}^{-2} \text{ h}^{-1}$  at  $\Delta T=50^\circ\text{C}$  (**Figure 4.9 A**). The increase in temperature difference resulted in a greater difference in vapor pressure across the membrane, creating the driving force for a higher water vapor transportation.<sup>125</sup> This positive correlation between flux and  $\Delta T$  has been demonstrated in previous DCMD studies.<sup>126</sup>

According to the literature, the thickness and the permeation flux of the membrane generally demonstrates an inversely proportional relationship.<sup>110,127</sup> Two samples with different thicknesses ( $150 \text{ μm}$  and  $390 \text{ μm}$ ) were chosen to investigate their suitability for the same feed concentration.

**Figure 4.9 B** demonstrates that for the PVDF-HFP-rGO membrane sample with a thickness of  $150 \text{ μm}$  at a temperature difference of  $50^\circ\text{C}$ , a higher water flux ( $53.05 \text{ kg m}^{-2} \text{ h}^{-1}$ ) was obtained for the feed solution of  $60 \text{ g/L NaCl}$ . However, the membrane with a  $390 \text{ μm}$  thickness exhibited a relatively lower water flux ( $20.53 \text{ kg m}^{-2} \text{ h}^{-1}$ ) at the same temperature difference and identical feed conditions. This is because the thicker membrane increased the mass transfer resistance. For both samples, the salt rejection remained at a stable value ( $99.98\%$ )—even with different thicknesses—when testing the feed solution of  $60 \text{ g/L NaCl}$  salt concentration at a temperature difference of  $50^\circ\text{C}$ . These high salt rejection and fluxes obtained are attributable to the unique structure of rGO.

Firstly, this material is hydrophobic due to high density of carbon atoms in its surface. The enhanced hydrophobicity via incorporation of rGO helps to repel the salt-water solution and delay wetting time. In addition, the hexagonal honeycomb lattice found in the  $sp^2$ -bonded carbon graphene scaffold can serve as effective sorption sites for water vapor while repelling water molecules. Due to large, non-oxidized areas inside rGO nanocapillaries, the nanochannels provide a low-friction pathway for ultra-fast water vapor transport.<sup>128</sup> However, in terms of wetting resistance, the LEPw value of the membrane of a thickness of 150  $\mu\text{m}$  was 55.1 kPa as compared with 103.42 kPa for membranes of a thickness of 390  $\mu\text{m}$ . Therefore, a thicker membrane (390  $\mu\text{m}$ ) was chosen for the long-term stability test.

In short-term experiments, pristine PVDF-HFP membranes were also tested to investigate the effect of rGO on the overall performance of DCMD. Results showed that there is no obvious decrease in flux between the PVDF-HFP membranes with and without rGO ( $22.26 \text{ kg m}^{-2} \text{ h}^{-1}$ , **Figure 4.9 C**). The similar fluxes could be attributed to the similar thermal conductivity of the pristine PVDF-HFP membrane and rGO incorporated membrane, which is consistent with the previous TGA analysis.

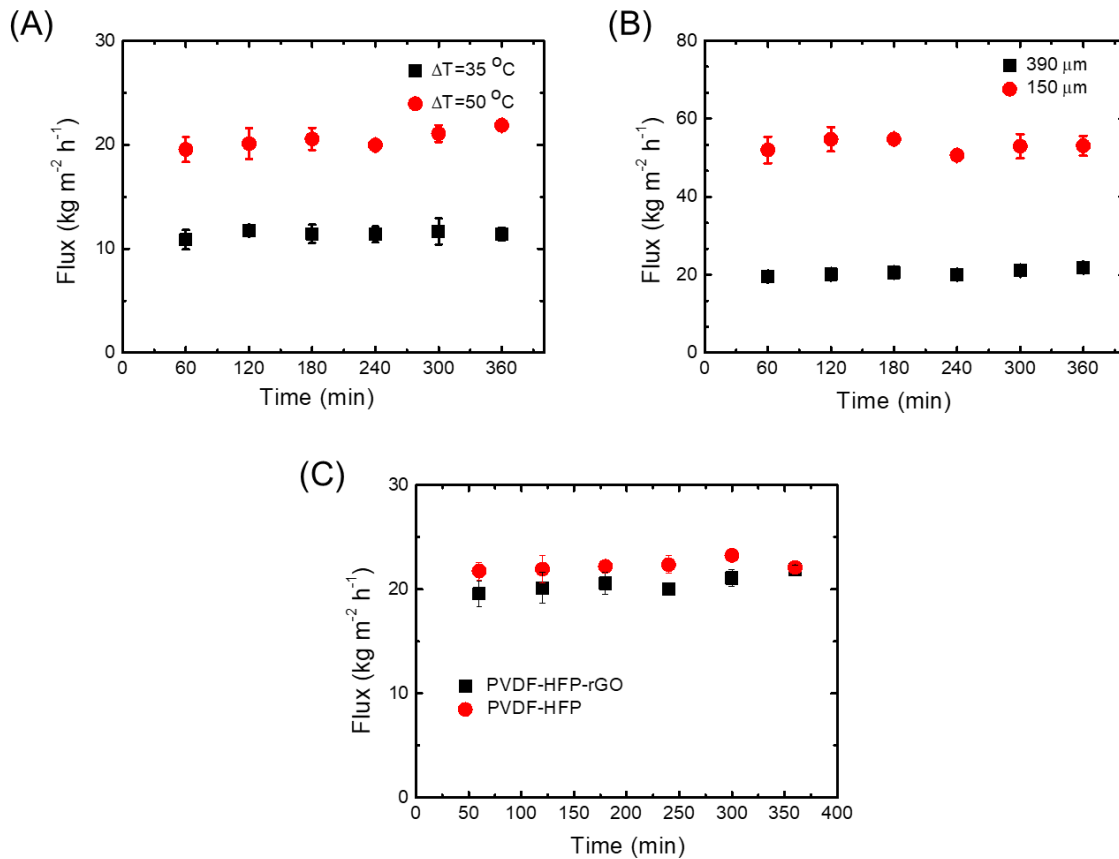


**Figure 4. 9** (A) Permeate flux versus time for the PVDF-HFP-rGO membrane (with a thickness of 390 μm) under a temperature difference of 35 °C and 50 °C. (B) Permeate flux versus time for PVDF-HFP-rGO membranes with different thicknesses. (C) Pure water flux versus time for the pure PVDF-HFP, PVDF-HFP-rGO membrane (ΔT=50 °C). Feed water was 60 g/L NaCl solution circulated at 0.75 LPM with a feed temperature of 75 °C and a distillate temperature of 25 °C.

#### 4.3.6 Long-term stability

The long-term DCMD experiment (2520 min) with the 60 g/L NaCl solution was conducted to test membrane scaling (**Figure 4.10 A**) to determine the operating time profile of permeate flux. It was observed that the flux of the PVDF-HFP membrane decreased significantly, while that of the PVDF-HFP-rGO membrane decreased only slightly. As mentioned above, the membrane used in the MD process is inclined to be wetted during the long-term operation required for the treatment of high salinity solutions.

Compared with the pristine membrane, the rGO-incorporated membrane exhibited better stability and durability. In the first 360 min, the flux of the PVDF-HFP-rGO membrane remained lower

than that of the original one. This is primarily because of the high thermal conductivity of graphene, increasing conductive heat losses as previously stated. Furthermore, pristine membrane scaling was not substantial in the initial period.

After this initial period, the PVDF-HFP membrane became more and more wetted and scaled. As a result, the PVDF-HFP-rGO membrane presented higher flux than that of the original one. The detected conductivity of the cold distillate for the PVDF-HFP-rGO membrane stabilized at about 5-20  $\mu\text{S}/\text{cm}$ , indicating that the NaCl rejection of the modified membranes was above 99.97%, which can be attributed to its higher LEPw and hydrophobicity. This result illustrates the feasibility of using rGO incorporated membranes in the the MD process. However, the permeate conductivity of the original membrane gradually increased to about 253  $\mu\text{S}/\text{cm}$  after 1380 min (as shown in **Figure 4.10 B**), indicating that the membrane pores suffered wetting due to scale formation on membrane permeate side. Inorganic scaling has been reported to suppress permeate flux as well as cause membrane wetting.<sup>129</sup> NaCl crystals grow on the surface and inside the membrane pores during distillation, and membrane wetting occurs increasingly as salt crystals grow.<sup>37</sup>

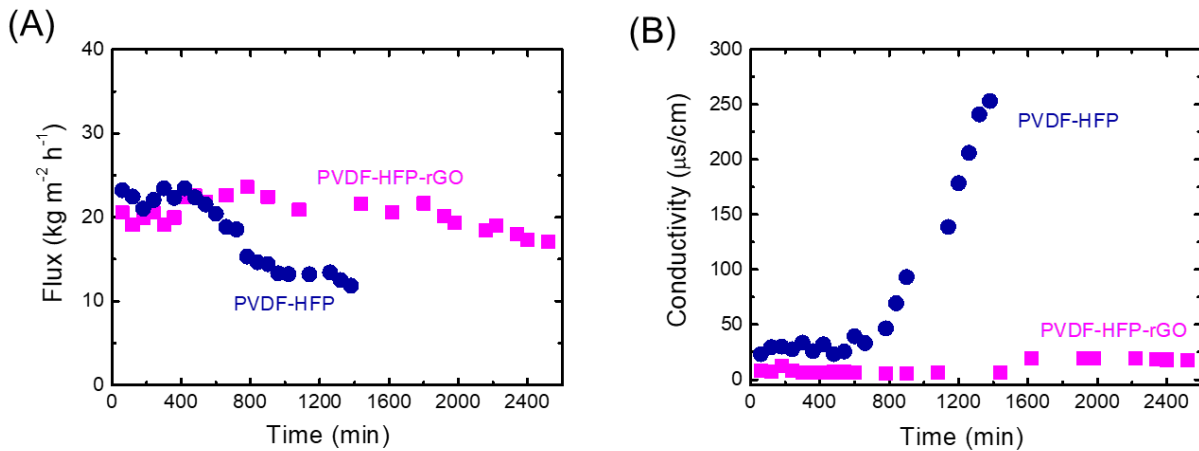


**Figure 4. 10** (A) Flux and (B) permeate conductivity vary with operating time in long-term DCMD experiments. Feed water was 60 g/L NaCl solution circulated at 0.75 LPM with a temperature of 75 °C, the distillate temperature was 25 °C with the flow rate of 0.75 LPM.

#### 4.3.7 Reported permeate flux and salt rejection of different electrospun nanofibrous membranes used for desalination.

**Table 4.1** compares the properties and DCMD performance of various PVDF nanofiber membranes developed in this work to data from the literature. In addition to a high rejection rate

of over 99.97%, the electrospun membrane with a thickness of 150  $\mu\text{m}$  offered enhancements in flux and long stable performance, attributable to the highly porous nanofibrous PVDF-HFP matrix and effective sorption of water vapor with the rGO addition.

**Table 4. 1** Comparison with different electrospun nano-fibrous membranes used for desalination.

Membrane	Feed solution		Permeate solution		Permeation flux (kg/m <sup>2</sup> h)	Salt rejection (%)	Long-term performance
	Solution	T <sub>f,in</sub> (°C)	Solution	T <sub>p,in</sub> (°C)			
PVDF-clay nanofiber <sup>130</sup>	35 g/L NaCl	80	- <sup>a</sup>	17	6	98.27	Wet in 8 h
PVDF nanofiber <sup>119</sup>	35 g/L NaCl	60	distilled water	20	11	> 99.99	Stable in 10 h
PVDF nanofiber <sup>110</sup>	30 g/L NaCl	60	distilled water	20	28	99.4	Stable in 25 h
PVDF hollow fiber <sup>131</sup>	35 g/L NaCl	79.3	ultrapure water	17.5	41.5	99.99	- <sup>a</sup>
PVDF hollow fiber <sup>132</sup>	35 g/L NaCl	70.5	distilled water	20	28.1	99.8	- <sup>a</sup>
This work	60 g/L NaCl	75	DI water	25	20.53	>99.97	Stable in 42 h
	60 g/L NaCl	75	DI water	25	53.05	99.98	- <sup>a</sup>

<sup>a</sup>: The data was not mentioned in the paper.

#### 4.3.8 Proposed mechanism for enhanced stability of rGO incorporated membrane

The proposed mechanism for enhanced stability due to the presence of rGO is shown in **Figure 4.11**. Graphene consists of a 2D sheet of sp<sup>2</sup>-bonded carbon atoms in hexagonal honey-comb lattices which serve as effective sorption sites for water vapor freed from hydrogen bonding, while repelling water molecules and salt ions.<sup>128,133</sup> At the same time, enhanced hydrophobicity via incorporation of rGO also help to repel salt-water solution. This is in line with previous published studies on oxidized carbon nanotubes.<sup>134</sup> The above factors contribute to excellent anti-scaling, anti-wetting properties, and enhanced stability of the membrane. Our research provides new facets for the future application of reduced graphene oxide to enhance hydrophobicity of MD membranes. Since oxygen-containing functional groups are found in the rGO backbone structure, various surface modifications of the rGO incorporated membrane could be considered for further membrane optimization.

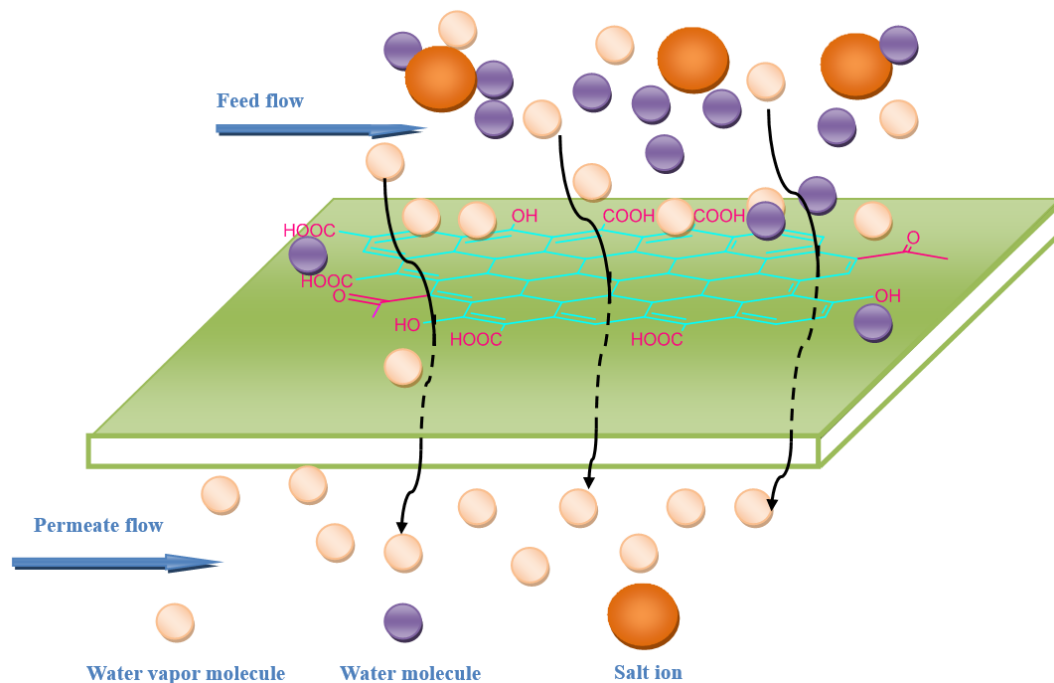


**Figure 4. 11** Schematic of proposed mechanism for PVDF-HFP-rGO membrane.

#### 4.4 Summary

Highly hydrophobic rGO/PVDF-HFP membranes were successfully fabricated by electrospinning, leading to high salt rejection and permeate flux. The membrane liquid entry pressure (LEP<sub>w</sub>) increased from 34.4 kPa to 103.42 kPa by incorporation of rGO. PVDF-HFP-rGO membranes contained a narrower pore size distribution in the range of 0.20~0.92 μm with a desired mean pore size compared with the pristine PVDF-HFP membranes. The short-term DCMD experiment with a 60 g/L sodium chloride solution showed that salt rejection of the PVDF-HFP-rGO membrane stabilized at 99.98%. The membrane was stable under the long-term DCMD experimental conditions (2520 min), achieving an average flux of 20.37 kg m<sup>-2</sup> h<sup>-1</sup> at a temperature difference of 50 °C. The detected conductivity of the cold distillate for the PVDF-HFP-rGO membrane stabilized at about 5-20 μS/cm. This facile fabrication of an rGO-incorporated membrane may open the space to lay groundwork for next-generation membranes in desalination, wastewater disposal, and food processing processes.

## **Chapter 5. Development of Robust and Superamphiphobic Membranes using Reduced Graphene Oxide (rGO)/PVDF-HFP Nanocomposite Mats for Membrane Distillation**

Membrane distillation (MD) has attracted significant attention to desalinate hypersaline water owing to its unique advantages. However, commercially available membranes used for MD desalination face fouling and wetting issues in treating wastewaters containing low surface tension contaminants (e.g., oil and alcohol) and surface-active reagent (e.g., surfactants). Herein, a superamphiphobic (i.e., superhydrophobic and near-superoleophobic) MD membrane was fabricated using electrospinning technique followed by a simple surface modification step for treating challenging wastewaters containing low surface tension substances. In order to fabricate a superamphiphobic membrane, a highly hydrophobic nanofibrous mat was first prepared by electrospinning a mixture of poly (vinylidene fluoride-co-hexafluoropropylene) (PVDF-HFP) and reduced graphene oxide (rGO). Surface superamphiphobicity was then supplemented by a facile one-step grafting of low surface energy fluoroalkylsilane. The influence of this one-step surface modification on the morphology and physicochemical properties of membranes was investigated, revealing altered elemental composition and enhanced hydrophobicity of the electrospun nanofiber mats. The resulting membranes demonstrated superamphiphobicity, confirmed by their wetting resistance evaluated with water and low surface tension liquids. The antiwetting performance of the membrane was tested through desalinating 35 g/L sodium chloride solution in the presence of a surfactant (sodium dodecyl sulfate, SDS) in the direct contact membrane distillation (DCMD) unit. Membranes modified by fluoroalkylsilane (PH-rGO-POTS) exhibited enhanced membrane distillation performance in terms of both permeation flux and salt rejection, while control membranes suffered severe wetting problems.

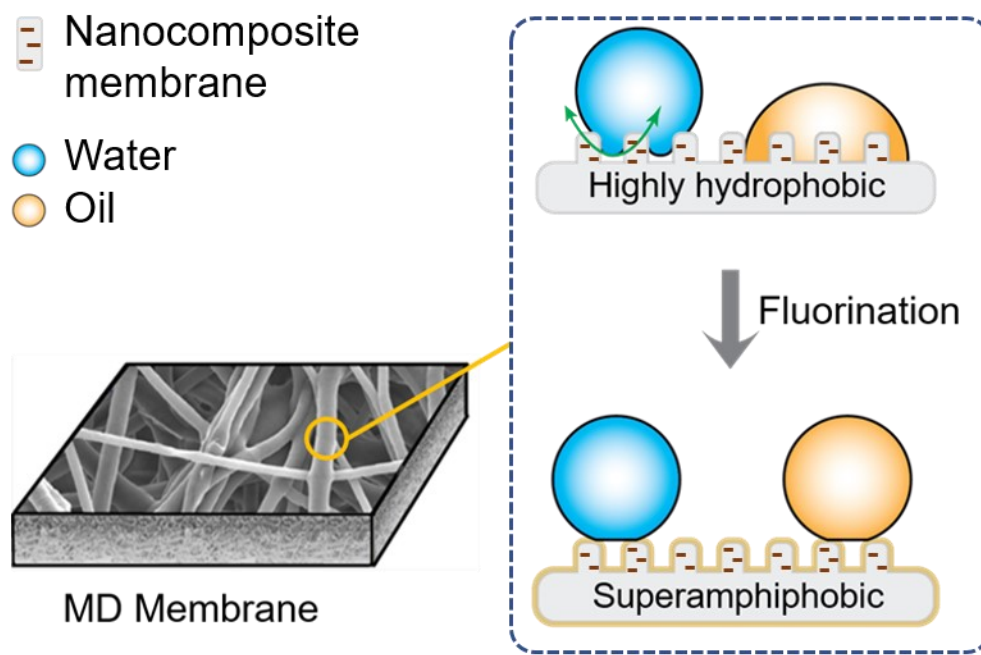


**Figure 5. 1** Graphical abstract

## 5.1 Background

Membrane distillation (MD) is an emerging, thermal-driven membrane process for desalination.<sup>135</sup> In the MD process, a hydrophobic microporous membrane is used to only allow vapor molecules passing through. The driving force for MD separation is a partial vapor pressure gradient across the membrane, typically deriving from the temperature differential between the hot feed and cold permeate streams.<sup>9</sup> MD is particularly suitable to desalinate highly saline brines where the salinity is beyond the practical limit of reverse osmosis (RO) (~70,000 ppm), such as RO brines, coal seam gas water, and shale gas/oil produced wastewater, due to its relative insensitivity to salt concentration and a theoretical 100% salt rejection.<sup>136,137</sup> Low working temperature (30-80 °C) distinguishes MD from conventional thermal distillation (60-110 °C), making it possible to utilize low-grade heat sources, such as waste heat or solar thermal energy, significantly reduces the cost.<sup>11</sup> Despite these advantages, MD is still in an early developmental stage and has not been widely applied in industrial and commercial settings. Membrane fouling and wetting are two major obstacles when using hydrophobic microporous membranes to treat challenging wastewaters. Membrane fouling is generally caused by deposition of humic acid, proteins, and oily substances onto the hydrophobic membrane through hydrophobic-hydrophobic interactions.<sup>138</sup> Moreover, deposition of inorganic species (scaling) will cause further complications.<sup>139</sup> Membrane wetting is another challenge that affects stable desalination performance of MD membranes. This phenomenon occurs when the trans-membrane pressure exceeds the liquid entry pressure (LEP), which is affected by liquid surface tension, membrane hydrophobicity, pore size, and pore shape.<sup>140</sup> In addition, conventional hydrophobic microporous membranes used in MD processes can be easily wetted by low surface tension contaminants (i.e., oil, alcohols, and surfactants) which often present in highly saline industrial waste streams,<sup>87,141</sup> contaminating the distillate and jeopardizing water treatment quality. This fouling and wetting problem restricts the application of conventional hydrophobic MD membranes to treat only wastewater free of hydrophobic and amphiphilic contaminants.

In treating challenging feed water containing low surface tension contaminants, amphiphobic modification can be effective at preventing membrane fouling and wetting. Amphiphobic surfaces with contact angles larger than 90° for both water and low surface tension liquids have recently gained popularity in a wide range of applications, including self-cleaning,<sup>142</sup> corrosion

resistance,<sup>143</sup> and anti-bacteria.<sup>83</sup> The surface amphiphobicity of solids are governed by both surface chemistry and surface morphology.<sup>144</sup> It is well-recognized that the creation of re-entrant structures in conjunction with appropriate chemical composition could create a metastable Cassie-Baxter state for the solution-membrane interfacial contact, effectively preventing membrane wetting caused by low surface tension liquids.<sup>145</sup> Therefore, the amphiphobic surface can be realized by reducing the surface free energy through functionalizing substrates with low-surface-energy materials (mainly fluorinated small molecules or macromolecules) together with engineering micro/nano reentrant structures on substrate.<sup>146</sup>

To date, there are some successful cases in which amphiphobic membranes serve as robust anti-wetting MD membrane. For example, Boo et al.<sup>10</sup> immobilized silica nanoparticles (SiNPs) with perfluorodecyltrichlorosilane (FDTS) on a phase-inversed polyvinylidene fluoride (PVDF) membrane. The SiNPs-coated PVDF membrane achieved stable performance in treating a synthetic wastewater containing surfactants (sodium dodecyl sulfate) and mineral oil, as well as with shale gas wastewater. However, to achieve a stable anchoring of nanoparticles, pre-treatment is required to create special functional groups on the membrane.<sup>147,148</sup> In addition, many attempts require the usage of special equipment, such as chemical vapor deposition reactors and plasma chambers.<sup>149</sup> Fabricating a stable, amphiphobic MD membrane through facile and cost-effective method still faces challenges.

Owning few oxygen-containing groups (e.g. hydroxyl, carboxyl, and epoxy), reduced graphene oxide (rGO) nanosheets exhibit superior hydrophobicity (water contact angle is near 125°) and it is a promising candidate to fabricate hydrophobic MD membranes.<sup>150</sup> In addition, rGO can be tailored to a wide range of potential applications with some reactive sites where further functionalization can be realized, achieving superhydrophobicity and desired nano-geometries for amphiphobic MD membrane development.<sup>151</sup> However, the potential applications of rGO in MD desalination is rarely explored.<sup>152</sup>

In this study, we proposed one simple and facile method to fabricate superamphiphobic (superhydrophobic and near-superoleophobic) nanofibrous membranes with robust anti-wetting properties for MD desalination. Highly hydrophobic nanofibrous substrates, poly (vinylidene fluoride-co-hexafluoropropylene) (PVDF-HFP) /rGO, were first prepared by electrospinning a blend of PVDF-HFP and rGO. rGO incorporated membranes (referred to as PH-rGO) exhibited

improved stability and durability with satisfactory distillate quality compared with control PVDF-HFP membranes.<sup>153</sup> The advantage of electrospun nanofibrous mats was taken of their intrinsic reentrant geometry, and the oxygen-containing functional groups on the rGO nanosheets which facilitate further modification on membrane surface. Then, low surface energy fluoroalkylsilane perfluorooctyltriethoxysilane (POTS) was coated on the nanocomposite membrane through a simple dip-coating process. We investigated the morphology, wettability properties, and surface robustness of developed membranes. Finally, we challenged the stability of the resultant superamphiphobic membrane with a model surfactant (sodium dodecyl sulfate, SDS) -containing saline solution. Our research provides new insights in developing robust superamphiphobic surfaces and fabricating novel nanofibrous membranes with excellent anti-wetting performance in MD desalination.

## **5.2 Materials and methods**

### **5.2.1 Chemicals and materials**

PVDF-HFP, DMAc, acetone, and reduced graphene oxide were used to prepare the dope solution (detailed information about the chemicals was described in Chapter 3.1). POTS (97%), tetraethyl orthosilicate (TEOS), ethyl alcohol (C<sub>2</sub>H<sub>5</sub>OH), ammonium hydroxide (NH<sub>4</sub>OH), SDS, calcium chloride (CaCl<sub>2</sub>, AR), sodium sulphate (Na<sub>2</sub>SO<sub>4</sub>, AR), and humic acid sodium salt were purchased from Sigma-Aldrich (Oakville, ON, Canada). Machine oil (90% base oil with 10% additives, density of 881.4 kg/m<sup>3</sup> at 20 °C, kinematic viscosity of 271.62 mm<sup>2</sup>/s at 20 °C, and surface tension of 29.8 mN/m at 20 °C) was received from Canadian Tire (Montreal, QC, Canada).

### **5.2.2 Preparation of superamphiphobic nanofibrous membranes**

The electrospun nanofibrous mat (PH-rGO) was prepared in a similar method reported in our previous work.<sup>153</sup> The dope solution was prepared by suspending rGO (0.15 wt%) and PVDF-HFP (15 wt%) in a mixture of DMAc/acetone (8/12, v/v) under 10 min probe sonication (Branson 3510, Shanghai, China). The mixture was then stirred overnight on a hot plate at 45 °C. Electrospinning of the dope solutions was conducted using a Nanospinner (NE300, Inovenso, Turkey) with 20 mL polymeric solutions delivered by a Luer-lock syringe (Vitaneedle, MA) at a flow rate of 4.0 mL/h. A high voltage (25 kV) was applied between the syringe nozzle and the electrically grounded

metallic drum with a rotating speed of 100 rpm. The distance between nozzle tip and collector was 15 cm. The procedure of the superamphiphobic modification is displayed in **Figure 5.2**. Electrospun mats were immersed in a solution of POTS (0.890 mL) and ethanol (30 mL) for 36 h. Coated membranes were then rinsed with deionized water three times, followed by thermal treatment at 120 °C for 4 h.

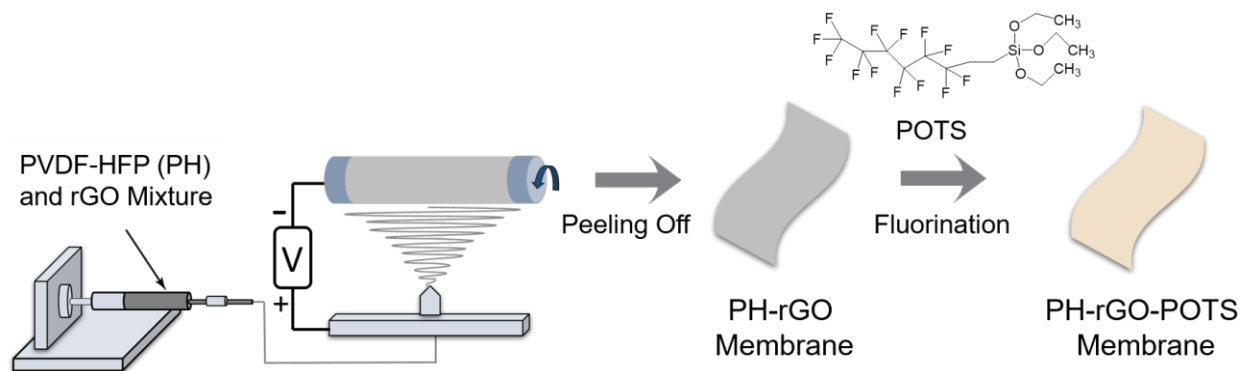


**Figure 5. 2** The schematic procedure for preparation of PH-rGO-POTS functionalized membranes through a dip-coating strategy. The PH-rGO electrospun nanofibrous mat was immersed in a mixture of POTS and ethanol for 36 h, followed by thermal treatment at 120 °C for 4 h after rinsing with deionized water.

### 5.2.3 Membrane characterization

Morphology of the resulting membranes was observed by SEM. Fiber diameter distribution and frequency were measured via ImageJ software. Silicon (Si) mapping was obtained via an EDS apparatus. The presence of rGO was investigated via Raman spectroscopy (Invia Reflex-Renishaw). The elemental composition of the membranes was evaluated by XPS. ATR-FTIR was performed to observe the functional group changes on the PH- rGO mat surface after coating POTS. The resistance to surface wetting of the membranes was evaluated by contact angle measurements of deionized water ( $\gamma = 72.5$  mN/m, diiodomethane ( $\gamma = 50.1$  mN/m) and water-ethanol mixtures ( $\gamma = 53.4\sim 22.2$  mN/m) using a video contact angle system. The water sliding angles were measured by tilting the fixed membrane samples until the water droplet started to move on the surface.

The mean pore size and pore size distribution of the as-prepared membranes were characterized by using a capillary flow porometer. The maximum pore size of the membranes was characterized by the bubble point pressure test reported in literature.<sup>154</sup>

The LEP of membrane was measured with a standard bench scale dead-end filtration setup (detailed information was described in Chapter 3.3).

#### **5.2.4 Stability of surface coating**

Thermal, mechanical, and chemical stability values of surface superamphiphobicity were evaluated under challenging conditions including boiling water (deionized water, 100 °C) for 4 h, sonication for 60 min, an acidic condition (HCl solution, pH=2), and a basic condition (NaOH solution, pH=12) at room temperature for 110 h, respectively. Water contact angle and diiodomethane contact angle of the top electrospun membrane surface were then measured at room temperature following the above procedure.

#### **5.2.5 Membrane distillation experiments**

DCMD performance experiments were conducted in the lab-scale apparatus. The hot feed solution was maintained in a constant temperature water bath. The feed solution and the cold solution were circulated at the same speed across the lower and upper face of the membrane cell respectively with two gear pumps under 0.8 psi. The circulation feed rate and permeate rate were measured by two flowmeters held constant at 0.75 LPM. The inlet temperature of the hot feed varied from 35 °C to 65 °C, while the cold side was kept at a constant 15.0 °C. The conductivity of the distillate was monitored. The water permeation flux,  $J$ , of the prepared membrane was calculated according to the equation (3-1). Salt rejection,  $R$ , was calculated by the equation (3-2).

The wetting propensity of the modified nanofibrous membranes was investigated in the presence of SDS in the feed solution. For the initial MD run, 3.5 wt% NaCl solution was used as a feed solution. The mass and conductivity of the cold side were recorded and, therefore, the real-time flux and salt rejection were calculated and monitored. After 2 hours, SDS was added to the feed stream solution to reach a final concentration of 0.3 mM to reduce the surface tension of the solution and thereby induce pore wetting. If the membranes are wetted, the feed saline solution will penetrate through the wetted portions of the membrane to the distillate side, leading to the

deterioration of MD performance with regards to permeate quality. The PH-rGO (unmodified substrate) and PH-POTS membranes were used as control samples. PH-POTS membrane was obtained by coating POTS on the PVDF-HFP electrospun nanofibrous mat to illustrate the influence of rGO addition into the substrate.

## 5.3 Results and discussion

### 5.3.1 The effect of POTS coating on membrane surface morphology

Membrane surface morphology and chemical composition are of paramount importance to membrane wettability.<sup>155</sup> Electrospinning is applied to fabricate PVDF-HFP/rGO nanofibrous mats as it facilitates MD membranes with high hydrophobicity, high porosity, and controllable thickness.<sup>156</sup> Moreover, electrospun membranes with multilevel roughness provide a re-entrant structure on nanofibers,<sup>157</sup> which is critical for realizing surface amphiphobicity. Here, the morphology of electrospun membranes before and after chemical modification was observed by SEM (**Figure 5.3 A-B**). Both membranes surfaces presented an open “three dimensional” nanofibrous interconnected structure, and the re-entrant structure was clearly observed. There was no significant difference in the diameter of fibers between substrate mat and the POTS-coated membrane (**Figure 5.3 C-D**), indicating that the fluorination process was well controlled and no obvious POTS aggregation blocked membrane pores.

Raman spectroscopy is a well-established technique for characterizing graphene-based materials, which can be used not only to identify graphene, but also to quantitatively probe the defect contents.<sup>158</sup> Both membrane samples exhibited two typical bands in the Raman spectra (**Figure A-3**): one was the D band located at around  $1344\text{ cm}^{-1}$ , representing the disorder in graphene backbone; the other one was the G band located at around  $1600\text{ cm}^{-1}$  attributable to the stretching of conjugated double bonds between the  $sp^2$ -bonded carbon atoms in hexagonal honeycomb lattices. The intensity ratio ( $I_D/I_G$ ) of the D band and the G band characterized the extent of defects and impurities in rGO.<sup>115</sup> Due to the successful coating of POTS on the rGO based substrate., the  $I_D/I_G$  slightly increased from 0.83 to 0.87.

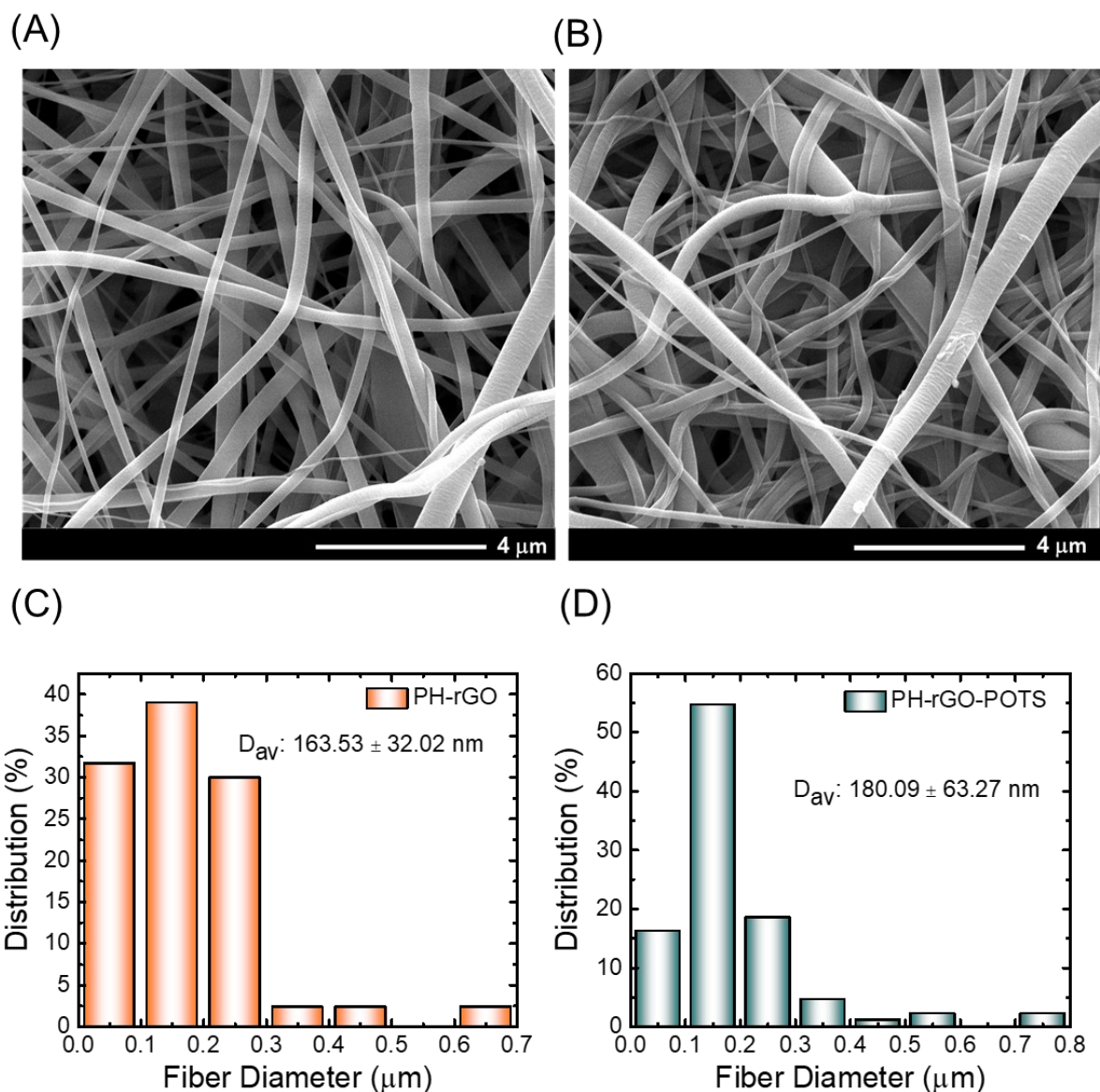


**Figure 5. 3** SEM images and corresponding fiber diameter distribution of (A, C) PH-rGO and (B, D). PH-rGO-POTS membranes.

### 5.3.2 Successful POTS functionalization confirmed by XPS and FTIR spectra

The one-step POTS tailoring on membrane was further examined by investigating characteristic elements (Si and F) and functional groups (Si-O) of POTS on membranes. Membrane surface elements were analyzed via XPS (**Figure 5.4 A**), which revealed Si peaks at binding energies of 104 eV (for Si 2p) and 155 eV (for Si 2s), implying successful coating with POTS on the PH-rGO nanofibrous substrate. In contrast, no Si peak was observed on the pristine membrane, as shown

in **Figure 5.4 A**. The ratio of F/C increased for the PH-rGO-POTS membrane (~1.45 times), suggesting a lower surface energy of the modified membranes with a higher fluorine density due to the long fluoroalkyl chain (-CF<sub>2</sub>- and -CF<sub>3</sub>) of POTS (**Table 5.1**). The respective FTIR spectra of the pristine and modified membranes are shown in **Figure 5.4 B**. The peak at 796 cm<sup>-1</sup> featured by the Si-O-Si stretching vibration and the peak around 1151 cm<sup>-1</sup> corresponding to the -CF<sub>2</sub>- stretching vibration, featured by silanol and fluoroalkyl functional groups of POTS, appeared in the spectra of the PH-rGO-POTS membrane.<sup>159</sup> These observations indicate that POTS is simply and successfully functionalized on nanofibrous membrane through one-step coating.

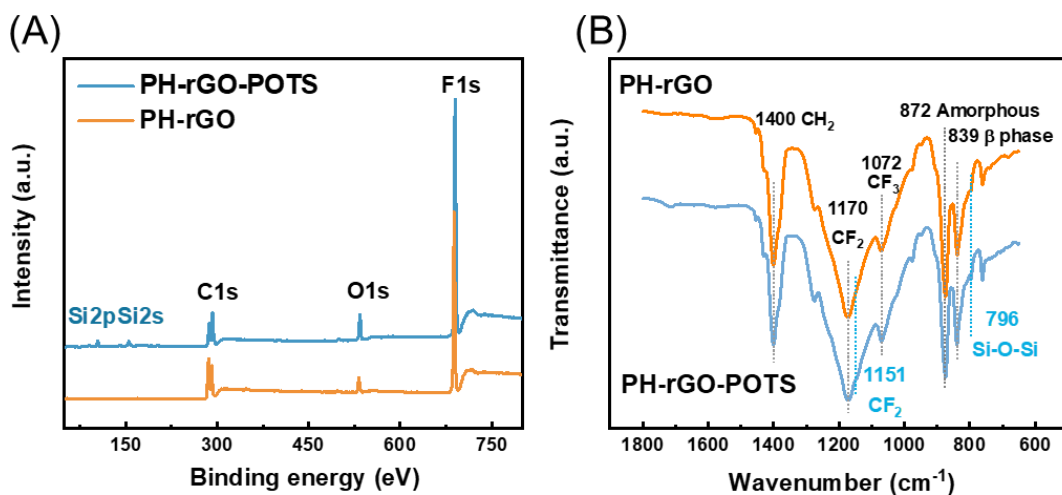


**Figure 5. 4** (A) XPS survey and (B) FTIR spectra of the pristine PH-rGO and the PH-rGO-POTS membranes.

**Table 5. 1** Elemental composition of resultant membranes.

Membrane	Atom percent (%)					
	C 1s	O 1s	F 1s	Si 2p	F/C	O/C
PH-rGO	44.54	4.16	51.3	0	1.15	0.09
PH-rGO-POTS	36.75	6.30	53.32	3.63	1.45	0.17

The EDS Si element mapping on membrane cross-section is shown in **Figure 5.5** Result showed that Si distributed across the whole membrane, which means that the POTS coating penetrates

membrane pore and binds on the fiber surface. Such a penetrated coating potentially increases robustness of membrane modification, preventing POTS layer peeling off from the nanofibrous substrate in filtration.<sup>160</sup>

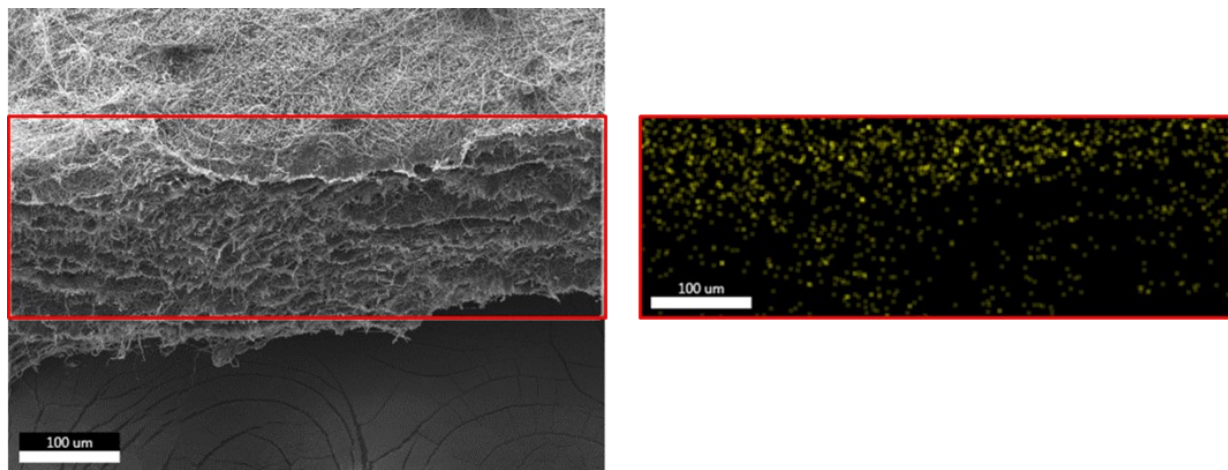


**Figure 5. 5** The cross-sectional EDS mapping images of Si element on the PH-rGO-POTS membrane.

The oxygen state on POTS-coated membrane was further analyzed via high-resolution XPS spectra collected at the binding energies of 536 to 528 eV. The peak intensity of C-OH at 534.7 eV significantly reduced after POTS coating on PH-rGO membrane, associating with the appearance of strong Si-O signal featured at 533.9 eV (**Figure 5.6 A-B**). Result further supports that silanol coupling agent, POTS, is successfully grafted on nanofibrous membrane. The hydrophobic-hydrophobic interaction together with the hydrogen bonds between the fluoride-rich alkane groups from the POTS network and the PH-rGO mat are the main driving forces that facilitate POTS binding onto the nanofibers.<sup>161</sup>

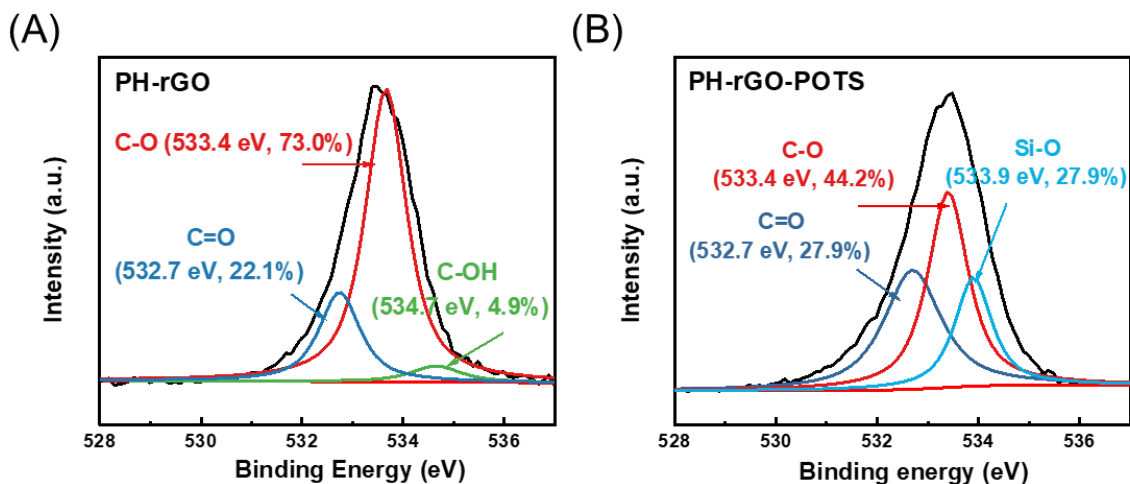


**Figure 5. 6** XPS O1s spectra of (A) pristine membrane and (B) PH-rGO-POTS membrane.

### 5.3.3 Evaluation of wettability and robustness of the membranes

Surface wettability was characterized using the static contact angle of water and diiodomethane droplets. **Figure 5.7** shows the static and sliding contact angle profiles of water for the pristine and modified membrane samples. The water contact angle of POTS modified membranes was  $153.8^\circ$  (**Figure 5.7**). Interestingly, as-prepared PH-rGO-POTS membranes exhibited a low contact angle hysteresis with sliding angle lower than  $2^\circ$  (data was not shown), indicating a superhydrophobic surface.<sup>162</sup> The liquid droplet is suspended on the top of the superhydrophobic surface and the air friction presents between the surface and liquid droplet makes suspension much easier. Nearly sphere-like droplets will form when water drops on such superhydrophobic membrane surfaces, which will readily roll off due to low contact angle hysteresis, migrating away pollutant and performing a self-cleaning property.<sup>163</sup>

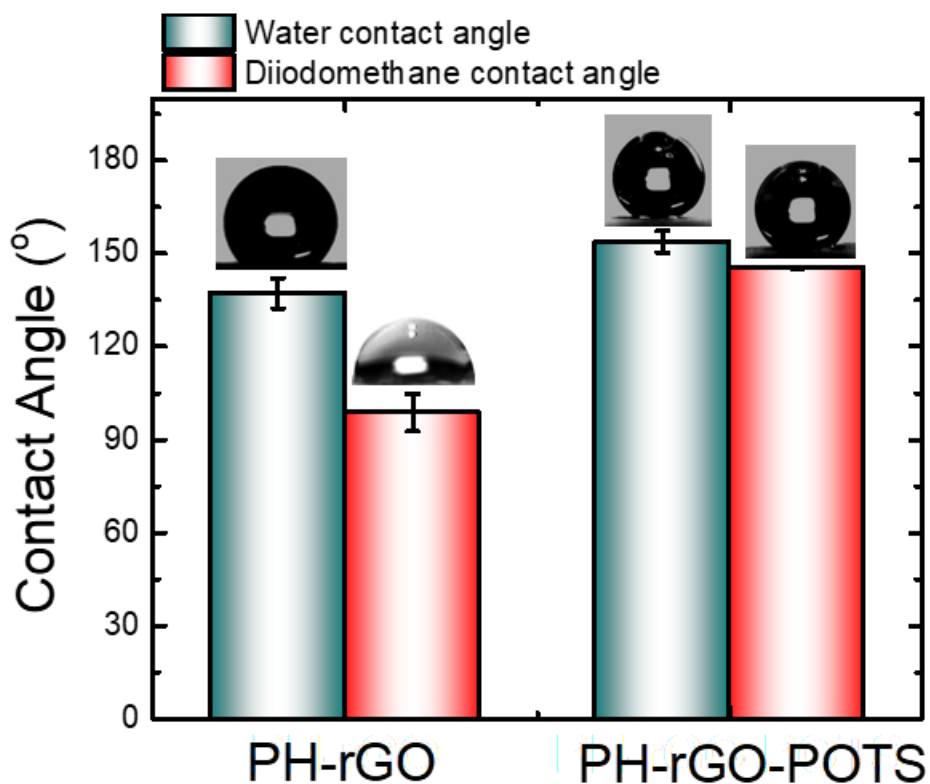


**Figure 5. 7** Contact angle profile of water and diiodomethane drops on the PH-rGO and the PH-rGO-POTS membranes.

The slippery property (high water repellency and low water adhesion) of the PH-rGO-POTS membrane was further investigated. Firstly, the as-prepared membrane was immersed in the dye (Congo Red) solution (**Figure 5.8 A**). It is clearly observed that the membrane surface possesses superior anti-wetting properties towards the dye solution. In addition, water droplets rolled freely from the horizontally placed membrane without leaving a trace (**Figure 5.8 B**). With such a slippery surface, the POTS coated membrane exhibits the self-cleaning potential. When water droplets dripped on membrane, they readily rolled off from the surface, sweeping away contaminant dusts (calcium carbonate powder) which was deposited on the membrane (**Figure 5.8 C**).

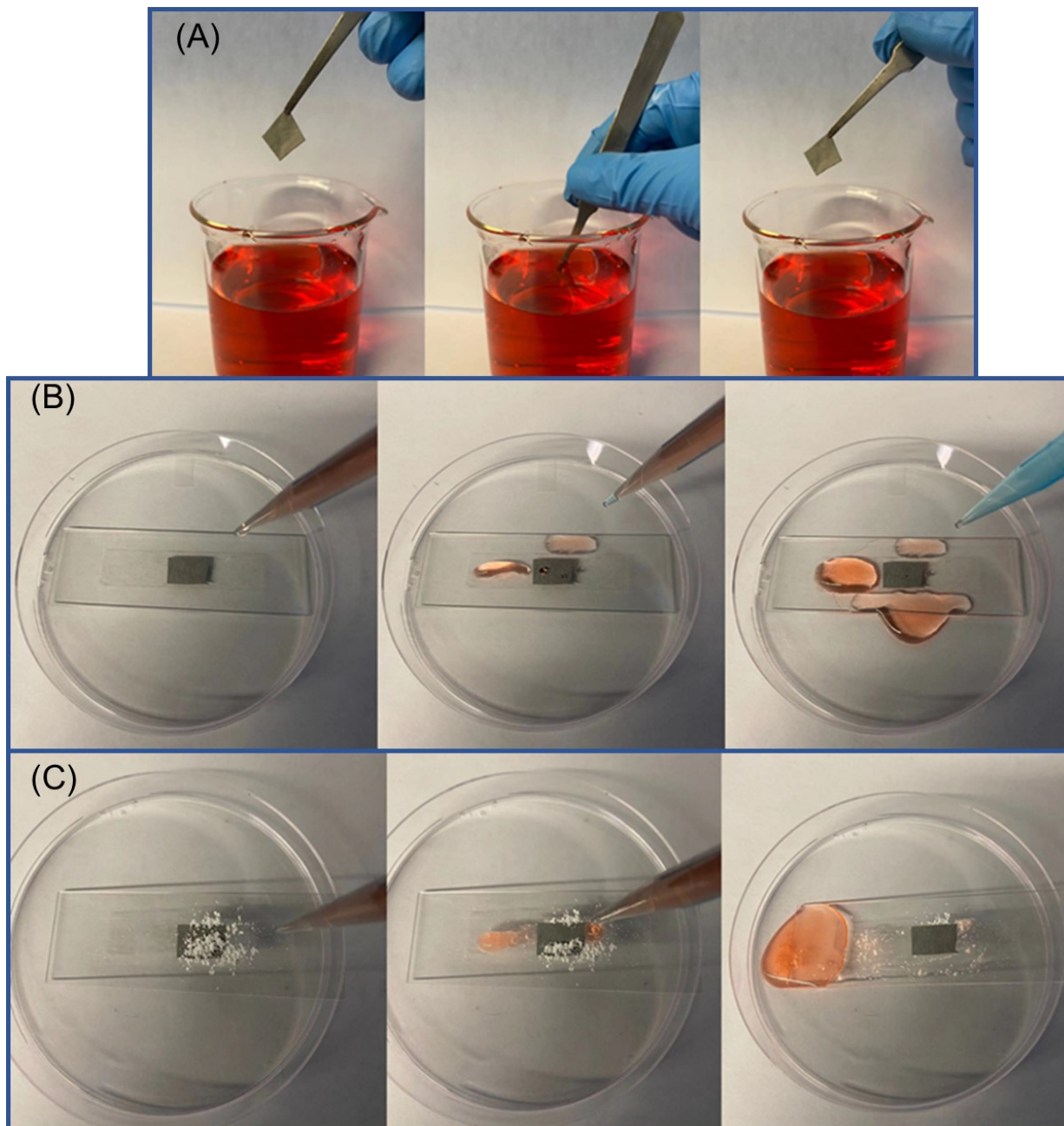


**Figure 5. 8** (A) Non-sticky test, PH-rGO-POTS membrane was inserted into dye solution and then taken out. (B) The roll-off behavior of the water droplets on the PH-rGO-POTS membrane at the horizontal state. (C) Self-cleaning behavior of the PH-rGO-POTS membrane.

In addition to superhydrophobicity, POTS modified membranes presented strong oleophobicity with a sharp increase in diiodomethane contact angle, namely from 98.7° for pristine PH-rGO to 145.3° after POTS coating (**Figure 5.9**).

To precisely assess the anti-wetting ability of the prepared membranes, the contact angles of water-ethanol mixtures with volume ratio ranging from 90:10 to 0:100, corresponding to surface tensions varying from 53.4 to 22.2 mN/m,<sup>164</sup> were evaluated (**Figure 5.9**). Owing to the hydrophobic nature and intrinsic re-entrant structure, the PH-rGO substrate exhibited high contact angles of 121.3° and 92.7° for the 10% ( $\gamma = 53.4$  mN/m) and 20% ethanol aqueous solution ( $\gamma = 43.7$  mN/m), respectively. However, the hydrophobic PH-rGO membrane was instantly wicked by the 30% ethanol aqueous solution ( $\gamma = 37.2$  mN/m). In contrast, the PH-rGO-POTS membrane exhibited great anti-wetting performance (contact angle  $>90^\circ$ ) even when it was challenged with the 80% ethanol aqueous solution which has low surface tension ( $\gamma = 24.5$  mN/m). With such superior antiwetting performance, PH-rGO-POTS membranes are expected to be stable and with high efficiency desalination in long-term MD operation.

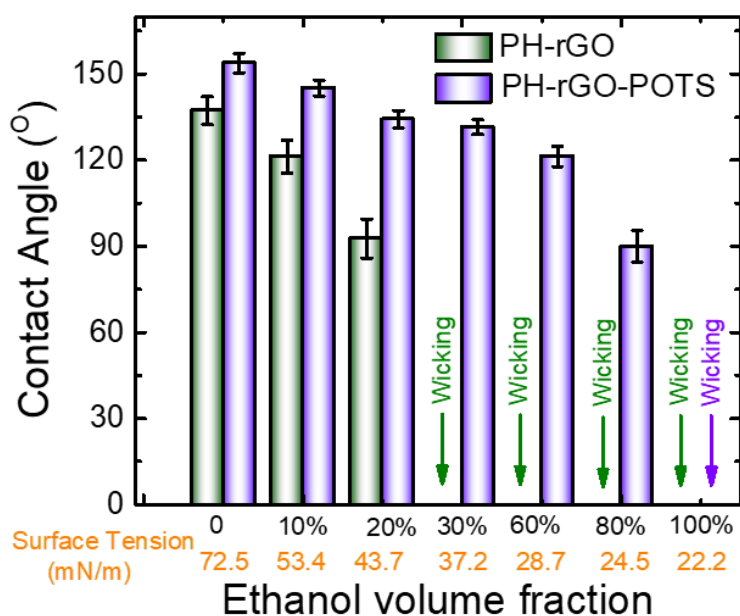


**Figure 5. 9** Contact angles of the resultant membranes facing with different water-ethanol mixtures. “Wicking” means that the membrane was wetted by the testing liquids immediately, and no stable contact angles could be measured. The error bars stand for the standard deviations of

contact angle measurements. The water-ethanol mixtures with different surface tensions are prepared following a published protocol.<sup>164</sup>

As discussed above, the electrospinning technique can be employed to form highly hydrophobic composite nanofibers with the reentrant structure required for achieving oleophobicity.<sup>165</sup> Further water and diiodomethane contact angle enhancements could be attributed to the lower surface energy created by POTS molecules. Overall, superamphiphobicity was achieved on PH-rGO nanocomposite membranes modified by POTS (PH-rGO-POTS).

The long-term stability of superamphiphobic surfaces remains a challenge for practical application. In general, the dip-coating method to fabricate a superhydrophobic membrane is not effective as the coating easily peels away from the support under complicate water environment.<sup>166</sup> Here, it is expected that the membrane modified by POTS would possess robust superamphiphobicity due to the hydrophobic-hydrophobic interaction together with the hydrogen bonds between the rGO and POTS molecules. To further evaluate the chemical and mechanical stability of superamphiphobic modification, PH-rGO-POTS membranes were challenged in difficult conditions, such as boiling water, strong acid, and base solutions, after which contact angles of membranes were determined with water and diiodomethane, respectively. Results shown in **Figure 5.10** revealed that the water and the diiodomethane contact angles of modified membranes remained constant after the challenging treatments, including 4 h boiling in DI water, 110 h etching in HCl and NaOH solutions, and sonication for 1 h, respectively. Moreover, the challenged PH-rGO-POTS membrane maintained similar morphology with that of a freshly prepared one. These observation demonstrates that the POTS coating could firmly adhere to PH-rGO nanofibers and withstand these harsh treatments. All results suggest that the modified membranes are very stable and exhibit excellent superamphiphobicity, showing great potential to treat challenging wastewater.

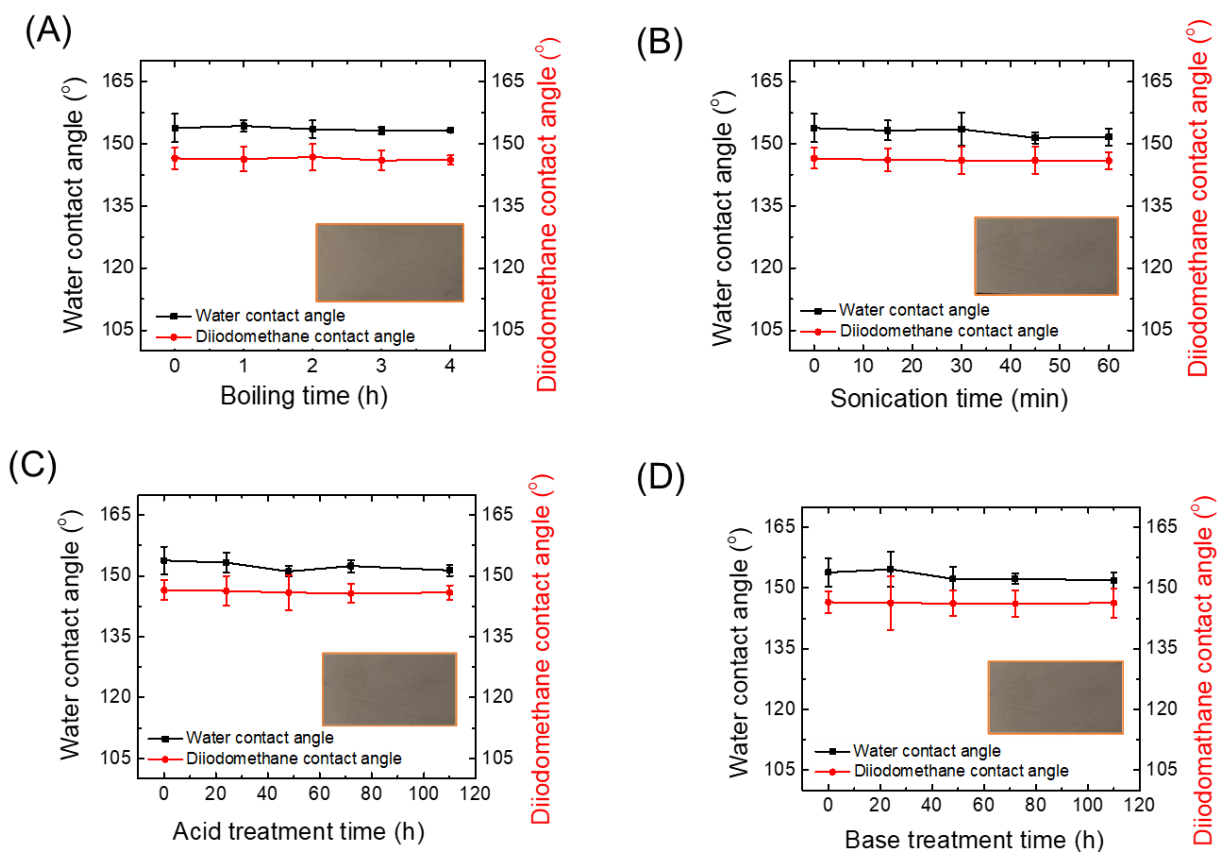


**Figure 5. 10** Water contact angle (black) and Diiodomethane contact angle (red) of PH-rGO-POTS membranes after challenging with (A) boiling water for 4h, (B) sonication for 60 min, (C) strong acid (HCl, pH=2) for 110 h, and (D) base solution (NaOH, pH=12) for 110 h. The error bars in the figures stand for standard deviation. Insets are optical photos of PH-rGO-POTS membranes after various treatments.

### 5.3.4 Membrane properties and DCMD performance

Pore size and pore size distribution (PSD) are crucial parameters in the performance of MD. An optimal pore size is needed to balance between high permeate flux and pore wetting resistance. In addition, different pore sizes can exhibit different flow mechanisms.<sup>28</sup> PH-rGO-POTS membrane exhibited a PSD from 0.1 to 0.90  $\mu\text{m}$ , while the unmodified substrate ranging from 0.1 and 1.01  $\mu\text{m}$ . Membranes with a narrow PSD favor prevention towards liquid penetration,<sup>167</sup> which can be further confirmed from the LEP value. As shown in **Figure 5.11**, PH-rGO-POTS exhibited a higher LEP (122.7 kPa) than that the PH-rGO substrate (104.5 kPa), attributing to the higher

contact angle and lower maximum pore size after modification, beside its closely linked nanofibrous network structure.

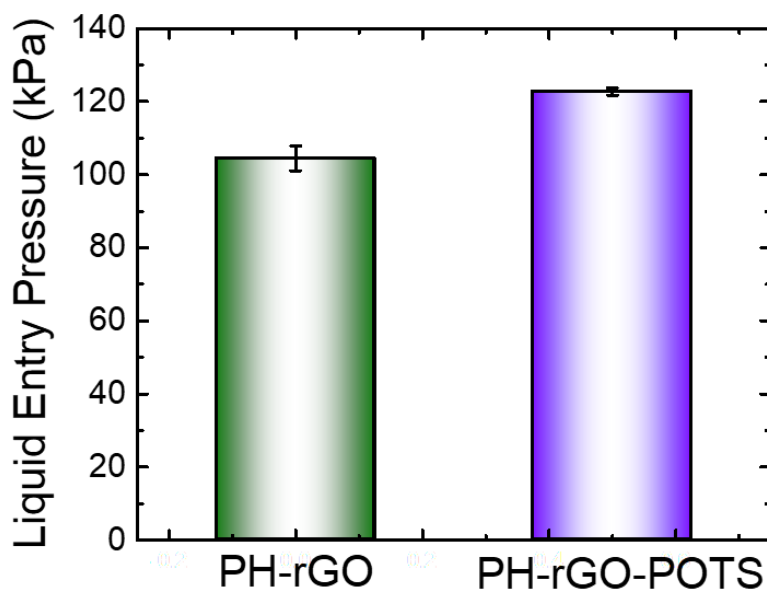


**Figure 5. 11** The LEP value for the membrane samples in this work.

DCMD tests were conducted using NaCl solution as feed to investigate the performance of modified membranes. The effect of specific parameters, such as feed temperature and feed salt concentration were analyzed for the product water. **Figure 5.12 A** shows the effect of temperature difference,  $\Delta T$  (feed-permeate temperature difference), on the water flux. According to the observation, the higher temperature differences increase permeate flux, varying from  $6.6 \text{ kg m}^{-2} \text{ h}^{-1}$  to  $28.23 \text{ kg m}^{-2} \text{ h}^{-1}$  for temperature differences from  $20 \text{ }^\circ\text{C}$  to  $50 \text{ }^\circ\text{C}$  (with permeate side fixed at  $15^\circ\text{C}$ ). This phenomenon can be explained by the increased vapor pressures and heat transfer at higher temperature differences. **Figure 5.12 B** shows the effect of salt concentration (in grams/liter) on product water flux. The increment of feed concentration from 0 to 60 g/L only leads to a slight reduction ( $\sim 12.2\%$ ) in the permeate flux of PH-rGO-POTS membrane. Meanwhile, the permeate conductivity stayed below  $4.5 \text{ } \mu\text{S/cm}$ , indicating a near complete rejection of the salts. This observation confirms our hypothesis that the as-prepared superamphiphobic membrane (PH-rGO-POTS) can sustain high salinity and perform well in desalination. The slight flux decline is likely caused by the decrease in water activity as salt concentration increases.<sup>168</sup> Additionally, a thicker boundary layer may be developed in the membrane-solution interface at higher salt concentrations.

The aggravated concentration and temperature polarization effects further reduce the driving force for evaporation.<sup>169</sup>

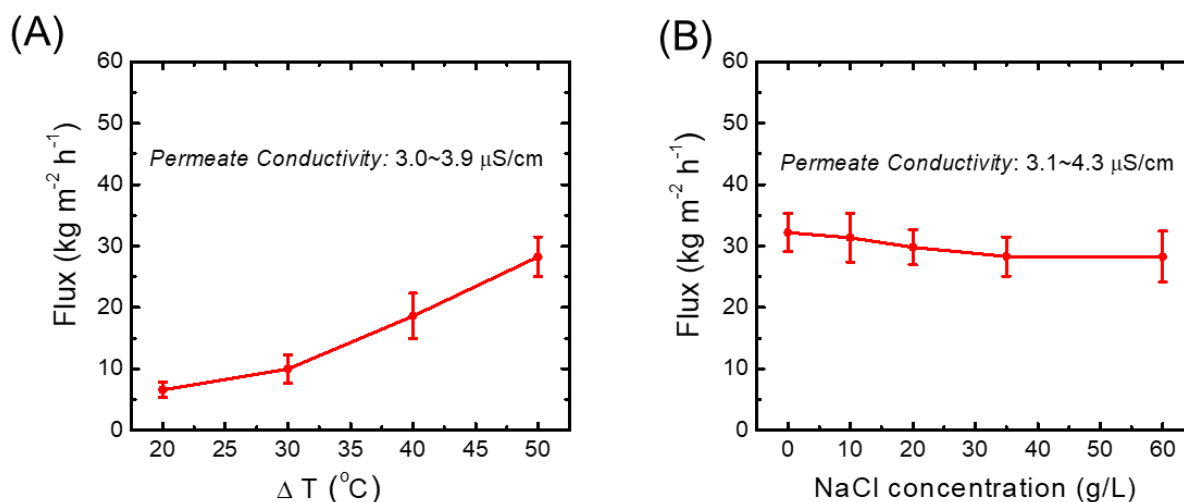


**Figure 5. 12** (A) Water flux of the PH-rGO-POTS membranes under various temperature differences; the temperature of the feed varied from 35 °C to 65 °C, while the permeate side was kept as constant, 15.0 °C. (B) Water flux of the PH-rGO-POTS membrane under different NaCl concentrations with the temperature difference maintained at 50 °C. The error bars in the figures stand for standard deviation. The flow rate of feed and permeate streams were both 0.75 LPM.

SDS is a popular surfactant in wastewater treatment, decreasing the surface tension of wastewater<sup>170</sup> which normally wets the MD membrane and diminishes its performance.<sup>171</sup> In this study, sequential dosing of SDS was introduced into 3.5 wt% NaCl feed solution to challenge the membrane wetting resistance during the DCMD process. In the initial addition of 0.1 mM SDS, water flux for PH-rGO (unmodified substrate), PH-POTS (control), and PH-rGO-POTS membranes were stable with salt rejection rates always near 100% (**Figure 5.13 A-B**). However, severe wetting was observed on the PH-POTS membrane as indicated by the sharp reduction of water flux and salt rejection after the introduction of 0.2 mM SDS to the feed. The PH-rGO membrane showed a stable MD performance without changes in the water flux for 0.2 mM SDS in the feed; while the flux performance and permeate quality dramatically decreased after 0.3 mM SDS was added. A similar observation is reported in the literature.<sup>171</sup> In contrast, the PH-rGO-POTS membrane maintained a stable water vapor flux and almost complete salt rejection (~100%)

even after 0.3 mM of SDS addition, indicating its high resistance to wetting with low surface tension liquids.

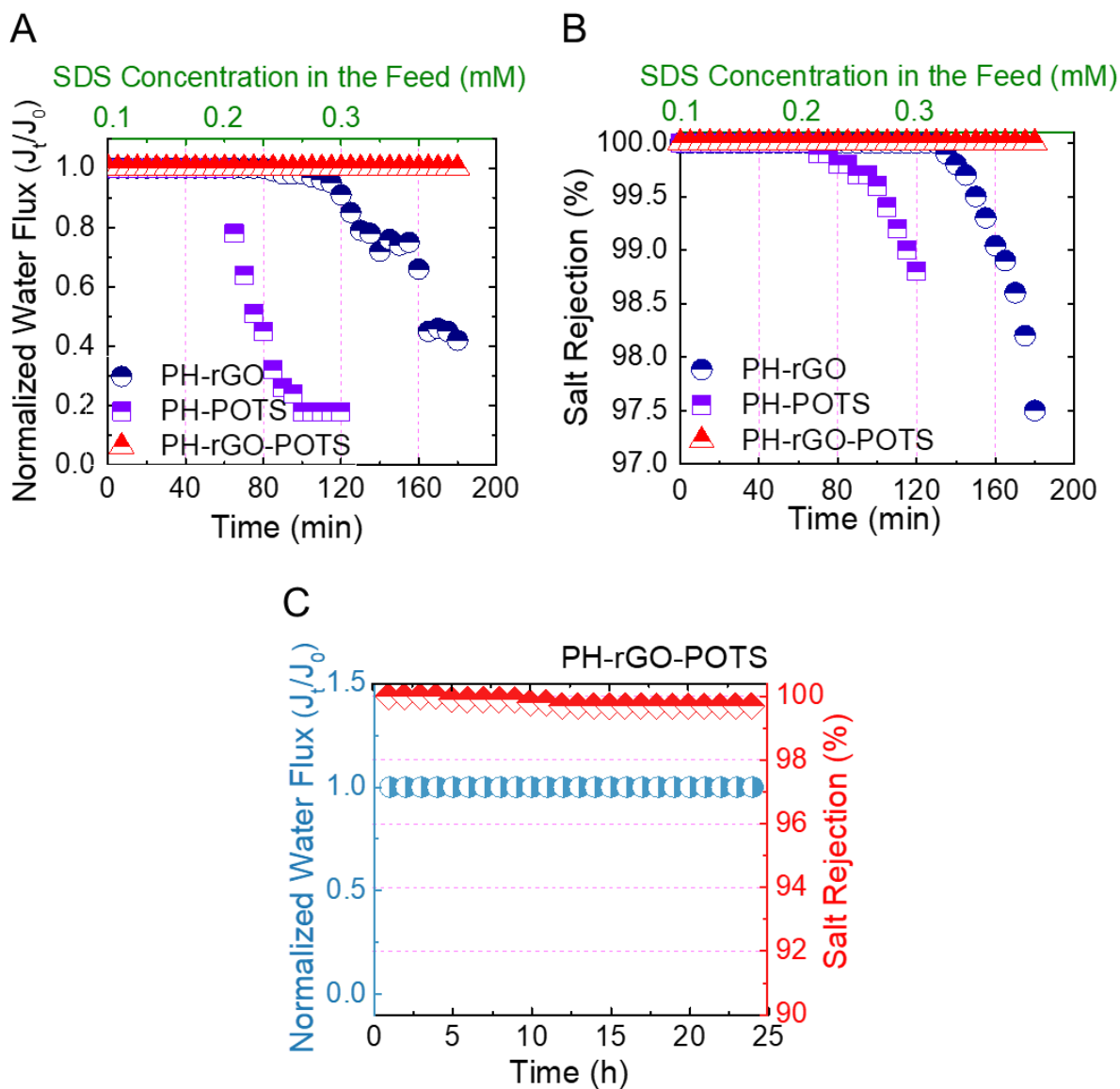


**Figure 5. 13** (A) Water flux and (B) permeate conductivity of PH-rGO (unmodified substrate), PH-POTS (control), and PH-rGO-POTS membranes in DCMD. A 3.5 wt% NaCl solution with increased addition of SDS from 0.1 mM to 0.3 mM was used as feed solution maintained at 65 °C and deionized water was used as a permeate cooling solution maintained at 15 °C. (C) Long-term stability of PH-rGO-POTS membranes in the presence of mixed foulants (35 g/L NaCl, 20 mM CaCl<sub>2</sub>, 20 mM Na<sub>2</sub>SO<sub>4</sub>, 100 mg/L humic acid sodium salt, 10 mg/L machine oil and 0.05 mM SDS). The flow rate of feed and permeate streams were both 0.75 LPM.

As the surface tension of the feed reduced due to an increased dose of SDS, the liquid-air interface sagged, feed solution impinged upon the next layer of fibers, leading to a state transition on membrane from Cassie-Baxter to the Wenzel state.<sup>172</sup> Some larger pores became flooded by the SDS solution as their liquid entry pressures were reduced to levels lower than the hydraulic pressure in the feed channel, hence partially wetting of the membrane occurred.<sup>141</sup> The penetration of the feed solution into the membrane pores resulted in a substantial increase in the mass transfer resistance against vapor molecules diffusion.<sup>72</sup> Overall, the presence of surfactants in the feed solution could render the membrane surface hydrophilic, reducing the LEP and facilitating the leakage of salty liquids through membranes.<sup>173</sup>

Interestingly, the unmodified substrate PH-rGO was not wetted immediately once the SDS was added into the feed, indicating resistance against low surface tension solutions and its ability as a substrate targeting superamphiphobic membranes. The enhanced anti-wetting properties of PH-rGO-POTS nanofibrous membranes—as compared to control membranes (unmodified substrate, PH-rGO, and the PH-POTS membrane without rGO incorporation in the substrate)—was attributed to the low surface energy on membrane after POTS modification. While the direct surface coating of POTS on the PH substrate failed to achieve superamphiphobicity, which was confirmed by its low anti-wetting performance towards ethanol solutions (>30 vol%) and lower LEP value (**Figure 5.14**). It was noted that the cylindrical fiber structures of the electrospun nanofiber mat, PH-rGO provided primary re-entrant structure, and the POTS coating offered further low surface energy properties, preventing membrane wetting by the solution. The slippery property of the PH-rGO-POTS membrane can hinder both heterogeneous nucleation and deposition of salts.<sup>174-176</sup>

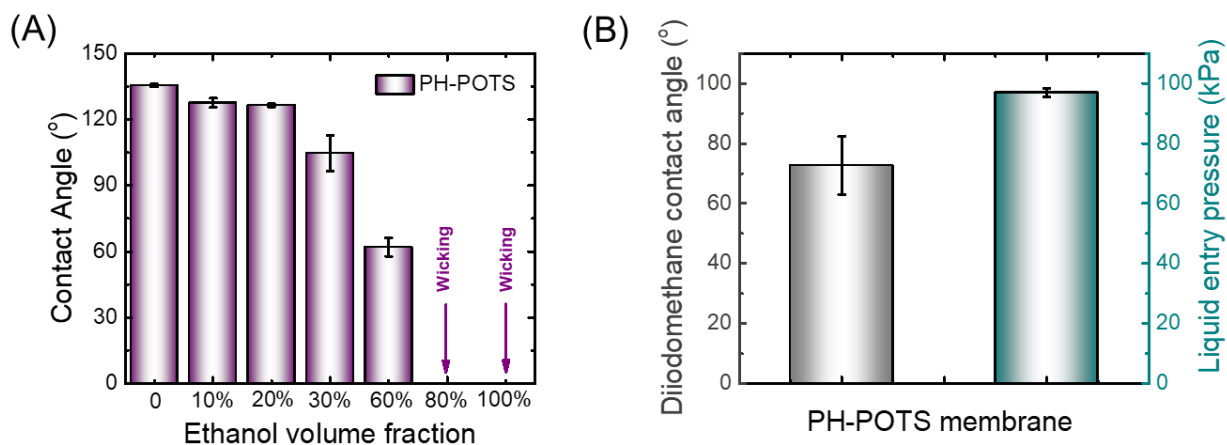


**Figure 5. 14** (A) Contact angles of the PH-POTS membrane with different ethanol concentrations. (B) Diiodomethane contact angle (grey) and LEP (blue) of the PH-POTS membrane.

To comprehensively investigate the stability of the superamphiphobic membrane, a variety of foulants including both inorganic salts and organic compounds were added to the feed solution. A synthetic feed solution with high concentration salinity was prepared here to challenge the fouling and wetting resistance of PH-rGO-POTS membrane, which contained 35 g/L NaCl, 20 mM CaCl<sub>2</sub>, 20 mM Na<sub>2</sub>SO<sub>4</sub>, 100 mg/L humic acid sodium salt, 10 mg/L machine oil, and 0.05 mM SDS. As shown in **Figure 5.13 C** and **Figure A-4**, PH-rGO-POTS membrane exhibited stable permeate flux with a water recovery of 57.0% and a high salt rejection (>99.7%) for 24 hours of continuous DCMD operation. Considering the feed solution is very harsh with various contaminants in high concentrations, the long-term wetting of membrane is predictable, and the salt rejection is within the acceptable value.<sup>177,178</sup>

We further compare the modification method and MD performance of amphiphobic membranes developed in this work to previous studies (**Table 5.2**). Based on this comparison, the one-step tailoring of robust superamphiphobicity described in this work would provide a new route towards the fabrication of robust, anti-wetting MD membranes without sacrificing the water flux, and requiring no involvement of membrane surface activation and special equipment (plasma, CVD reactors, etc.).

**Table 5. 2** Comparison of amphiphobic membranes for membrane distillation.

Substrate	Modification method	Amphiphobicity	Feed composition	$\Delta T$	Performance
<b>PVDF-HFP nanofiber</b> <sup>175</sup>	SiNPs grafting + fluorination	CA: water 150°; oil 135°	58 g/L NaCl + 0.3 mM SDS	40 °C	12.5 LMH; SR ~100%
<b>PVDF-HFP nanofiber</b> <sup>179</sup>	One-step electrospinning	CA: water 154°; oil 148°	35 g/L NaCl + 0.3 mM SDS	40 °C	8 LMH; permeate conductivity ~2 $\mu$ S
<b>PVDF Nanofiber</b> <sup>149</sup>	CF <sub>4</sub> plasma treatment	CA: water 160°; oil > 140°	RO brine + 0.7mM SDS	40 °C	15.28 LMH; SR ~100%
<b>PVDF flat Sheet</b> <sup>71</sup>	SiNPs and polystyrene grafting + fluorination	CA: water 176°; hexadecane 138°; water sliding angle 7°	emulsion of SDS + hexadecane + NaCl	40 °C	~9 LMH; permeate conductivity ~50 $\mu$ S
<b>PVDF flat Sheet</b> <sup>180</sup>	SiNPs deposition and fluorination	CA: water and oil, > 160°; water sliding angle: 1.1°	RO brine +20 mg/L humic acid	40 °C	11.22 LMH; SR ~100%
<b>PVDF-HFP/rGO nanofiber (this work)</b>	One step fluorination	CA: water 153.8°; diiodomethane 145.3°; water sliding angle of 1.8°	35 g/L NaCl + 0.3 mM SDS	50 °C	~27 LMH; SR ~100 %

## 5.4 Summary

In this study, we present a facile approach to fabricate superamphiphobic nanofibrous membranes by functionalizing POTS onto the PH-rGO nanofibrous substrate. The POTS-modified membrane (PH-rGO-POTS) displayed superhydrophobicity with water contact angles larger than 150° and sliding angles lower than 2°, indicating their self-cleaning properties. Moreover, this as-prepared membrane exhibited large diiodomethane contact angles of 145.3°. The superamphiphobicity stems from the synergistic effects of the re-entrant structure provided by electrospun nanofibrous substrate and the low surface energy offered by the POTS coating. The modified membrane also exhibited excellent superamphiphobic stability in harsh treatment conditions. Furthermore, the resultant superamphiphobic membrane presented a robust performance with a relatively high flux

and desired permeate quality in the presence of 0.3 mM SDS during the DCMD process, compared with the control membranes. This demonstrated the outstanding anti-wetting properties of superamphiphobic membranes. Overall, we demonstrated an effective anti-wetting MD membrane where low surface energy modifier was introduced on the rGO based polymeric substrate without using pretreatment and complicated equipment. Given the simplicity of the approach, combined with robust chemical, thermal and mechanical stability, this strategy provides avenues for the fabrication of robust superamphiphobic MD membrane for application in various wastewater treatments.

## **Chapter 6. Mesoporous MCM-48 Silica Nanospheres Incorporated PVDF-HFP Membrane with Highly Enhanced Permeate Flux in Membrane Distillation Process**

In this study, mesoporous MCM-48 silica nanoparticles with controlled particle sizes were prepared under mild conditions and hydrophobilized with vinyl groups. We then—for the first time—fabricated a novel hybrid PVDF-HFP/MCM-48 electrospun nanofibrous membrane by incorporating vinyl-modified MCM-48 nanoparticles into the PVDF-HFP polymer matrix. The addition of hydrophobic MCM-48 nanoparticles was found to significantly increase water vapor transport, with a flux enhancement 87.16% greater than that observed in the pristine PVDF-HFP membrane during direct contact membrane distillation operation. The PVDF-HFP/MCM-48 hybrid membrane exhibited stable flux and the permeate conductivity remained less than 8.0  $\mu\text{S}/\text{cm}$  when tested with feed solutions containing 35 g/L NaCl and 1.26 g/L  $\text{CaCl}_2$  in the long-term experiments. Overall, this work provides an insight into the development of highly permeable membranes for membrane distillation applications by employing porous MCM-48 silica as a nanofiller.

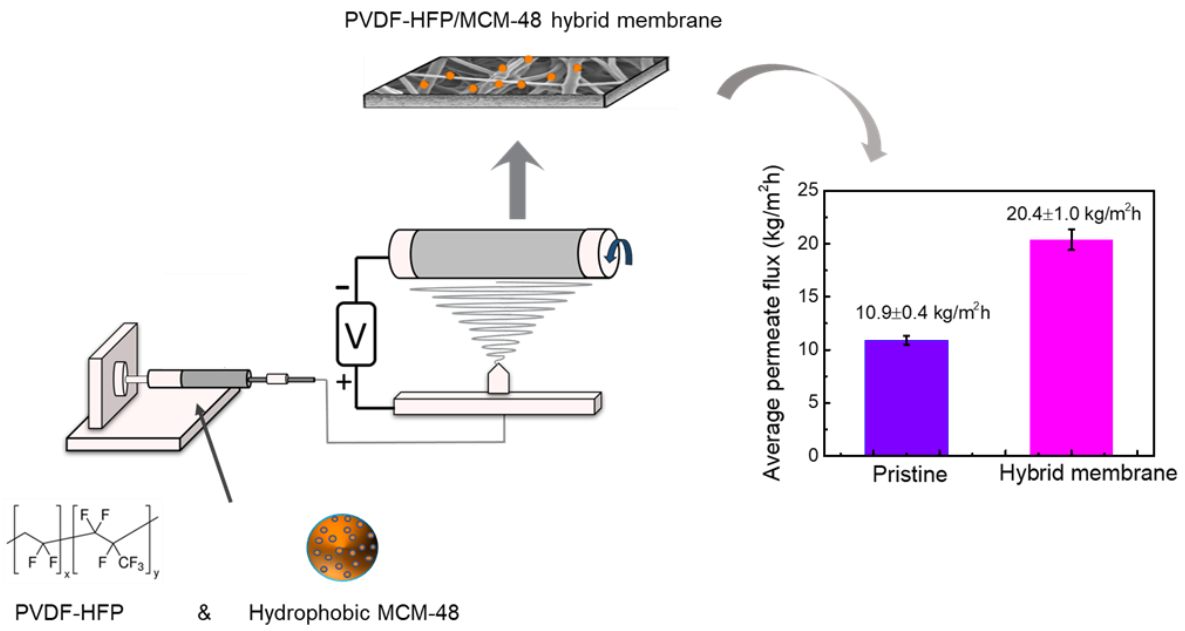


Figure 6. 1 Graphical Abstract

## 6.1 Background

Membrane distillation (MD) has a promising future in treating hypersaline feed solutions such as shale gas produced water<sup>181</sup> and reverse osmosis concentrates<sup>182</sup> to address the issues of water scarcity via a combination of the thermal and membrane processes.<sup>183,184</sup> Compared to other desalination techniques used to treat high salinity brines, MD offers several distinct advantages, including higher rejection, lower operating temperature and pressure, the potential to utilize any form of low-grade waste heat or solar energy as the thermal driving force, and a relatively low sensitivity towards feed salinity.<sup>19,185</sup>

Despite these advantages, MD systems have not been widely applied in industrial or commercial settings. One important reason for this is its relatively low permeability.<sup>186,187</sup> Flux enhancement in MD has been discussed in many works.<sup>188-189</sup> Generally, varying pore diameter or membrane thickness, fabricating composite hydrophobic/hydrophilic membranes, and blending with functional inorganic fillers are common approaches towards flux enhancement.<sup>190,191</sup> Among these methods, blending with inorganic particles has generated a great deal of interest due to the wide availability of different types of functional inorganic particles. The inorganic materials used can be classified into porous (e.g., zeolites, carbon nanotubes, MOFs, and mesoporous silica) and nonporous types (e.g., TiO<sub>2</sub>, Al<sub>2</sub>O<sub>3</sub>, and ZrO<sub>2</sub>).<sup>192,193</sup> Upon incorporation into polymeric materials, nonporous nanoparticles have been demonstrated to optimize membrane structure, enlarge pore size, narrow pore size distribution, and improve membrane porosity to some extent.<sup>194</sup> However, the enhancement of permeate flux is limited by the impermeability of the nonporous particles.<sup>194,195</sup> The internal porosity of porous fillers is assumed to provide additional flow paths for water vapor, which can directly contribute to the enhancement of membrane flux.<sup>196</sup> Moreover, the chains of typical synthetic polymers can penetrate the pores of the mesoporous fillers and enhance polymer-particle interfacial adhesion.<sup>193</sup> Currently, very few studies have focused on the incorporation of porous nanofillers into the polymer matrix to directly enhance membrane transport properties of MD membrane materials. Cheng et al.<sup>197</sup> found that the addition of 1 wt% MOF particles efficiently increased the water flux of the hybrid MOF/PVDF hollow fiber membrane by 50.5% in the MD operation process.

The mesoporous M41S family (MCM-41, MCM-48 and MCM-50) has received significant attention as catalysts, adsorbents, and membranes due to their large specific surface areas, high

pore volume, tunable pore sizes (2-50 nm), and easy surface functionalization.<sup>198,199</sup> Mesoporous silica spheres with good compatibility in polymer matrixes have been widely used to fabricate mixed-matrix nanocomposite gas separation membranes to enhance gas permeability without sacrificing selectivity.<sup>198,200</sup> For example, the MCM-41 incorporated polysulfone composite membrane exhibited a clear enhancement in thermal stability, mechanical performance, and H<sub>2</sub>/CH<sub>4</sub> separation performance.<sup>201</sup> However, to the best of our knowledge, no studies have investigated the utilization of mesoporous silica for the preparation of composite MD membranes with enhanced performance.

PVDF has been widely used in the MD process due to its high mechanical strength, good thermal stability, outstanding chemical resistance, and hydrophobicity;<sup>195</sup> with the co-polymer of PVDF, polyvinylidene fluoride-hexafluoropropylene (PVDF-HFP) exhibiting enhanced hydrophobicity and durability.<sup>202</sup> In this work, MCM-48 of controlled particle sizes were prepared under mild conditions and functionalized with vinyltriethoxysilane (VTEOS).<sup>203</sup> In addition to increasing hydrophobicity, the VTEOS modification promotes adhesion between the inorganic and organic phases and improve the dispersion of silica nanoparticles into the polymer matrix.<sup>204</sup> Compared with two dimensional hexagonal MCM-41, MCM-48 nanoparticles with three dimensional cubic channel networks serve as a porous host for easy and direct access of guest species without pore blockage, offering fewer diffusion limitations.<sup>196</sup> Scanning electron microscope (SEM), transmission electron microscopy (TEM), and nitrogen sorption tests were performed to characterize the morphology, pore structure, and pore size of MCM-48 nanoparticles. Hybrid PVDF-HFP/MCM-48 electrospun nanofibrous membranes were prepared by blending with hydrophobic MCM-48 nanoparticles, and their performance was evaluated in a direct contact membrane distillation (DCMD) configuration. The effects of the addition of MCM-48 on the physical and chemical properties of the hybrid membrane and DCMD performance were investigated. Not only is this the first attempt to fabricate PVDF-HFP/MCM-48 nanofibrous membranes by electrospinning, but also the first to employ MCM-48 based membranes in MD processes.

## 6.2 Materials and methods

### 6.2.1 Chemicals and materials

Triblock copolymer F127, cetyltrimethylammonium bromide (CTAB), PVDF-HFP, VTEOS, DMAc, tetraethyl orthosilicate (TEOS), ethyl alcohol (C<sub>2</sub>H<sub>5</sub>OH), and ammonium hydroxide (NH<sub>4</sub>OH, 28.0~30.0 wt%) were purchased from Sigma-Aldrich (Oakville, ON, Canada). All other agents were purchased from Fisher-Scientific (St Laurent, QC, Canada).

### 6.2.2 Preparation of functionalized MCM-48 nanoparticles

MCM-48 nanoparticles of three different sizes were synthesized by using CTAB as a structure directing agent, TEOS as a silica source, and F127 as a particle dispersion agent under basic conditions—similar to those reported in the literature (**Figure 6.2**).<sup>196</sup>. Briefly, 0.5 g of CTAB and 2.05 g of F127 were dissolved in a mixture of 96.0 mL of deionized water, 34.0 g of ethanol, 10.0 g of ammonium hydroxide solution at room temperature, followed by the immediate addition of TEOS (1.8 g). After 1 min of vigorous stirring at 1000 rpm, the mixture was kept at static conditions for further silica condensation at room temperature. The white solids were collected and washed by centrifugation at 12,000 rpm (ThermoFisher Scientific, Germany), then air dried at 70 °C for 30 h. Surfactants were removed by calcination at 550 °C for 5 h to obtain the final MCM-48 product.

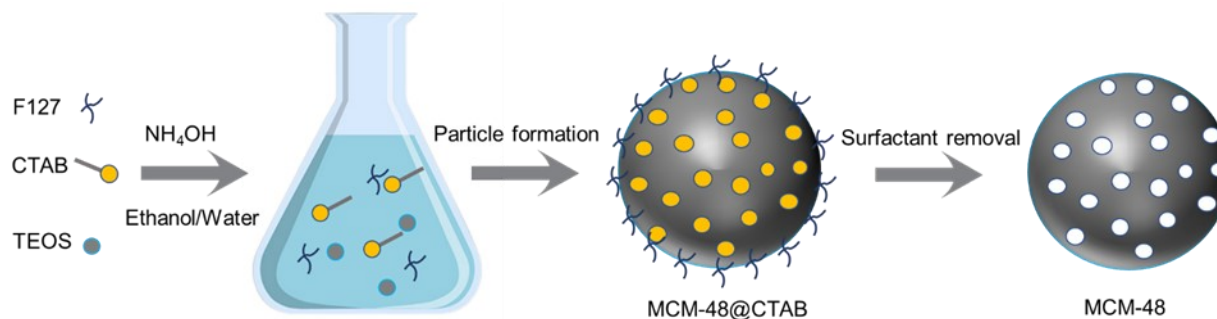


**Figure 6. 2** Schematic representation of synthesis of MCM-48 nanospheres.

The hydrophobic modification process was completed with VTEOS at room temperature as follows:<sup>203</sup> 100 mg of MCM-48 nanoparticles, 1.5 mL of VTEOS, and 10 mL of ethanol were added into a bottle and placed on a magnetic stirrer at 1100 rpm for 24 h at room temperature, producing a clear solution. 1 mL of ammonium hydroxide solution was added to the resultant solution and stirred for 30 h at 30 °C. To separate the vinyl-modified MCM-48 nanoparticles, the resulting solution was centrifuged three times in ethanol and dried in an oven at 50 °C for 24 h.

### **6.2.3 Preparation of pristine PVDF-HFP and hybrid PVDF-HFP/MCM-48 electrospun nanofibrous membranes**

Taking advantage of the accessible functionalization of MCM-48 silica nanoparticles and their excellent compatibility with the organic polymer matrix, the modified MCM-48 spheres were incorporated into the polymer. The electrospun nanofibrous mats were prepared in a similar method as reported in our previous work.<sup>205</sup> In short, the dope solution was prepared by dispersing hydrophobic MCM-48 (0 wt% for pristine membrane and 6.7 wt% for hybrid membrane) and PVDF-HFP (15 wt%) in a mixture of DMAc/acetone (8/12, V/V). The mixture was then stirred overnight on a hot plate at 45 °C, following an ultrasonic treatment for 2 h prior to the electrospinning process. 20 mL of each solution was loaded into a Luer-lock syringe (Vitaneedle, MA). Electrospinning of the dope solutions was conducted using a Nanospinner (NE300, Inovenso, Turkey). Uniform polymeric suspensions were delivered via the metallic nozzle at a 4.0 mL/h flow rate. A high voltage (25 kV) was applied between the nozzle and an electrically grounded metallic drum covered by a piece of aluminum foil with a rotation speed of 100 rpm. The distance between nozzle tip and collector was maintained at 12 cm.

### **6.2.4 Characterization methods**

Nitrogen sorption tests were performed using a BET Sorptometer (BET-201-A, Porous Materials Inc., Ithaca, NY, USA). A multiple-point Brunauer-Emmett-Teller (BET) method was used to calculate the specific surface area of MCM-48 nanoparticles. The average pore size and pore volume of MCM-48 nanoparticles were calculated by analyzing the nitrogen adsorption isotherm using the Barret-Joyner-Halenda (BJH) method. The morphology of the MCM-48 nanoparticles and the surface of the resulting membranes were observed by SEM. Nanoparticle size distribution and frequency were measured via ImageJ software. TEM images (Tecnai G2 F20) of MCM-48

nanoparticles supported on a carbon-coated copper microgrid substrate were taken. The high-angle annual dark field scanning transmission electron microscopy (HAADF-STEM) images, STEM and energy-dispersive X-ray spectroscopy (STEM-EDS) mapping images were recorded by a STEM (Talos F200X G2 S/TEM, Thermo Scientific) at an acceleration voltage of 200 kV. Thermal properties of the membranes were characterized by thermal gravimetric analysis (TGA Q5000 V3.15) under a nitrogen atmosphere at a heating rate of 10 °C/min. The surface roughness of prepared membranes was evaluated by AFM. The average roughness (Ra) values were obtained using the “Gwyddion” software. ATR-FTIR was performed to observe the functional group changes. The crystal structures of particles and membranes were investigated via X-ray diffraction (XRD-model, Bruker D8 Discover instrument in which the X-ray source is copper and is equipped with a Vantec area detector). Water contact angles were measured using the system software. The mean pore size of the as-prepared membranes was characterized by a capillary flow porometer based on the wet/dry flow method. Gas permeability was determined by the steady state porosimeter (APP-10K-A-1, Porous Materials Inc., Ithaca, NY, USA).

### **6.2.5 Direct contact membrane distillation experiments**

We performed DCMD performance experiments using a flat-sheet membrane set-up. The hot feed solution was maintained at a constant temperature using a water bath. The hot feed and cold distillate solutions were moved co-currently across the lower and upper faces of the membrane cell, respectively, with the help of two gear pumps. The circulation feed flow rate and distillate flow rate were detected by two flowmeters and kept constant. The experiments were carried out with NaCl solution (35 g/L) as a feed solution to investigate the flux and salt rejection. Operational temperatures were monitored at the inlet and outlet of the module using four thermocouples connected to a thermometer. The conductivity of the distillate Permeate quality was monitored using a conductivity meter, while the membrane flux,  $J$ , of the prepared membranes was calculated according to the equation (3-1).

## 6.3 Results and discussion

### 6.3.1 Characterization of MCM-48 nanoparticles

The effect of the amount of F127 on the particle morphology and size was investigated using SEM and TEM image analysis. Both SEM (**Figure 6.3 A, D, G**) and TEM (**Figure 6.3 B, E, H**) images demonstrate that the prepared MCM-48 were well-dispersed spherical nanoparticles. With an increase in the amount of F127, the average particle size calculated from SEM micrographs decreased from  $163.7 \pm 30.6$  to  $83.6 \pm 12.6$  nm. The mesoporous structure of MCM-48 was easily observed at high magnification in TEM images, indicating the well-ordered pore networks,<sup>206,207</sup> which is in good agreement with the BET surface area and total pore volume analysis (below). We obtained monodisperse MCM-48 materials without the deformation of structural properties through use of triblock copolymer F127 as a good dispersing agent, and efficiently controlling the particle size in the binary surfactant system.<sup>206</sup> The nonionic surfactant F127 interacts with silicates through hydrogen bonds during the assembly of silicates, which limit the growth of particle grains, resulting in different sizes of MCM-48 spheres.<sup>207</sup> The structural properties of these samples are summarized in **Table 6.1**. The pore size and pore volume changed slightly, and the BET surface area decreased from 1311 to 1082 m<sup>2</sup>/g with the amount of F127 increasing from 2.05 to 5.06 g.

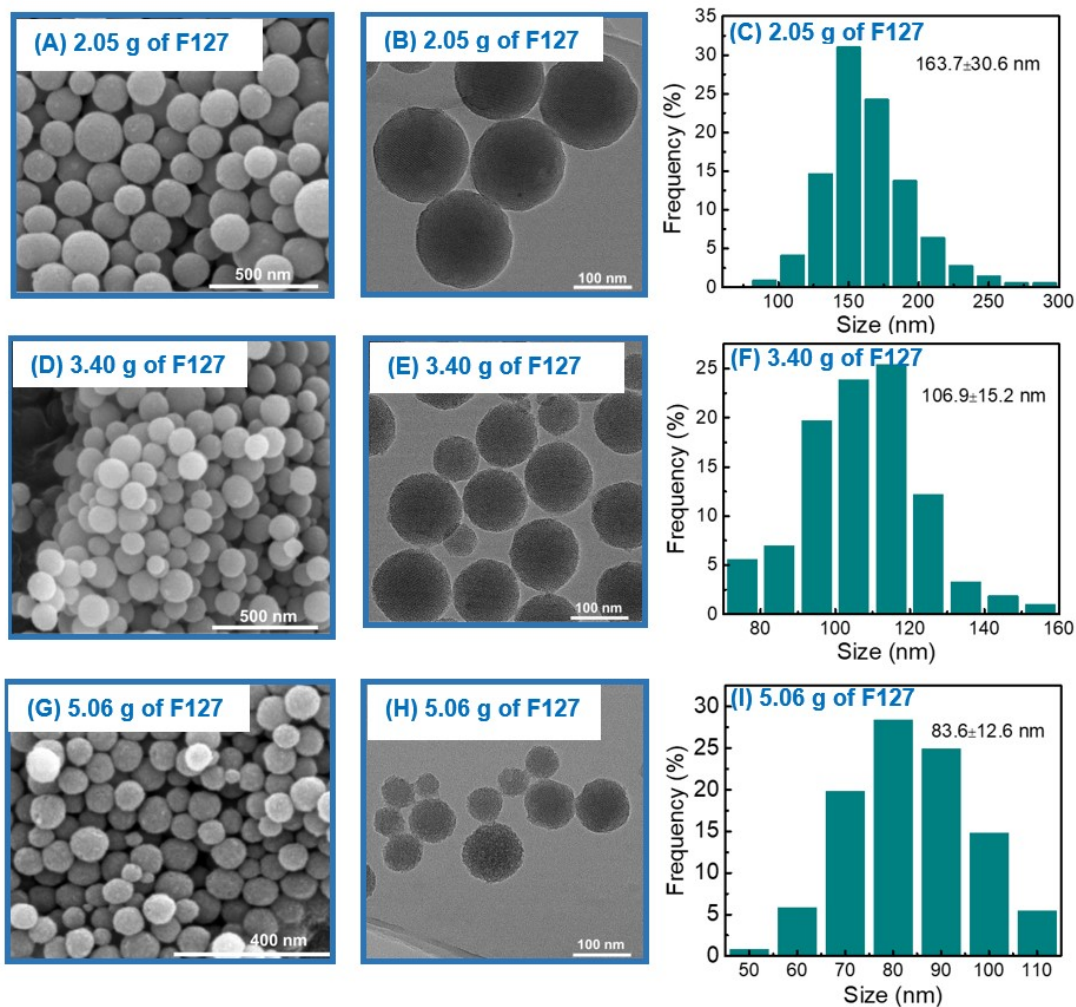


**Figure 6. 3** (A, D, G) SEM images, (B, E, H) TEM images and (C, F, I) particle size distribution of prepared MCM-48 nanoparticles using various amounts of F127 as the particle dispersion agent.

**Table 6. 1** Structural parameters of MCM-48 nanoparticles using different amounts of F127.

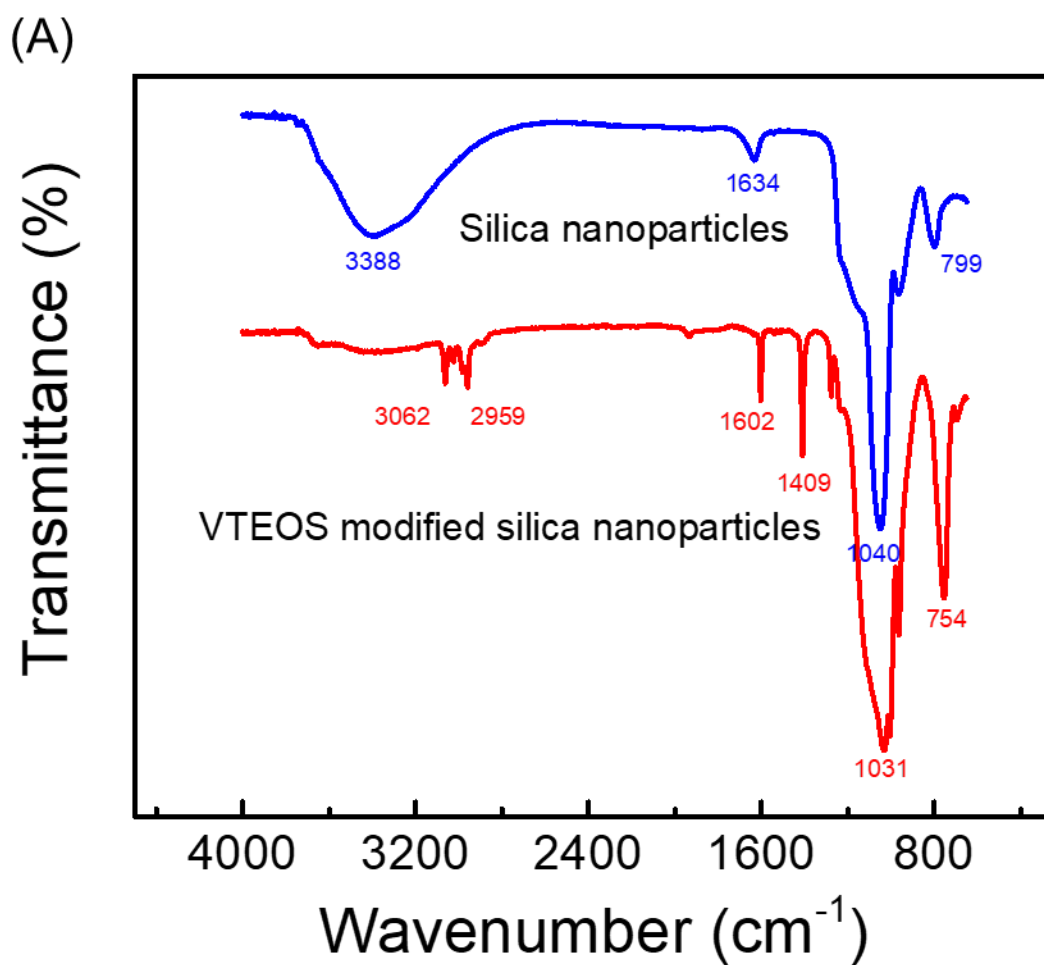
Amount of added F127 (g)	BET surface area (m <sup>2</sup> /g)	Average pore diameter (nm)	Pore volume (cm <sup>3</sup> /g)
2.05	1311	3.1	1.028
3.40	1123	3.2	0.900
5.06	1082	3.5	0.943

To investigate the effects of MCM-48 incorporation on MD membrane properties and performance, only MCM-48 nanoparticles with the largest BET surface area (added F127 = 2.05 g) were applied. This is discussed in the following section. Future work could further investigate the effects of different sizes of MCM-48 spheres on membrane performance in DCMD applications.

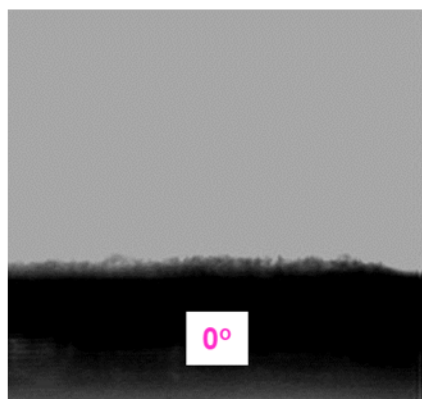
Large scale synthesis of MCM-48 nanoparticles was carried out in a larger batch using 3.5 g of CTAB in 1.06 L of F127/Deionized water/EtOH/NH<sub>4</sub>OH solution. Particle morphologies of the large batch samples were similar to those in the small batch sample that used 0.5 g of CTAB in 150 mL of mixture solution. Thus, the production of monodisperse spherical MCM-48 materials can be easily scaled up without any significant loss of sample quality and quantity due to the kinetically controlled short synthesis time.

It is worth pointing out that hydrophobization of hydrophilic nanofillers will render them miscible with another hydrophobic matrix.<sup>195</sup> Additionally, interfacial interactions can be improved by molecular entanglement between the hydrophobic chains grafted on the modified nanoparticles surface and the polymer matrix.<sup>208</sup> To disperse MCM-48 spheres in the PVDF-HFP matrix efficiently and avoid nanoparticle agglomeration, the hydrophobization of MCM-48 with VTEOS was carried out.<sup>208</sup> The successful graft was confirmed via FT-IR spectral analysis and water contact angle measurements. As shown in **Figure 6.4 A**, the strong broad peaks around 3388 cm<sup>-1</sup> (O-H stretching vibration), 1049 cm<sup>-1</sup> (Si-O-Si stretching), and 799 cm<sup>-1</sup> (Si-O stretching) were

assigned to hydrophilic MCM-48 silica nanoparticles. For vinyl modified MCM-48, new peaks of ethyl at  $3000 - 2700 \text{ cm}^{-1}$  (stretching, C-H) and  $1409 \text{ cm}^{-1}$  (bending, C-H) provided evidence for surface VTEOS functionality on MCM-48. Additionally, the peak located at  $1602 \text{ cm}^{-1}$  was due to asymmetric vibrations of H-O-H which is overlapped with vinyl  $\nu(\text{C}=\text{C})$  vibrations.<sup>209,210</sup> The contact angle results of the nanoparticles are shown in **Figure 6.4 B-C**. As observed, the contact angle of nanoparticles dramatically increased from  $0^\circ$  in the hydrophilic MCM-48 to  $150.5^\circ \pm 1.2^\circ$  after VTEOS modification.



(B)



(C)

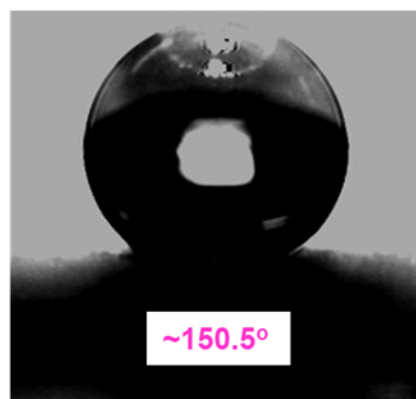


**Figure 6. 4** (A) FTIR spectroscopy for the bare and modified nanoparticles. The contact angle image of the silica nanoparticle (B) before and (C) after modification.

### 6.3.2 Characterization of hybrid membranes

The microstructure and fiber diameter distribution of pristine and hybrid membranes were investigated by FE-SEM analysis (results are presented in **Figure 6.5** and **Figure 6.6**). Both membranes exhibited a 3D interconnected nanofibrous structure. However, the incorporation of hydrophobic MCM-48 into the dope solution changed the morphology of the electrospun membranes. While pristine PVDF-HFP mats have a nearly homogeneous fiber diameter distribution at an average of  $241.3 \pm 55.89$  nm without any beads in their structure, the incorporation of the vinyl modified MCM-48 in the dope solution increased the distribution of the fiber diameter, with a mean value of  $308.12 \pm 3.37$  nm (**Figure 6.6**). Hydrophobic MCM-48 nanoparticles were found randomly distributed on the fibers of the PVDF-HFP/MCM-48 hybrid membranes, with no obvious agglomeration of particles, and do not block the material's pores. The formation of larger fibers can be attributed to the increase of polymer dope viscosity as a result of the presence of hydrophobic MCM-48 nanoparticles.<sup>211</sup> AFM measurements were conducted to observe the topography of the prepared electrospun membranes. As shown in **Figure 6.5 A-B** (inset), the PVDF-HFP/MCM-48 hybrid membranes displayed a high average surface roughness (Ra) of  $336.3 \pm 70.7$  nm. While the average surface roughness of pristine PVDF-HFP membranes was  $273.0 \pm 44.1$  nm; the sharp increase in roughness of the hybrid membrane may be associated with the incorporation of MCM-48 nanoparticles, which created protrusions and led to a highly textured surface.<sup>212</sup>

To further verify the existence of MCM-48 in the composite membranes and detailed composition of the as-prepared PVDF-HFP/MCM-48 hybrid membranes, high-magnification TEM, HAADF-STEM and STEM-EDS mapping images are shown in Figure 2E-N. The HAADF-STEM images (**Figure 6.5 F-I**) of individual nanofiber confirm the well-distributed MCM-48 nanoparticles loaded onto/into the nanofibers either in a mono-dispersed or aggregated form, leading to the formation of micro/nano scale roughness. Associated STEM-EDS mapping images (**Figure 6.5 J-N**) reveal C, O, F, and Si elements, indicating the successful incorporation MCM-48 nanoparticles in the PVDF-HFP backbone.

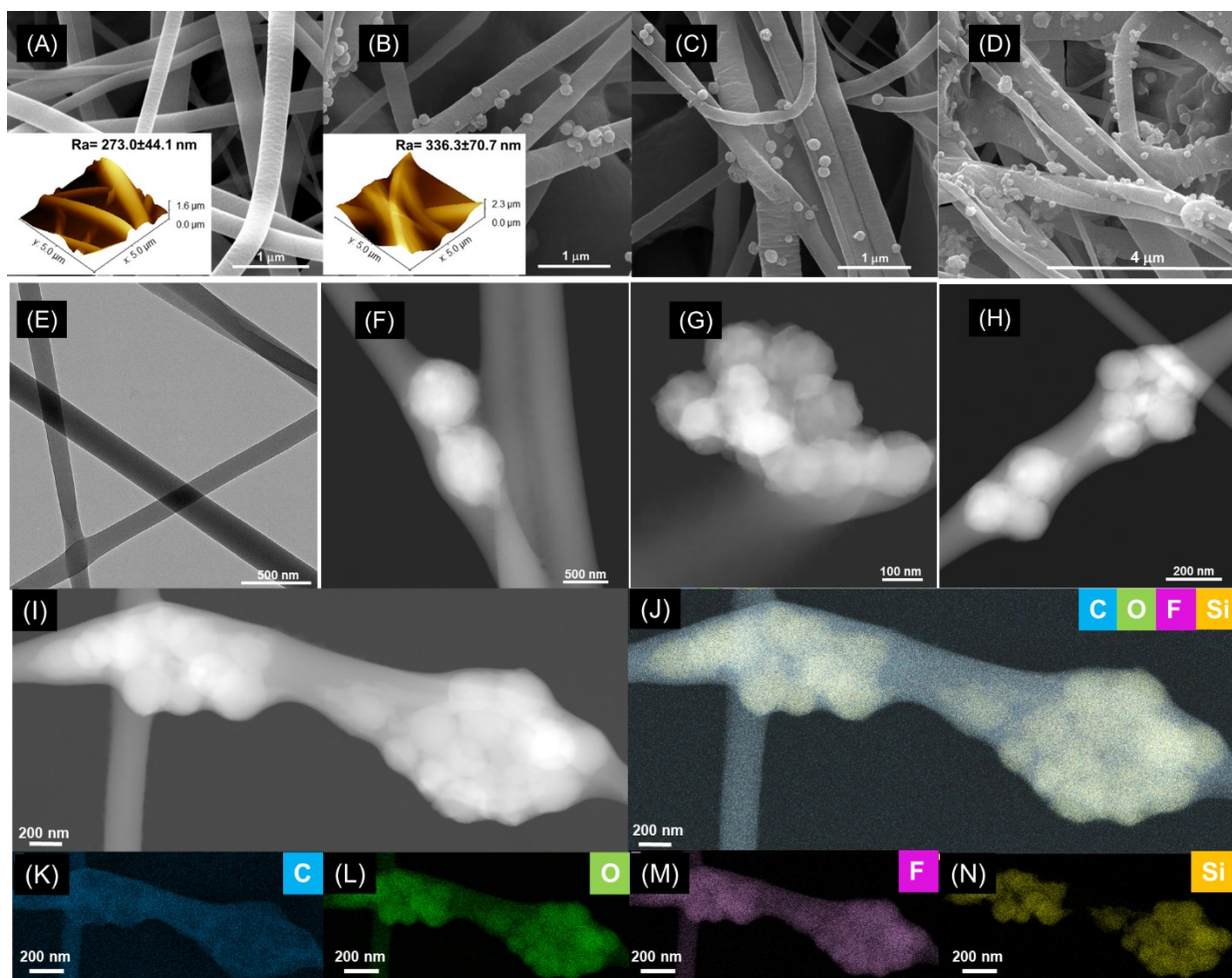


**Figure 6. 5** The detailed microstructure of the fabricated membranes. (A, B, C, D) Surface morphology of the fabricated membranes visualized by SEM and probed by AFM (inset). (E) High-magnification TEM image of pristine PVDF-HFP membrane. (F, G, H, I) HAADF-STEM images of PVDF-HFP/MCM-48 hybrid membrane with the corresponding STEM-EDS mapping analysis (J, L, K, M, N).

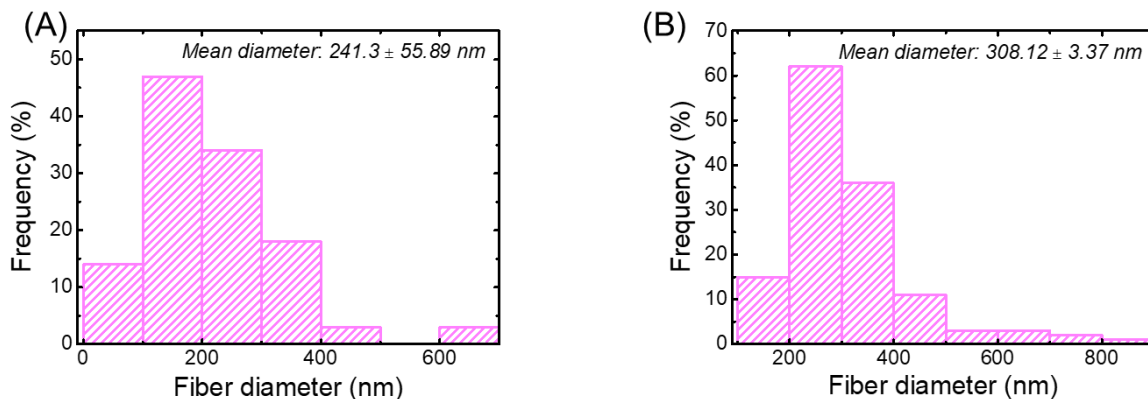


**Figure 6. 6** Fiber diameter distribution of the electrospun nanofibrous membranes (A) Pristine and (B) Hybrid membrane.

Thermogravimetric analyses are shown for bare, vinyl-MCM-48 and electrospun membranes in **Figure 6.7**. The bare MCM-48 sample underwent a slight weight loss which was attributed to the evaporation of the absorbed water molecules or trapped solvents occurred below 200 °C and silanol group dehydroxylation at higher temperatures.<sup>209</sup> Compared to the unmodified MCM-48, vinyl modified particles showed no obvious weight loss until 465°C, which was related to the decomposition of organic groups from the modifier. These results suggest that the synthesized silica nanospheres show good thermal stability at higher temperatures.

As for the neat PVDF-HFP membrane and the hybrid membrane, the major weight loss took place from ~425 °C to 500 °C (**Figure 6.7**), which was due to the decomposition of the PVDF-HFP matrix.<sup>213</sup> However, the hybrid membrane displayed a less weight loss (48%) than the neat membrane sample (75%) within the above discussed temperature range. The difference in the weight loss represents the successful incorporation of vinyl modified MCM-48 nanospheres in the polymer matrix, which maintains the thermal stability of the composite membrane at the region of high temperatures. This implies the addition of MCM-48 improve the thermal stability of the polymer membrane. It is believed that the strong interaction of polymer chain with the hydrophobic MCM-48 nanoparticles, restricting the thermal motions of the polymer chains.<sup>214</sup>

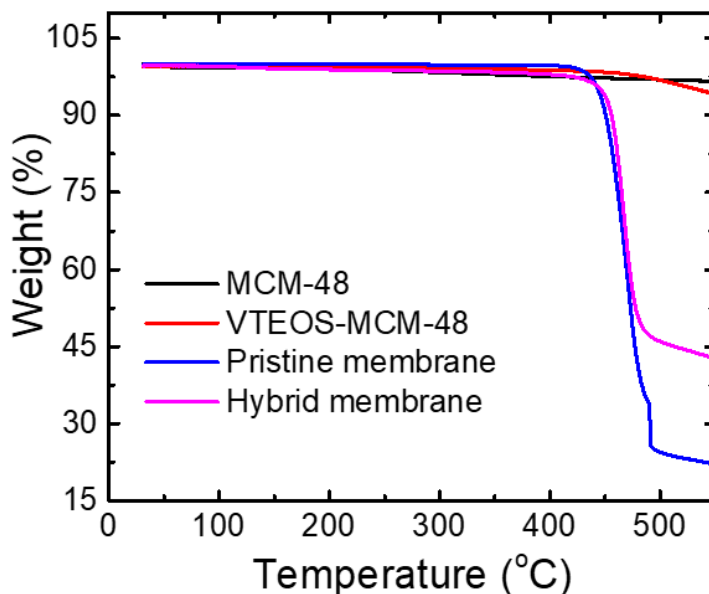


**Figure 6. 7** TGA profile for prepared nanomaterials and membranes

Surface chemical compositions of pristine and composite membranes were characterized with FT-IR spectral analysis was employed to confirm the surface chemical compositions of pristine and composite membranes (**Figure 6.8**). A new strong broad band around  $1051\text{ cm}^{-1}$  was observed in the MCM-48 incorporated membrane, corresponding to the Si-O-Si anti-symmetric stretching vibration peak and C-F stretching vibration peak coefficient.<sup>215</sup> In addition, the new absorption peak found at  $1602\text{ cm}^{-1}$  attributable to the C=C vibration, was shown in PVDF-HFP/MCM-48 hybrid membranes. Meanwhile, the peaks appearing within the  $2900\text{-}3000\text{ cm}^{-1}$  range were attributed to C-CH<sub>3</sub> asymmetric deformation vibration and asymmetric vibration of CH<sub>3</sub>CH<sub>2</sub> in VTEOS modified MCM-48 spheres.<sup>195</sup> Thus, the FT-IR information fully confirmed the successful incorporation of hydrophobic MCM-48 spheres in the PVDF-HFP matrix.

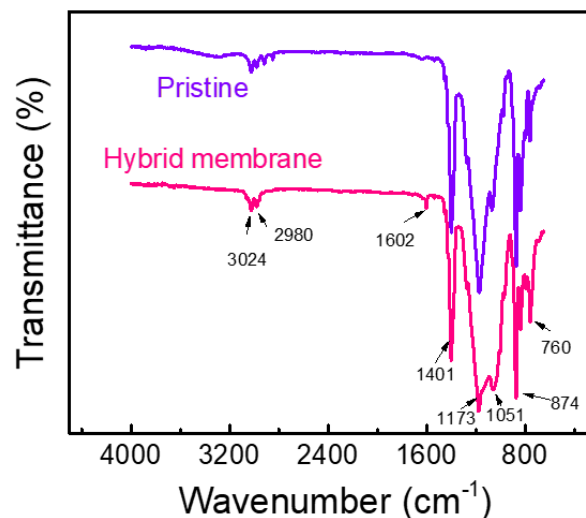


**Figure 6. 8** FTIR spectroscopy for pristine and hybrid membranes.

The small-angle XRD data revealed four characteristic peaks at  $2\theta$  of  $2.56^\circ$ ,  $2.98^\circ$ ,  $4.76^\circ$  and  $4.98^\circ$  representing the (211), (220), (420) and (332) planes, respectively (**Figure 6.9 A**). This diffraction pattern identifies the 3D Ia3d cubic space group of MCM-48-type mesoporous silica.<sup>196</sup> The obtained pattern of VTEOS modified MCMC-48 still showed the identification pattern of mesoporous silica but with an obvious reduction in the intensities of the peaks at (211) and (220). Meanwhile, peaks at other incidence angles were not observed. Possible reason for this is the modification of vinyl groups inside the pore channels causing feeble block and collapse of pore structure.<sup>216</sup>

**Figure 6.9 B** shows the XRD patterns of as-prepared membranes within a wide range, two major peaks at  $18.28^\circ$  (100) and  $20.08^\circ$  (020) indexed to the a-crystalline phases of PVDF-HFP.<sup>217</sup> This confirms the partial crystallization of PVDF units in the copolymer and gives a semicrystalline structure of PVDF-HFP. When the silica particles were impregnated into the membrane, the intensity of these peaks decreased dramatically. This may result from the addition of inorganic nanofillers enhancing amorphous region in PVDF-HFP nanofibers.<sup>218</sup> Within the low angle range from  $0^\circ$  to  $10^\circ$  (**Figure 6.9 B** inset), the specific diffraction peaks at (211) (200) characteristic of the cubic mesophase in VTEOS modified MCM-48 were observed in the XRD curve of hybrid

membrane due to the successful incorporation of hydrophobic MCM-48 nanospheres into the PVDF-HFP matrix.

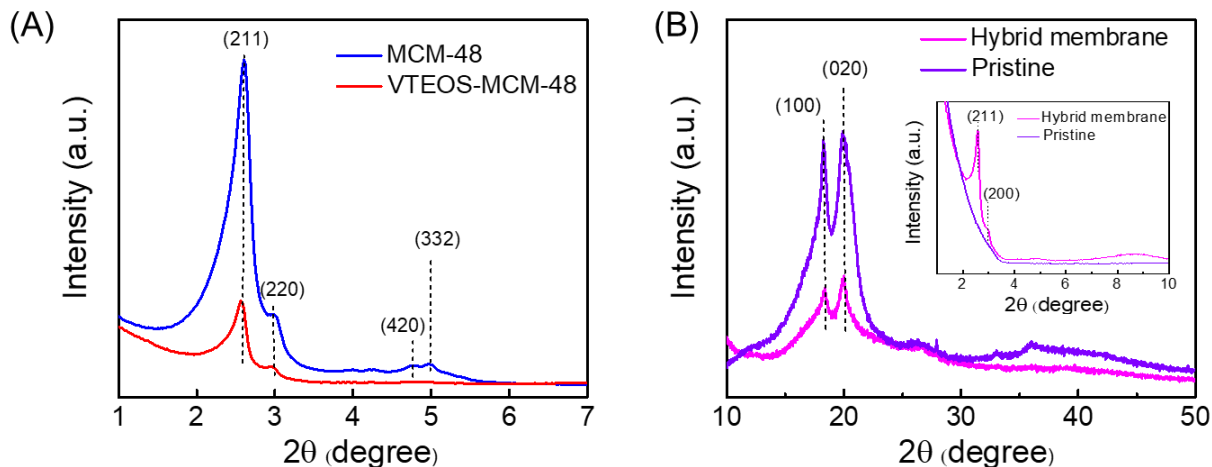


**Figure 6. 9** (A) Small-angle XRD patterns of synthesized nanoparticles, and (B) the wide-angle XRD patterns of different membranes. Inset image shows the small-angle XRD patterns of the respective samples.

The average water contact angle (WCA) for the prepared membranes is shown in **Figure 6.10**. It was observed that the addition of MCM-48 spheres promoted membrane hydrophobicity, with WCA increasing from  $126.9^{\circ} \pm 3.0^{\circ}$  to  $142.3^{\circ} \pm 4.9^{\circ}$  resulting from the surface geometry effect.<sup>215</sup> After the incorporation of MCM-48 nanoparticles, the nascent PVDF-HFP nanofibers, which already had a relatively high WCA, were partly coated by hydrophobic MCM-48 and the electrospun fibers exhibited a surface morphology with micro/nano bumps. It is possible that the micro/nanostructure evident in the hybrid membrane introduce hierarchical roughness and rendered the membrane surface more hydrophobic.<sup>219</sup>

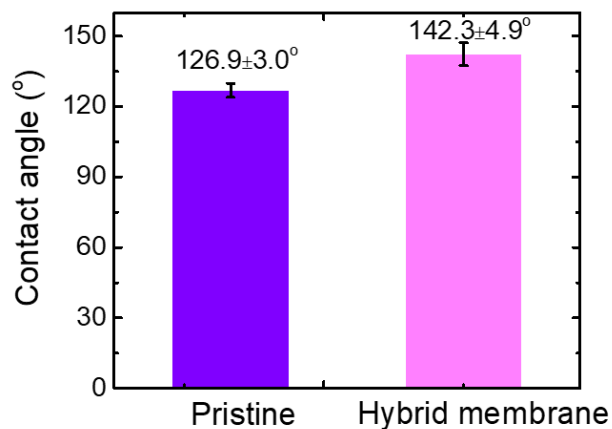


**Figure 6. 10** Water contact angle of the pristine and hybrid membranes.

### 6.3.3 Enhancement of gas permeability and DCMD performance of hybrid membranes

In a DCMD process, the water vapor molecules transmit through the porous membrane matrix at various vapor pressure gradients, which is very similar to a gas diffusing across the porous media. Thus, the breathability of a membrane obtained from the gas permeability test is important to predict the MD vapor flux.<sup>194</sup> The air permeation flux observed at different pressures for the PVDF-HFP membranes and the hybrid membranes are shown in **Figure 6.11 A**. The results of air flow rate showed the expected trend for all membranes, positively correlated with the applied pressure. Compared to the unmodified membrane, the gas permeation flux of the MCM-48 incorporated membranes improved significantly, which was consistent with an increase in mean pore size. After the incorporation of hydrophobic MCM-48 nanoparticles, the hybrid membrane showed a mean pore size of  $0.79 \pm 0.16 \mu\text{m}$ , as compared to a mean pore size of only  $0.31 \pm 0.14 \mu\text{m}$  for the pristine membrane (**Figure 6.11 B**).

The remarkable gas flow of the composite membrane should be highlighted here. For example, its value at 40 psi was found to be 969.8 cc/sec compared to the 166.6 cc/sec for the pristine membrane, while that of a commercial PVDF membrane from the reference was observed to be 88.6 cc/sec.<sup>106</sup>

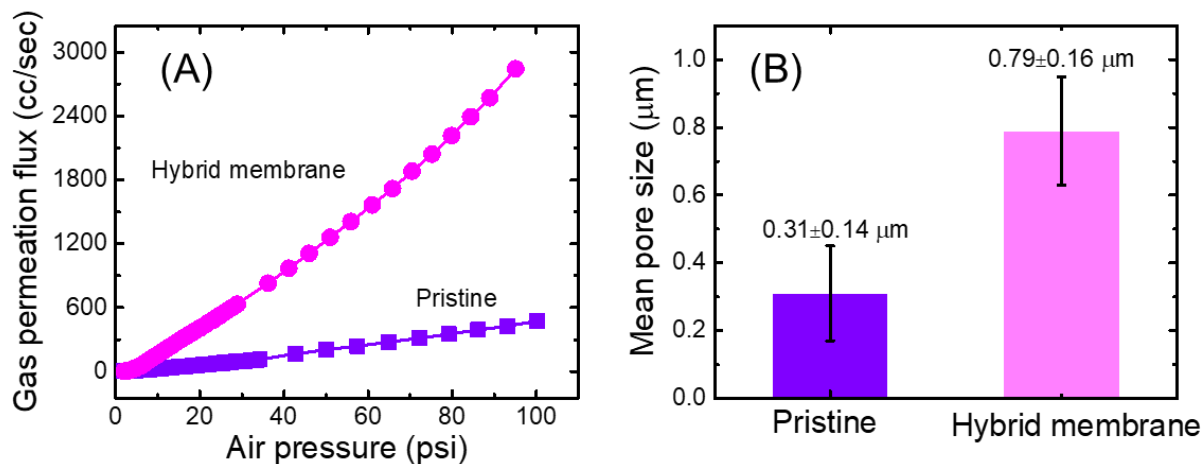


**Figure 6. 11** (A) Gas permeability of electrospun membranes at different applied pressures and (B) mean pore size of the pristine and hybrid membranes.

The influence of the addition of MCM-48 on DCMD performance was investigated using 35g/L NaCl as the feed solution for 4 h at the temperature difference of 40 °C. Both the pure PVDF-HFP membrane and the hybrid membrane were tested, and the results are presented in **Figure 6.12**. The membrane distillation flux increased considerably for the blend membrane, and the average flux enhancement percent (%) was as high as 87.16. This surprising enhancement in flux is much higher than that previous reported in the research (**Table 6.2**).<sup>130,194,219,220</sup> In order to illustrate the importance of the inner pore structure on the MD performance, the nonporous silica nanoparticles, including the templates (referred to as MCM-48@CTAB), were also added to the PVDF-HFP matrix, the resultant composite membrane was used as the control here. However, the flux for the control membrane decreased slightly as compared with the pristine membrane (**Table 6.2**). All these results indicate that the addition of porous MCM-48 into the PVDF-HFP matrix can increase the mass transport in the DCMD process.

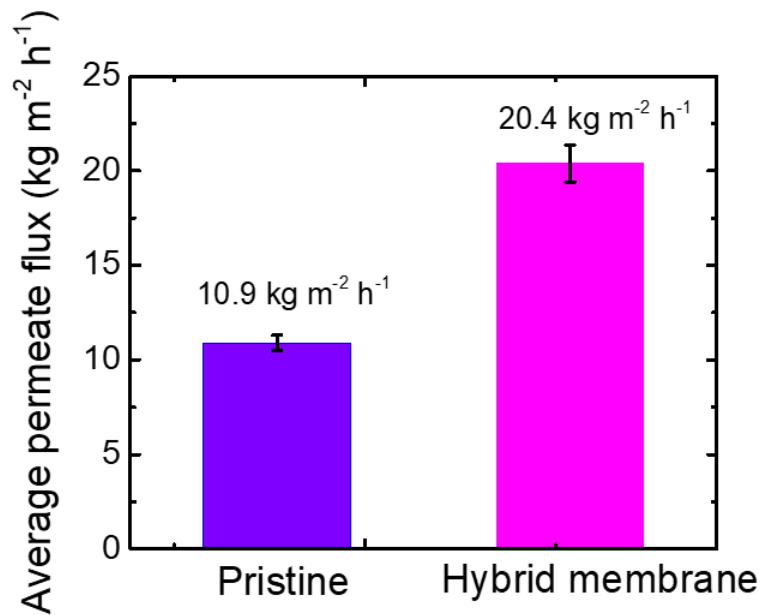


**Figure 6. 12** water flux of pristine and hybrid membranes in DCMD process. A 35g/L NaCl solution was used as feed solution maintained at 55 °C and deionized water was used as a permeate cooling solution maintained at 15 °C. The flow rate of feed and permeate streams were both 0.7 LPM.

**Table 6. 2** Comparisons of flux enhancement between the current work and reference studies.

Membrane	Configuration	Feed	Feed temperature (°C)	Flux enhancement (%)
PVDF/Clay <sup>194</sup>	DCMD	3.5 wt% NaCl	80	7.5
PVDF/AC <sup>219</sup>	VMD	10 wt% NaCl	70	30
PVDF-HFP/SiO <sub>2</sub> <sup>130</sup>	DCMD	3.5 wt% NaCl	80	16.8
PVDF/MOF <sup>220</sup>	DCMD	3.5 wt% NaCl	48	78.14
PVDF-HFP/MCM-48 (This work)	DCMD	3.5 wt% NaCl	55	87.16
PVDF-HFP/MCM-48@CTAB (This work, nonporous control)	DCMD	3.5 wt% NaCl	55	-2

### 6.3.4 Proposed mechanism of water vapor permeation through the hybrid membrane

In the PVDF-HFP/MCM-48 hybrid membranes, the porous MCM-48 nanoparticles can be found in two forms demonstrated by the SEM and HAADF-STEM images: fully/partly entrapped inside the polymer fibers and exposed outside the fibers, both can assist in the water vapor transport during the DCMD operation. On one hand, the addition of MCM-48 nanoparticles would enlarge the fiber diameter, contributing to the increased pore size of hybrid membranes.<sup>221</sup> On the other hand, the porous MCM-48 nanospheres with large pore volume exist outside the fibers may serve as sorbent sites that allow the water vapor molecules hop from one site to another by interacting with the surfaces.<sup>222</sup> Furthermore, the incorporated MCM-48 nanospheres either in monodispersed or aggregated form can increase membrane surface roughness with micro/nano protrusions, thus providing more effective liquid areas to evaporate. As a result, the overall membrane permeability improved greatly after incorporation with the hydrophobic MCM-48 nanoparticles.

### 6.3.5 Long-term stability of the PVDF-HFP/MCM-48 hybrid membrane

Finally, DCMD was carried out continuously treating a 35 g/L NaCl feed solution for 50 h and a mixture of 35 g/L NaCl plus 1.26 g/L CaCl<sub>2</sub> for 24 h to examine the long-term stability of the hybrid membrane. Results showed that the water vapor flux did not decline (**Figure 6.13 A-B**). At the same time, the permeate conductivity stabilized below 8.0 μS/cm during the operation. These results imply the use of MCM-48 nanoparticles may be of great potential to develop composite membranes with high performance for membrane distillation applications.

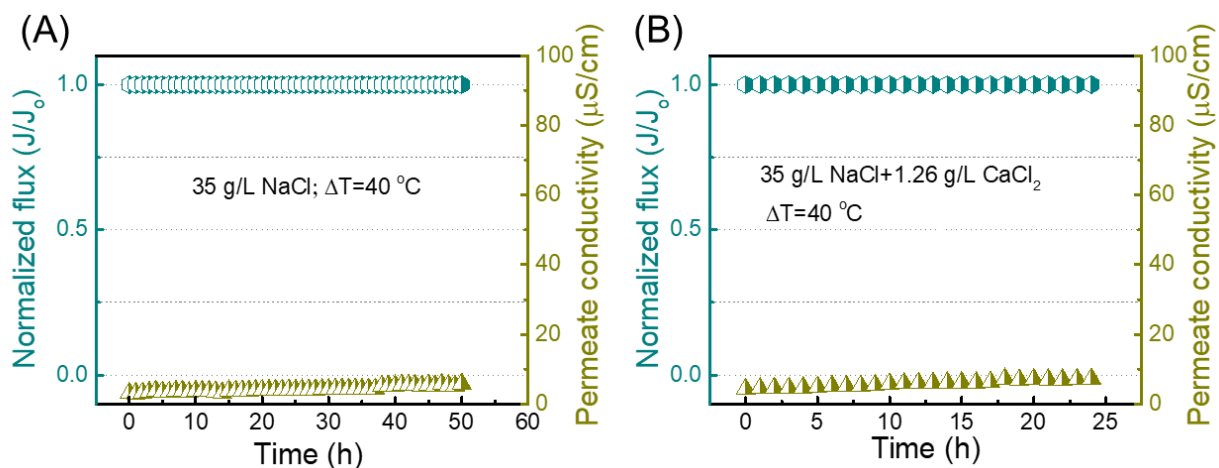


**Figure 6. 13** Long-term stability of PVDF-HFP/MCM-48 hybrid membranes using (A) a 35 g/L NaCl solution and (B) a mixture of 35 g/L NaCl + 1.26 g/L CaCl<sub>2</sub> with the feed solution maintained at 55 °C and deionized water as the cooling solution maintained at 15 °C. The flow rate of feed and permeate streams were both 0.7 LPM.

### 6.4 Summary

In this work, mesoporous MCM-48 silica nanoparticles with controlled particle sizes were synthesized under mild conditions. The hydrophobilized MCM-48 spheres were then incorporated into the PVDF-HFP polymer matrix to produce an inorganic/organic hybrid membrane via the electrospinning process. SEM, HAADF-STEM analyses, FTIR and TGA confirmed the presence of nanoparticles within the membrane matrix. The contact angle, fiber diameter and air permeability of the hybrid membrane increased dramatically. The improved permeability of the PVDF-HFP/MCM-48 hybrid membrane was demonstrated by testing it in DCMD, where the average flux enhancement percent (%) was as high as 87.16 compared to its pristine counterpart.

Finally, the hybrid membrane exhibited stable flux with good permeate quality in the long-term experiments when treating the mixture of NaCl and CaCl<sub>2</sub> solutions. All the results demonstrate that the addition of hydrophobic MCM-48 spheres in the polymer matrix is effective in enhancing membrane permeability. This work suggests that the porous MCM-48 silica may be of great potential in the development of highly permeable membranes for MD applications.

## Chapter 7 Conclusions, contributions and future work

### 7.1 Conclusions

Membrane distillation (MD) is a promising, thermally driven, membrane-based technology as an effective and efficient separation approach to produce fresh water. The existing MD membranes are mostly based on MF membranes which suffer from low vapor flux, pore wetting, and a gradual deterioration of the membrane performance due to membrane fouling in long-term operation. To overcome those limitations, it is essential to achieve a balance in pore size, hydrophobicity, mechanical integrity, as well as the membrane thickness, material selection, and fabrication techniques. The main objective of this research is to design and fabricate practically applicable, high flux, and durable fouling and wetting resistant membranes.

In this research, three types of novel membranes are developed and assessed in MD for various applications. The performance improvement of MD membranes based on this study could reduce the time and cost consumption related to the membrane preparation, increasing the membrane lifespan and material varieties. This provides necessary groundwork to open the gate for next-generation membranes in desalination, wastewater disposal, and food processing process. The following conclusions and contributions can be drawn from experiments performed and the findings throughout the project.

(1) Electrospinning is a fascinating membrane preparation method which can fabricate nanofibers with unique characteristics, such as high porosity, excellent hydrophobicity, very good interconnectivity, and high specific surface area. Various functional materials can be incorporated into the nanofibrous mats during or after their spinning thus tailoring multi-functionality on/into the fibers. Different electrospinning parameters should be optimized to reach a balance in hydrophobicity, thickness, fiber diameter, pore size and mechanical integrity. Superamphiphobic membranes with self-cleaning property could be achieved by effective surface modification on the nanofibrous substrates. The potential applications of nanofibrous composite membranes in water treatment via DCMD have been demonstrated comprehensively in this study.

(2) A highly hydrophobic electrospun PVDF-HFP/(rGO) membrane for use in direct contact membrane distillation (DCMD) has been designed and fabricated successfully via the electrospinning process. The highlights of this work include: (i) The PVDF-HFP-rGO membrane

exhibited a higher liquid entry pressure (LEP<sub>w</sub>) value (103.42 kPa) than that of the PVDF-HFP membrane (34.4 kPa); (ii) The membrane hydrophobicity was improved by introducing rGO into the PVDF-HFP polymer matrix (i.e., the water contact angle was increased from 123° to 139°); and (iii) The PVDF-HFP/rGO membrane exhibited greater stability in the long-term testing with 60 g/L NaCl feed solution. This facile fabrication of highly hydrophobic membrane enriches the knowledge about the application of graphene-based materials in MD membrane with enhanced performance.

(3) The surface modification of PH-rGO nanofibrous substrate with fluoroalkylsilane POTS into a superamphiphobic membrane was realized by a simple dip-coating method. The resultant membrane (PH-rGO-POTS) displayed superhydrophobicity with water contact angles larger than 150° and sliding angles lower than 2°, indicating their self-cleaning properties. Moreover, this as-prepared membrane exhibited large diiodomethane contact angles of 145.3°. The superamphiphobicity property primarily relies on i) reentrant structure formed by the PVDF-HFP/rGO nanofibrous substrate, and ii) low surface energy rendered by the POTS coating. POTS is a perfluorinated agent, a thin layer of POTS coating could decrease the surface energy and reduce the adhesive force of the membranes, leading to the slippery characteristics. The modified membrane also exhibited excellent superamphiphobic stability in harsh treatment conditions (i.e., 4 h boiling in deionized water, 110 h etching in HCl and NaOH solutions, and sonication for 1 h). The superamphiphobic surface demonstrated the outstanding anti-wetting and anti-fouling properties in the presence of various contaminants during the DCMD process. According to the observation, the one-step tailoring of robust superamphiphobicity in this work without sacrificing the water flux, no involvement of membrane surface activation and special equipment would provide new insights for MD application in various wastewater treatments.

(4) Spherical MCM-48 mesoporous nanoparticles of three different sizes were synthesized by varying the amount of dispersing agent F127 and modified with VTEOS to render hydrophobicity. The hydrophobilized MCM-48 spheres were then incorporated into the PVDF-HFP polymer matrix to produce an inorganic/organic hybrid membrane via the electrospinning process. The addition of MCM-48 contributed to the increase of nanofiber diameter, surface roughness, pore size, water CA and air permeability of the hybrid membrane. The PVDF-HFP/MCM-48 hybrid membrane exhibited a flux enhancement of 87.16 % compared to its pristine counterpart in the DCMD process. In the long-term test using 35 g/L NaCl and 1.26 g/L CaCl<sub>2</sub> as the feed, the hybrid

membrane exhibited stable flux with satisfactory permeate quality. It is worth noting that, not only is this the first attempt to fabricate PVDF-HFP/MCM-48 nanofibrous membranes by electrospinning, but also the first to employ MCM-48 based membranes in MD processes. Overall, this work provides an insight into the development of highly permeable membranes for MD applications by employing porous MCM-48 silica as the nanofiller.

## **7.2 Contributions**

In this study, two novel, highly hydrophobic composite membranes were synthesized, characterized and evaluated for their performance in DCMD: the electrospun PVDF-HFP/rGO membrane and PVDF-HFP/MCM-48 hybrid membrane. Furthermore, the robust superamphiphobic modification on electrospun nanofibrous mat to realize the necessary chemical and physical properties for anti-wetting performance was achieved: PH-rGO-POTS membrane with POTS coated on the PVDF-HFP/rGO nanofibrous substrate. Electrospinning is a versatile membrane preparation method which can fabricate nanofibrous mats with unique characteristics. The potential applications of nanofibrous composite membranes in water treatment via DCMD have been demonstrated comprehensively in this study. rGO incorporated membranes exhibited enhanced stability and durability with satisfactory distillate quality compared with the control membranes. The advantage of electrospun nanofibrous mats was then taken of their intrinsic reentrant geometry, and the oxygen-containing functional groups on the rGO nanosheets which facilitate further superamphiphobic modification on the membrane surface. The porous MCM-48 nanoparticles were developed as the nanofiller for the first time to fabricate inorganic/organic hybrid membranes through the electrospinning technique. The addition of MCM-48 spheres was confirmed to improve the water vapor transport during the DCMD operation with a flux enhancement of 87.16 % compared to the pristine membrane.

From this work, four journal articles are expected with two already having been published and one is ready to submit.

## **7.3 Future work**

(1) Hydrophobic membranes, or even superamphiphobic membranes used in MD are easily fouled by oils due to the long range hydrophobic-hydrophobic interactions, which hinders the application

of MD in the treatment of oily wastewater. The Janus membrane formed by constructing a thin hydrophilic layer on a porous hydrophobic substrate can be worth investigating in the future research. The procedure for fabricating the hydrophilic/hydrophobic composite membrane is included in the appendix of this thesis (**Figure A-5**).

(2) Fluorinated silica nanoparticles could be an environmentally friendly and cost-effective replacement for the long chain fluoroalkylsilane POTS to achieve superamphiphobicity on the nanofibrous substrate. The interconnected nanofiber structure provides relatively rough surface that gives the primary reentrant structure. When fluorinated silica nanoparticles further deposited onto the substrate, a second level re-entrant structure is created on the cylindrical nanofibers. The multi-level re-entrant together with the low surface energy from the attached fluorine chains would result in the enhanced anti-wetting property by making the membrane superamphiphobic. Some preliminary results are shown in the appendix (**Figure A-6, A-7, A-8, A-9**).

(3) The particle size of MCM-48 mesoporous spheres can be precisely tuned by varying the amount of dispersing agent F127. In Chapter 5, only one size of MCM-48 is investigated for MD application. Future research efforts can be directed to the evaluation of the effect of MCM-48 size toward the membrane properties and separation performance. Some preliminary results have been obtained (**Figure A-10, A-11, A-12, A-13**). In addition, macroporous fillers (average pore diameter  $d > 50$  nm) could be developed for the highly permeable MD membranes.

(4) Compared to the pressure-driven processes, fouling in MD is not yet fully understood, especially the fouling behavior and mechanism when different kinds of foulants existed simultaneously. Fouling always leads to membrane pore wetting and blocking, restricting the industrial implementation of MD process. This complex phenomenon needs to be deeply studied in future work.

## References

1. Jackson, R. B.; Carpenter, S. R.; Dahm, C. N.; McKnight, D. M.; Naiman, R. J.; Postel, S. L.; Running, S. W., Water in a changing world. *Ecol. Appl.* **2001**, *11*, 1027-1045.
2. Chen, L.; Wang, H.; Kuravi, S.; Kota, K.; Park, Y. H.; Xu, P., Low-cost and reusable carbon black based solar evaporator for effective water desalination. *Desalination* **2020**, *483*, 114412.
3. Xu, X.; He, Q.; Ma, G.; Wang, H.; Nirmalakhandan, N.; Xu, P., Selective separation of mono- and di-valent cations in electrodialysis during brackish water desalination: Bench and pilot-scale studies. *Desalination* **2018**, *428*, 146-160.
4. Saavedra, A., Valdés, H., Mahn, A., & Acosta, O., Comparative Analysis of Conventional and Emerging Technologies for Seawater Desalination: Northern Chile as A Case Study. *Membranes* **2021**, *11*, 180.
5. Winter, T.; Pannell, J.; McCann, L., The Economics of Desalination and Its Potential Application in Australia. *University of Western Australia* **2005**, No. 413-2016-25978.
6. Esmailion, F., Hybrid renewable energy systems for desalination. *Appl. Water Sci.* **2020**, *10*, 1-47.
7. Zarzo, D.; Prats, D., Desalination and energy consumption. What can we expect in the near future? *Desalination* **2018**, *427*, 1-9.
8. Elimelech, M.; Phillip, W. A., The future of seawater desalination: energy, technology, and the environment. *Sci.* **2011**, *333*, 712-717.
9. Chen, G.; Yang, X.; Lu, Y.; Wang, R.; Fane, A. G., Heat transfer intensification and scaling mitigation in bubbling-enhanced membrane distillation for brine concentration. *J. Membr. Sci.* **2014**, *470*, 60-69.
10. Boo, C.; Lee, J.; Elimelech, M., Omniphobic polyvinylidene fluoride (PVDF) membrane for desalination of shale gas produced water by membrane distillation. *Environ. Sci. Technol.* **2016**, *50*, 12275-12282.

11. Schwantes, R.; Cipollina, A.; Gross, F.; Koschikowski, J.; Pfeifle, D.; Rolletschek, M.; Subiela, V., Membrane distillation: solar and waste heat driven demonstration plants for desalination. *Desalination* **2013**, *323*, 93-106.
12. Alklaibi, A. M.; Lior, N., Membrane-distillation desalination: Status and potential. *Desalination* **2005**, *171*, 111-131.
13. Boo, C.; Lee, J.; Elimelech, M., Engineering surface energy and nanostructure of microporous films for expanded membrane distillation applications. *Environ. Sci. Technol.* **2016**, *50*, 8112-8119.
14. Woo, Y. C.; Chen, Y.; Tijing, L. D.; Phuntsho, S.; He, T.; Choi, J. S.; Kim, S. H.; Shon, H. K., CF<sub>4</sub> plasma-modified omniphobic electrospun nanofiber membrane for produced water brine treatment by membrane distillation. *J. Membr. Sci.* **2017**, *529*, 234-242.
15. Meindersma, G. W.; Gujit, C. M.; de Hann, A. B., Desalination and water recycling by air gap membrane distillation. *Desalination* **2006**, *187*, 291-301.
16. Eykens, L.; De Sitter, K.; Dotremont, C.; Pinoy, L.; Van der Bruggen, B., How to optimize the membrane properties for membrane distillation: a review. *Ind. Eng. Chem. Res.* **2016**, *55*, 9333-9343.
17. El-Bourawi, M. S.; Ding, Z.; Ma, R.; Khayet, M., A framework for better understanding membrane distillation separation process. *J. Membr. Sci.* **2006**, *285*, 4-29.
18. Yang, X.; Wang, R.; Shi, L.; Fane, A. G.; Debowski, M., Performance improvement of PVDF hollow fiber-based membrane distillation process. *J. Membr. Sci.* **2011**, *369*, 437-447.
19. Zhang, J.; Li, D.; Duke, M.; Xie, Z.; Gray, S., Performance of asymmetric hollow fibre membranes in membrane distillation under various configurations and vacuum enhancement. *J. Membr. Sci.* **2010**, *362*, 517-528.
20. Adham, S.; Hussain, A.; Matar, J. M.; Dores, R.; Janson, A., Application of membrane distillation for desalting brines from thermal desalination plants. *Desalination* **2013**, *314*, 101-108.
21. Wang, P.; Chung, T. S., Recent advances in membrane distillation processes: membrane development, configuration design and application exploring. *J. Membr. Sci.* **2015**, *474*, 39-56.

22. Song, L.; Ma, Z.; Liao, X.; Kosaraju, P. B.; Irish, J. R.; Sirkar, K. K., Pilot plant studies of novel membranes and devices for direct contact membrane distillation- based desalination. *J. Membr. Sci.* **2008**, *323*, 257-270.
23. Han, D.; Steckl, A. J., Superhydrophobic and oleophobic fibers by coaxial electrospinning. *Langmuir* **2009**, *25*, 9454-9462.
24. Martínez, L.; Rodríguez-Maroto, J. M., Membrane thickness reduction effects on direct contact membrane distillation performance. *J. Membr. Sci.* **2008**, *312*, 143-156.
25. Eykens, L.; Hitsov, I.; De Sitter, K.; Dotremont, C.; Pinoy, L.; Nopens, I.; Van der Bruggen, B., Influence of membrane thickness and process conditions on direct contact membrane distillation at different salinities, *J. Membr. Sci.* **2016**, *498*, 353-364.
26. Wu, H. Y.; Wang, R.; Field, R. W., Direct contact membrane distillation: An experimental and analytical investigation of the effect of membrane thickness upon transmembrane flux. *J. Membr. Sci.* **2014**, *470*, 257-265.
27. Woods, J.; Pellegrino, J.; Burch, J., Generalized guidance for considering pore-size distribution in membrane distillation. *J. Membr. Sci.* **2011**, *368*, 124-133.
28. Phattaranawik, J., Effect of pore size distribution and air flux on mass transport in direct contact membrane distillation. *J. Membr. Sci.* **2003**, *215*, 75-85.
29. Alkhudhiri, A.; Darwish, N.; Hilal, N., Membrane distillation: A comprehensive review. *Desalination* **2012**, *287*, 2-18.
30. García-Payo, M. C.; Izquierdo-Gil, M. A., Thermal resistance technique for measuring the thermal conductivity of thin microporous membranes. *J. Phys. D: Appl. Phys.* **2004**, *37*, 3008-3016.
31. Tijjng, L. D.; Woo, Y. C.; Choi, J. S.; Lee, S.; Kim, S. H.; Shon, H. K., Fouling and its control in membrane distillation-A review. *J. Membr. Sci.* **2015**, *475*, 215-244.
32. Meng, F.; Chae, S. R.; Drews, A.; Kraume, M.; Shin, H. S.; Yang, F., Recent advances in membrane bioreactors (MBRs): Membrane fouling and membrane material. *Water Res.* **2009**, *43*, 1489-1512.

33. Gryta, M.; Tomaszewska, M.; Karakulski, K., Wastewater treatment by membrane distillation. *Desalination* **2006**, *198*, 67-73.
34. Tang, C. Y.; Chong, T. H.; Fane, A.G., Colloidal interactions and fouling of NF and RO membranes: a review. *Adv. Colloid Interface Sci.* **2011**, *164*, 126-143.
35. Guillen-Burrieza, E.; Thomas, R.; Mansoor, B.; Johnson, D.; Hilal, N.; Arafat, H., Effect of dry-out on the fouling of PVDF and PTFE membranes under conditions simulating intermittent seawater membrane distillation (SWMD). *J. Membr. Sci.* **2013**, *438*, 126-139.
36. Laqbaqbi, M.; Sanmartino, J. A.; Khayet, M.; García-Payo, C.; Chaouch, M., Fouling in membrane distillation, osmotic distillation and osmotic membrane distillation. *Appl. Sci.* **2017**, *7*(4), 334.
37. Gryta, M., Influence of polypropylene membrane surface porosity on the performance of membrane distillation process. *J. Membr. Sci.* **2007**, *287*, 67-78.
38. Liao, Y.; Wang, R.; Tian, M.; Qiu, C.; Fane, A. G., Fabrication of polyvinylidene fluoride (PVDF) nanofiber membranes by electro-spinning for direct contact membrane distillation. *J. Membr. Sci.* **2013**, *425-426*, 30-39.
39. An, A. K.; Guo, J.; Lee, E. J.; Jeong, S.; Zhao, Y.; Wang, Z.; Leiknes, T., PDMS/PVDF hybrid electrospun membrane with superhydrophobic property and drop impact dynamics for dyeing wastewater treatment using membrane distillation. *J. Membr. Sci.* **2017**, *525*, 57-67.
40. Islam, M., Emerging materials and membrane-based processes for recycling hydraulic fracturing wastewater, Doctoral dissertation, **2018**, Concordia University.
41. Cui, J., Lu, T., Li, F., Wang, Y., Lei, J., Ma, W., Zou, Y., Huang, C. Flexible and transparent composite nanofibre membrane that was fabricated via a “green” electrospinning method for efficient particulate matter 2.5 capture. *J. Colloid Interface Sci.* **2021**, *582*, 506-514.
42. Essalhi, M.; Khayet, M., Self-sustained webs of polyvinylidene fluoride electrospun nanofibers: effects of polymer concentration and desalination by direct contact membrane distillation, *J. Membr. Sci.* **2014**, *454*, 133-143.
43. Lalia, B. S.; Guillen, E.; Arafat, H. A.; Hashaikeh, R., Nanocrystalline cellulose reinforced PVDF-HFP membranes for membrane distillation application. *Desalination* **2014**, *332*, 134-141.

44. Amarjargal, A.; Tijing, L. D.; Park, C. H.; Im, I. T.; Kim, C. S., Controlled assembly of superparamagnetic iron oxide nanoparticles on electrospun PU nanofibrous membrane: a novel heat-generating substrate for magnetic hyperthermia application. *Eur. Polym. J.* **2013**, *49*, 3796-3805.
45. Amarjargal, A.; Tijing, L.D.; Shon, H.K.; Park, C.-H.; Kim, C. S., Facile in situ growth of highly monodispersed Ag nanoparticles on electrospun PU nanofiber membranes: Flexible and high efficiency substrates for surface enhanced Raman scattering. *Appl. Surf Sci.* **2014**, *308*, 396-401.
46. Shirtcliffe, N. J.; McHale, G.; Atherton, S.; Newton, M. I., An introduction to superhydrophobicity. *Adv. Colloid Interface Sci.* **2010**, *161*, 124-138.
47. Costa, M. N.; Veigas, B.; Jacob, J. M.; Santos, D. S.; Gomes, J.; Baptista, P. V.; Martins, R.; Inácio, J.; Fortunato, E., A low cost, safe, disposable, rapid and self-sustainable paper-based platform for diagnostic testing: lab-on-paper. *Nanotechnology* **2014**, *25*, 094006.
48. Yao, L.; He, J., Recent progress in antireflection and self-cleaning technology-From surface engineering to functional surfaces. *Prog. Mater. Sci.* **2014**, *61*, 94-143.
49. Razmjou, A.; Arifin, E.; Dong, G.; Mansouri, J.; Chen, V., Superhydrophobic modification of TiO<sub>2</sub> nanocomposite PVDF membranes for applications in membrane distillation. *J. Membr. Sci.* **2012**, *415*, 850-863.
50. Dimitrakellis, P.; Gogolides, E., Hydrophobic and superhydrophobic surfaces fabricated using atmospheric pressure cold plasma technology: a review. *Adv. Colloid Interface Sci.* **2018**, *254*, 1-21.
51. Zhang, C.; Wu, Y.; Liu, L., Robust hydrophobic Fe-based amorphous coating by thermal spraying. *Appl. Phys. Lett.* **2012**, *101*, 121603.
52. Sharifi, N.; Pugh, M.; Moreau, C.; Dolatabadi, A., Developing hydrophobic and superhydrophobic TiO<sub>2</sub> coatings by plasma spraying. *Surf. Coat. Technol.* **2016**, *289*, 29-36.
53. Esfahani, M. R.; Aktij, S. A.; Dabaghian, Z.; Firouzjaei, M. D.; Rahimpour, A.; Eke, J.; Escobar, I. C.; Abolhassani, M.; Greenlee, L. F.; Esfahani, A. R.; Sadmani, A. H. M. A.; Koutahzadeh, N., Nanocomposite membranes for water separation and purification: Fabrication, modification, and applications. *Sep. Purif. Technol.* **2019**, *213*, 465-499.

54. Yang, M.; Liu, W.; Jiang, C.; He, S.; Xie, Y.; Wang, Z., Fabrication of superhydrophobic cotton fabric with fluorinated TiO<sub>2</sub> sol by a green and one-step sol-gel process. *Carbohydr. Polym.* **2018**, *197*, 75-82.
55. Yang, J.; Li, H.; Lan, T.; Peng, L.; Cui, R.; Yang, H., Preparation, characterization, and properties of fluorine-free superhydrophobic paper based on layer-by-layer assembly. *Carbohydr. Polym.* **2017**, *178*, 228-237.
56. Ogawa, T.; Ding, B.; Sone, Y.; Shiratori, S., Super-hydrophobic surfaces of layer-by-layer structured film-coated electrospun nanofibrous membranes. *Nanotechnology* **2007**, *18*, 165607.
57. Kim, E. K.; Lee, C. S.; Kim, S. S., Superhydrophobicity of electrospray-synthesized fluorinated silica layers. *J. Colloid Interface Sci.* **2012**, *368*, 599-602.
58. Shahabadi, S. M. S.; Rabiee, H.; Seyedi, S. M.; Mokhtare, A.; Brant, J. A., Superhydrophobic dual layer functionalized titanium dioxide/polyvinylidene fluoride-co-hexafluoropropylene (TiO<sub>2</sub>/PH) nanofibrous membrane for high flux membrane distillation. *J. Membr. Sci.* **2017**, *537*, 140-150.
59. Treccani, L.; Klein, T. Y.; Meder, F.; Pardun, K.; Rezwani, K., Functionalized ceramics for biomedical, biotechnological and environmental applications. *Acta Biomater.* **2013**, *9*, 7115-7150.
60. Hsieh, C. T.; Wu, F. L.; Chen, W. Y., Super water-and oil-repellencies from silica-based nanocoatings. *Surf. Coat. Technol.* **2009**, *203*, 3377-3384.
61. Wenzel, R. N., Resistance of solid surfaces to wetting by water. *Ind. Eng. Chem. Res.* **1936**, *28*, 988-994.
62. Cassie, A. B. D.; Baxter, S., Wettability of porous surfaces. *J. Chem. Soc. Faraday Trans.* **1994**, *40*, 546-551.
63. Tuteja, A.; Choi, W.; Ma, M.; Mabry, J. M.; Mazzella, S. A.; Rutledge, G. C.; McKinley, G. H.; Cohen, R. E., Designing superoleophobic surfaces. *Sci.* **2007**, *318*, 1618-1622.
64. Tuteja, A.; Choi, W.; McKinley, G. H.; Cohen, R. E.; Rubner, M. F., Design parameters for superhydrophobicity and superoleophobicity. *MRS Bull.* **2008**, *33*, 752-758.
65. Hong, K.; Kim, Y., Facile fabrication of superamphiphobic glass coated with fluorinated-silica nanoparticles. *Mater. Lett.* **2018**, *229*, 213-216.

66. Mora, L. V.; Taylor, A.; Paul, S.; Dawson, R.; Wang, C.; Taleb, W.; Owen, J.; Neville, A.; Barker, R., Impact of silica nanoparticles on the morphology and mechanical properties of sol-gel derived coatings. *Surf. Coat. Technol.* **2018**, *342*, 48-56.
67. Ortel, E.; Sokolov, S.; Kraehnert, R., Influence of steel substrate roughness on morphology and mesostructure of TiO<sub>2</sub> porous layers produced by template-assisted dip coating. *Microporous Mesoporous Mater.* **2010**, *127*, 17-24.
68. Li, C.; Sun, Y.; Cheng, M.; Sun, S.; Hu, S., Fabrication and characterization of a TiO<sub>2</sub>/polysiloxane resin composite coating with full-thickness super-hydrophobicity. *Chem. Eng. J.* **2018**, *333*, 361-369.
69. Liu, X.; Choi, H. S.; Park, B. R.; Lee, H. K., Amphiphobicity of polyvinylidene fluoride porous films after atmospheric pressure plasma intermittent etching. *Appl. Surf. Sci.* **2011**, *257*, 8828-8835.
70. Lu, K. J.; Zuo, J.; Chang, J.; Kuan, H. N.; Chung, T. S., Omniphobic hollow-fiber membranes for vacuum membrane distillation. *Environ. Sci. Technol.* **2018**, *52*, 4472-4480.
71. Zheng, R.; Chen, Y.; Wang, J.; Song, J.; Li, X. M.; He, T., Preparation of omniphobic PVDF membrane with hierarchical structure for treating saline oily wastewater using direct contact membrane distillation. *J. Membr. Sci.* **2018**, *555*, 197-205.
72. Chen, L. H.; Huang, A.; Chen, Y. R.; Chen, C. H.; Hsu, C. C.; Tsai, F. Y.; Tung, K. L., Omniphobic membranes for direct contact membrane distillation: Effective deposition of zinc oxide nanoparticles. *Desalination* **2018**, *428*, 255-263.
73. Saengkaew, J.; Le, D.; Samart, C.; Sawada, H.; Nishida, M.; Chanlek, N.; Kongparakul, S.; Kiatkamjornwong, S., Superhydrophobic coating from fluoroalkylsilane modified natural rubber encapsulated SiO<sub>2</sub> composites for self-driven oil/water separation. *Appl Surf Sci.* **2018**, *462*, 164-174.
74. Wang, X.; Hu, H.; Ye, Q.; Gao, T.; Zhou, F.; Xue, Q., Superamphiphobic coatings with coralline-like structure enabled by one-step spray of polyurethane/carbon nanotube composites. *J. Mater. Chem.* **2012**, *22*, 9624-9631.
75. Zhang, J.; Seeger, S., Superoleophobic Coatings with Ultralow Sliding Angles Based on Silicone Nanofilaments. *Angew. Chem., Int. Ed.* **2011**, *50*, 6652-6656.

76. Özmen, E.; Durán, A.; Castro, Y., Hydrophobic and oleophobic sol-gel coatings on glass substrates for usage at high temperatures. *Int. J. Appl. Glass Sci.* **2018**, *9*, 413-420.
77. Pan, S.; Kota, A. K.; Mabry, J. M.; Tuteja, A., Superomniphobic surfaces for effective chemical shielding. *J. Am. Chem. Soc.* **2012**, *135*, 578-581.
78. Airoudj, A.; Bally-Le Gall, F.; Roucoules, V., Textile with durable janus wetting properties produced by plasma polymerization. *J. Phys. Chem. A* **2016**, *120*, 29162-29172.
79. Xue, C. H.; Fan, Q. Q.; Guo, X. J.; An, Q. F.; Jia, S. T., Fabrication of superhydrophobic cotton fabrics by grafting of POSS-based polymers on fibers. *Appl. Surf. Sci.* **2019**, *465*, 241-248.
80. Xiong, D.; Liu, G.; Hong, L.; Duncan, E. S., Superamphiphobic diblock copolymer coatings. *Chem. Mater.* **2011**, *23*, 4357-4366.
81. Ganesh, V. A.; Dinachali, S. S.; Raut, H. K.; Walsh, T. M.; Nair, A. S.; Ramakrishna, S., Electrospun SiO<sub>2</sub> nanofibers as a template to fabricate a robust and transparent superamphiphobic coating. *RSC Adv.* **2013**, *3*, 3819-3824.
82. Vilcnik, A.; Jerman, I.; Šurca Vuk, A.; Kozelj, M.; Orel, B.; Tomsic, B.; Simončič, B.; Kovac, J., Structural properties and antibacterial effects of hydrophobic and oleophobic sol-gel coatings for cotton fabrics. *Langmuir* **2009**, *25*, 5869-5880.
83. Jin, C.; Jiang, Y.; Niu, T.; Huang, J., Cellulose-based material with amphiphobicity to inhibit bacterial adhesion by surface modification. *J. Mater. Chem.* **2012**, *22*, 12562-12567.
84. Zhu, X.; Dudchenko, A.; Gu, X.; Jassby, D., Surfactant-stabilized oil separation from water using ultrafiltration and nanofiltration. *J. Membr. Sci.* **2017**, *529*, 159.
85. Rodriguez-Mozaz, S.; Ricart, M.; Köck-Schulmeyer, M.; Guasch, H.; Bonnineau, C.; Proia, L.; Lopez de Alda, M.; Sabater, S.; Barceló, D., Pharmaceuticals and pesticides in reclaimed water: Efficiency assessment of a microfiltration–reverse osmosis (MF-RO) pilot plant. *J. Hazard. Mater.* **2015**, *282*, 165.
86. Hull, E.J.; Zodrow, K. R., Acid rock drainage treatment using membrane distillation: Impacts of chemical-free pretreatment on scale formation, pore wetting, and product water quality. *Environ. Sci. Tech.* **2017**, *51*, 11928.
87. Lee, J.; Boo, C.; Ryu, W. H.; Taylor, A. D.; Elimelech, M., Development of omniphobic desalination membranes using a charged electrospun nanofiber scaffold. *ACS Appl. Mater.*

*Interfaces* **2016**, 8, 11154.

88. Ahmed, F. E.; Lalia, B. S.; Hashaikh, R., Membrane-based detection of wetting phenomenon in direct contact membrane distillation. *J. Membr. Sci.* **2017**, 535, 89.

89. Sundaram, N. T. K.; Subramania, A. Microstructure of PVDF-co-HFP based electrolyte prepared by preferential polymer dissolution process., *J. Membr. Sci.* **2007**, 289, 1.

90. Gadinski, M. R.; Chanthad, C.; Han, K.; Dong, L.; Wang, Q., Synthesis of poly(vinylidene fluoride-co-bromotrifluoroethylene) and effects of molecular defects on microstructure and dielectric properties. *Polym. Chem.* **2014**, 5, 5957.

91. Stephan, A. M.; Teeters, D., Characterization of PVDF-HFP polymer membranes prepared by phase inversion techniques. *Electrochimica Acta.* **2003**, 48, 2143.

92. Fadhil, S.; Marino, T.; Makki, H. F.; Alsahy, Q. F.; Blefari, S.; Macedonio, F.; Nicolò, E. D.; Giorno, L.; Drioli, E.; Figoli, A., Novel PVDF-HFP flat sheet membranes prepared by triethyl phosphate (TEP) solvent for direct contact membrane distillation. *Chem. Eng. Process.* **2016**, 102, 16.

93. Novoselov, K. S.; Geim, A. K.; Morozov, S. V.; Jiang, D.; Zhang, Y.; Dubonos, S.V.; Grigorieva, I. V.; Firsov, A. A., Electric field effect in atomically thin carbon films. *Sci.* **2004**, 306, 666.

94. Perreault, F.; Jaramillo, H.; Xie, M.; Ude, M.; Nghiem, L.D.; Elimelech, M., Biofouling mitigation in forward osmosis using graphene oxide functionalized thin-film composite membranes. *Environ. Sci. Technol.* **2016**, 50, 5840.

95. Becerril, H. A.; Mao, J.; Liu, Z.; Stoltenberg, R. M.; Bao, Z.; Chen, Y., Evaluation of Solution-Processed Reduced Graphene Oxide Films as Transparent Conductors. *ACS Nano* **2008**, 2, 463.

96. Luechinger, N. A.; Booth, N.; Heness, G.; Bandyopadhyay, S.; Grass R. N.; Stark, W. J., Surfactant-Free, Melt-Processable Metal-Polymer Hybrid Materials: Use of Graphene as a Dispersing Agent. *Adv. Mater.* **2008**, 20, 3044.

97. Kang, S. M.; Park, S.; Kim, D.; Park, S. Y.; Ruoff, R. S.; Lee, H., Simultaneous Reduction and Surface Functionalization of Graphene Oxide by Mussel-Inspired Chemistry. *Adv. Funct. Mater.* **2011**, 21, 108.

98. Wang, S.; Zhang, Y.; Abidi, N.; Cabrales, L., Wettability and surface free energy of graphene films. *Langmuir* **2009**, 25, 11078.

99. Lee, J. S.; Yoon, J. C.; Jang, J. H., A route towards superhydrophobic graphene surfaces: surface-treated reduced graphene oxide spheres. *J. Mater. Chem. A* **2013**, *1*, 7312.
100. Tanugi, D. C.; Grossman, J. C., Water desalination across nanoporous graphene. *Nano Lett.* **2012**, *12*, 3602.
101. Mahmoud, K. A.; Mansoor, B.; Mansour, A.; Khraisheh, M., Functional graphene nanosheets: The next generation membranes for water desalination. *Desalination* **2015**, *356*, 208.
102. Li, Y.; Zhu, L., Evaluation of the antifouling and photocatalytic properties of novel poly(vinylidene fluoride) membranes with a reduced graphene oxide-Bi<sub>2</sub>WO<sub>6</sub> active layer. *J. Appl. Polym. Sci.* **2017**, *134*, 45426.
103. Tian, S.; Li, L.; Sun, W.; Xia, X.; Han, D.; Li, J.; Gu, C., Robust adhesion of flower-like few-layer graphene nanoclusters. *Sci. Rep.*, **2012**, *2*, 511.
104. Hu, M.; Mi, B., Enabling Graphene Oxide Nanosheets as Water Separation Membranes. *Environ. Sci. Technol.* **2013**, *47*, 3715
105. Sun, P.; Zhu, M.; Wang, K.; Zhong, M.; Wei, J.; Wu, D.; Xu, Z.; Zhu, H., Selective Ion Penetration of Graphene Oxide Membranes. *ACS Nano* **2013**, *7*, 428.
106. Lalia, B. S.; Guillen-Burrieza, E.; Arafat, H. A.; Hashaikh, R., Fabrication and characterization of polyvinylidene fluoride-co-hexafluoropropylene (PVDF-HFP) electrospun membranes for direct contact membrane distillation. *J. Membr. Sci.* **2013**, *428*, 104.
107. Tijing, L. D.; Choi, J. S.; Lee, S.; Kim, S. H.; Shon, H. K., Recent progress of membrane distillation using electrospun nanofibrous membrane. *J. Membr. Sci.* **2014**, *453*, 435.
108. Suja, P. S.; Reshmi, C. R.; Sagitha, P.; Sujith, A., Electrospun Nanofibrous Membranes for Water Purification. *Polym. Rev.* **2017**, *57*, 467.
109. Gopal, R., Electrospun nanofibrous filtration membrane. *J. Membr. Sci.* **2006**, *281*, 581.
110. Essalhi, M.; Khayet, M., Self-sustained webs of polyvinylidene fluoride electrospun nanofibers at different electrospinning times: 1. Desalination by direct contact membrane distillation. *J. Membr. Sci.* **2013**, *433*, 167.
111. Maab, H.; Francis, L.; Al-Saadi, A.; Aubry, C.; Ghaffour, N.; Amy, G.; Nunes, S. P., Synthesis and fabrication of nanostructured hydrophobic polyazole membranes for low-energy water recovery. *J. Membr. Sci.* **2012**, *423-424*, 11.
112. Prince, J. A.; Rana, D.; Matsuura, T.; Ayyanar, N.; Shanmugasundaram, T. S.; Singh, G., Nanofiber based triple layer hydrophilic/phobic membrane-a solution for pore wetting in

membrane distillation. *Sci. Rep.* **2014**, *4*, 6949.

113. Yao, S. H.; Yuan, J. K.; Zhou, T.; Dang, Z. M.; Bai, J. B., Stretch-modulated carbon nanotube alignment in ferroelectric polymer composites: characterization of the orientation state and its influence on the dielectric properties. *J. Phys. Chem. C.* **2011**, *115*, 20011.

114. Yu, L., Zhang, Y. H., Tong, W. S., Shang, J. W., Shen, B. Lv, F. Z., Chu, P. K., Green dielectric materials composed of natural graphite minerals and biodegradable polymer. *RSC Adv.* **2012**, *2*, 8793.

115. Ferrari, A. C.; Basko, D. M., Raman spectroscopy as a versatile tool for studying the properties of graphene. *Nat. Nanotechnol.* **2013**, *8*, 235.

116. Tong, W.; Zhang, Y.; Yu, L.; Luan, X.; An, Q.; Zhang, Q.; Lv, F.; Chu, P. K.; Shen, B.; Zhang, Z., Novel method for the fabrication of flexible film with oriented arrays of graphene in poly(vinylidene fluoride-co-hexafluoropropylene) with low dielectric loss. *J. Phys. Chem. C.* **2014**, *118*, 10567.

117. Tong, W.; Zhang, Y.; Zhang, Q.; Luan, X.; Lv, F.; Liu, L.; An, Q., An all-solid-state flexible piezoelectric high-k film functioning as both a generator and in situ storage unit. *Adv. Funct. Mater.* **2015**, *25*, 7029.

118. Jin, Z. X.; Pramoda, K. P.; Goh, S. H.; Xu, G. Q., Poly (vinylidene fluoride)-assisted melt-blending of multi-walled carbon nanotube/poly (methyl methacrylate) composites. *Mater. Res. Bull.* **2002**, *37*, 271.

119. Pan, C. Y.; Xu, G. R.; Xu, K.; Zhao, H. L.; Wu, Y. Q.; Su, H. C.; Xu, J. M.; Das, R., Electrospun nanofibrous membranes in membrane distillation: Recent developments and future perspectives. *Sep. Purif. Technol.* **2019**, *221*, 44-63.

120. Deshmukh, A.; Elimelech, M., Understanding the impact of membrane properties and transport phenomena on the energetic performance of membrane distillation desalination. *J. Membr. Sci.*, **2017**, *539*, 458.

121. Curcio, E.; Drioli, E., Membrane distillation and related operations - A Review. *Sep. Purif. Rev.* **2005**, *34*, 35.

122. Schofield, R.W.; Fane, A.G.; Fell, C. J. D., Gas and vapour transport through microporous membranes. I. Knudsen-Poiseuille transition, *J. Membr. Sci.* **1990**, *53*, 159.

123. Soliman, S.; Sant, S.; Nichol, J. W.; Khabiry, M.; Traversa, E.; Khademhosseini, A.,

Controlling the porosity of fibrous scaffolds by modulating the fiber diameter and packing density. *J. Biomed. Mater. Res. A* **2011**, *96*, 566-574.

124. Ugrozov, V. V.; Elkinab, I. B., Mathematical modeling of influence of porous structure a membrane on its vapour-conductivity in the process of membrane distillation. *Desalination* **2002**, *147*, 167.

125. Schofield, R. W.; Fane, A. G.; Fell, C. J. D., Heat and mass-transfer in membrane distillation. *J. Membr. Sci.* **1987**, *33*, 299.

126. Cho, D. W.; Song, H.; Yoon, K.; Kim, S.; Han, J.; Cho, J., Treatment of simulated coalbed methane produced water using direct contact membrane distillation. *Water* **2016**, *8*, 194.

127. Li, X.; Wang, C.; Yang, Y.; Wang, X.; Zhu, M.; Hsiao, B. S., Dual-biomimetic superhydrophobic electrospun polystyrene nanofibrous membranes for membrane distillation. *ACS Appl. Mater. Interfaces* **2014**, *6*, 2423.

128. Huang, L.; Pei, J.; Jiang, H.; Hu, X., Water desalination under one sun using graphene-based material modified PTFE membrane. *Desalination* **2018**, *442*, 1.

129. Duong, H. C.; Chivas, A. R.; Nelemans, B.; Duke, M.; Gray, S.; Cath, T. Y.; Nghiem, L. D., Treatment of RO brine from CSG produced water by spiral-wound air gap membrane distillation - A pilot study. *Desalination* **2015**, *366*, 121.

130. Prince, J. A.; Singh, G.; Rana, D.; Matsuura, T.; Anbharasi, V.; Shanmugasundaram, T. S., Preparation and characterization of highly hydrophobic poly (vinylidene fluoride)-clay nanocomposite nanofiber membranes (PVDF-Clay NNMS) for desalination using direct contact membrane distillation. *J. Membr. Sci.* **2012**, *397*, 80.

131. Wang, K.; Chung, T. S.; Gryta, M., Hydrophobic PVDF hollow fiber membranes with narrow pore size distribution and ultra-thin skin for the fresh water production through membrane distillation. *Chem. Eng. Sci.* **2008**, *63*, 2587.

132. Bonyadi, S.; Chung, T. S., Flux enhancement in membrane distillation by fabrication of dual layer hydrophilic–hydrophobic hollow fiber membranes. *J. Membr. Sci.* **2007**, *306*, 134.

133. Bhadra, M.; Roy, S.; Mitra, S., Desalination across a graphene oxide membrane via direct contact membrane distillation. *Desalination* **2016**, *378*, 37.

134. Roy, S.; Bhadra, M.; Mitra, S., Enhanced desalination via functionalized carbon nanotube immobilized membrane in direct contact membrane distillation, *Sep. Purif. Technol.* **2014**, *136*, 58.

135. Zheng, L.; Zhang, C.; Kang, S.; Li, C.; Hou, D.; Wu, S.; Wang, J.; Wei, Y., Insight into the microbial distribution and succession and biofouling mechanism in membrane distillation for desulfurization wastewater treatment. *Chem. Eng. J.* **2021**, *428*, 131097.
136. Lin, S.; Yip, N. Y.; Elimelech, M., Direct contact membrane distillation with heat recovery: thermodynamic insights from module scale modeling. *J. Membr. Sci.* **2014**, *453*, 498-515.
137. Li, J., Guan, Y., Cheng, F., Liu, Y., Treatment of high salinity brines by direct contact membrane distillation: Effect of membrane characteristics and salinity. *Chemosphere* **2015**, *140*, 143-149.
138. Wang, Z.; Lin, S., Membrane fouling and wetting in membrane distillation and their mitigation by novel membranes with special wettability. *Water Res.* **2017**, *112*, 38-47.
139. Gryta, M., Effect of iron oxides scaling on the MD process performance, *Desalination* **2007**, *216*, 88-102.
140. Zhong, L.; Wang, Y.; Liu, D.; Zhu, Z.; Wang, W., Recent advances in membrane distillation using Electrospun membrane: advantages, challenges, and outlook. *Environ. Sci.: Water Res. Technol.* **2021**, *7*, 1002-1019.
141. Franken, A. C. M.; Nolten, J. A. M.; Mulder, M. H. V.; Bargeman, D.; Smolders, C. A., Wetting criteria for the applicability of membrane distillation. *J. Membr. Sci.* **1987**, *33*, 315-328.
142. Ganesh, V. A.; Dinachali, S. S.; Raut, H. K.; Walsh, T. M.; Nair, A. S.; Ramakrishna, S., Electrospun SiO<sub>2</sub> nanofibers as a template to fabricate a robust and transparent superamphiphobic coating. *RSC Adv.* **2013**, *3*, 3819-3824.
143. Valipour-Motlagh, N.; Birjandi, F. C.; Sargolzaei, J.; Shahtahmassebi, N., Durable, superhydrophobic, superoleophobic and corrosion resistant coating on the stainless steel surface using a scalable method. *Appl. Surf. Sci.* **2013**, *283*, 636-647.
144. Lu, C., Su, C., Cao, H., Horseman, T., Duan, F., Li, Y., Nanoparticle-free and self-healing amphiphobic membrane for anti-surfactant-wetting membrane distillation. *J Environ Sci.* **2021**, *100*, 298-305.
145. Liu, T.; Kim, C. J., Turning a surface superrepellent even to completely wetting liquids. *Sci.* **2014**, *346*, 1096-1100.
146. Chu, Z.; Seeger, S., Superamphiphobic surfaces. *Chem. Soc. Rev.* **2014**, *43*, 2784-2798.

147. Huang, Y. Z.; Wang, Z.; Hou, D.; Lin, S., Coaxially electrospun super-amphiphobic silica-based membrane for anti-surfactant-wetting membrane distillation, *J. Membr. Sci.* **2017**, *531*, 122-128.
148. Wang, M.; Liu, G.; Yu, H.; Lee, S. H.; Wang, L.; Zheng, J.; Wang, T.; Yun, Y.; Lee, J. K., ZnO nanorod array modified PVDF membrane with superhydrophobic surface for vacuum membrane distillation application. *ACS Appl. Mater. Interfaces* **2018**, *10*, 13452-13461.
149. Badv, M.; Jaffer, I. H.; Weitz, J. I.; Didar, T. F., An omniphobic lubricant-infused coating produced by chemical vapor deposition of hydrophobic organosilanes attenuates clotting on catheter surfaces. *Sci. Rep.* **2017**, *7*(1), 1-10.
150. Ma, W.; Yang, L.; Chen, T.; Ye, Z.; Tufenkji, N.; Rahaman, M. S., Engineering polymer forest on membranes: tuning density, thickness, and architecture for biofouling control. *ACS Appl. Polym. Mater.* **2020**, *2*, 4592-4603.
151. Whitby, R. L. D., Chemical control of graphene architecture: tailoring shape and properties. *ACS Nano.* **2014**, *8*, 9733-9754.
152. Lee, J. S.; Yoon, J. C.; Jang, J. H., A route towards superhydrophobic graphene surfaces: surface-treated reduced graphene oxide spheres. *J. Mater. Chem. A* **2013**, *1*, 7312.
153. Chen, T.; Soroush, A.; Rahaman, M. S., Highly hydrophobic electrospun reduced graphene oxide/poly (vinylidene fluoride-co-hexafluoropropylene) membranes for use in membrane distillation. *Ind. Eng. Chem. Res.* **2018**, *57*, 14535-14543.
154. Liu, M.; Wei, Y. M.; Xu, Z. L.; Guo, R. Q.; Zhao, L. B., Preparation and characterization of polyethersulfone microporous membrane via thermally induced phase separation with low critical solution temperature system. *J. Membr. Sci.* **2013**, *437*, 169-178.
155. Ge, B.; Zhang, Z.; Men, X., Sprayed superamphiphobic coatings on copper substrate with enhanced corrosive resistance. *Appl. Surf. Sci.* **2014**, *293*, 271-274.
156. Shaulsky, E.; Nejati, S.; Boo, C.; Perreault, F.; Osuji, C. O.; Elimelech, M., Post-fabrication modification of electrospun nanofiber mats with polymer coating for membrane distillation applications, *J. Membr. Sci.* **2017**, *530*, 158-165.
157. Xue, Z.; Liu, M.; Jiang, L., Recent developments in polymeric superoleophobic surfaces, *J. Polym. Sci. Pol. Phys.* **2012**, *50*, 1209-1224.

158. Eckmann, A.; Felten, A.; Mishchenko, A.; Britnell, L.; Krupke, R.; Novoselov, K. S.; Casiraghi, C., Probing the nature of defects in graphene by Raman spectroscopy. *Nano Lett.* **2012**, *12*, 3925-3930.
159. Li, X.; Yu, X.; Cheng, C.; Deng, L.; Wang, M.; Wang, X., Electrospun superhydrophobic organic/inorganic composite nanofibrous membranes for membrane distillation. *ACS Appl. Mater. Interfaces* **2015**, *7*, 21919-21930.
160. Wu, X. Q.; Wu, X.; Wang, T. Y.; Zhao, L.; Truong, Y. B.; Ng, D., Zheng, Y. M.; Xie, Z., Omniphobic surface modification of electrospun nanofiber membrane via vapor deposition for enhanced anti-wetting property in membrane distillation. *J. Membr. Sci.* **2020**, *606*, 118075.
161. Tomina, V. V.; Yurchenko, G. R.; Matkovsky, A. K.; Zub, Y. L.; Kosak, A.; Lobnik, A., Synthesis of polysiloxane xerogels with fluorine-containing groups in the surface layer and their sorption properties. *J. Fluor. Chem.* **2011**, *132*, 1146-1151.
162. Dong, Z. Q.; Wang, B. J.; Ma, X. H.; Wei, Y. M.; Xu, Z. L., FAS grafted electrospun poly (vinyl alcohol) nanofiber membranes with robust superhydrophobicity for membrane distillation. *ACS Appl. Mater. Interfaces* **2015**, *7*, 22652-22659.
163. Liao, Y.; Loh, C. H.; Wang, R.; Fane, A. G., Electrospun superhydrophobic membranes with unique structures for membrane distillation. *ACS Appl. Mater. Interfaces* **2014**, *6*, 16035-16048.
164. Wang, W.; Du, X.; Vahabi, H.; Zhao, S.; Yin, Y.; Kota, A. K.; Tong, T., Trade-off in membrane distillation with monolithic omniphobic membranes. *Nat. Commun.* **2019**, *10*, 1-9.
165. Guo, M.; Ding, B.; Li, X.; Wang, X.; Yu, J.; Wang, M., Amphiphobic nanofibrous silica mats with flexible and high-heat-resistant properties. *J. Phys. Chem. C* **2010**, *114*, 916-921.
166. Tao, M.; Xue, L.; Liu, F.; Jiang, L., An intelligent superwetting PVDF membrane showing switchable transport performance for oil/water separation, *Adv. Mater.* **2014**, *26*, 2943-2948.
167. Wang, K. Y.; Chung, T. S.; Gryta, M., Hydrophobic PVDF hollowfiber membranes with narrow pore size distribution and ultra-thin skin for the freshwater production through membrane distillation. *Chem. Eng. Sci.* **2008**, *63*, 2587-2594.
168. Zou, L.; Zhang, X.; Gusnawan, P.; Zhang, G.; Yu, J., Crosslinked PVDF based hydrophilic-hydrophobic dual-layer hollow fiber membranes for direct contact membrane distillation desalination: from the seawater to oilfield produced water. *J. Membr. Sci.* **2021**, *619*, 118802.

169. Abdallah, H.; Moustafa, A. F.; AlAnezi, A. A.; El-Sayed, H. E. M., Performance of a newly developed titanium oxide nanotubes/polyethersulfone blend membrane for water desalination using vacuum membrane distillation. *Desalination* **2014**, *346*, 30-36.
170. Yüksel, E.; Şengil, İ. A.; Özacar, M., The removal of sodium dodecyl sulfate in synthetic wastewater by peroxi-electrocoagulation method, *Chem. Eng. J.* **2009**, *152*, 347-353.
171. An, X.; Liu, Z.; Hu, Y., Amphiphobic surface modification of electrospun nanofibrous membranes for anti-wetting performance in membrane distillation. *Desalination* **2018**, *432*, 23-31.
172. Murakami, D.; Jinnai, H.; Takahara, A., Wetting transition from the Cassie-Baxter state to the Wenzel state on textured polymer surfaces. *Langmuir* **2014**, *30*, 2061-2067.
173. Lin, S.; Nejati, S.; Boo, C.; Hu, Y.; Osuji, C. O.; Elimelech, M., Omniphobic membrane for Robust membrane distillation. *Environ. Sci. Technol. Lett.* **2014**, *1*, 443-447.
174. Li, X.; Qing, W.; Wu, Y.; Shao, S.; Peng, L. E.; Yang, Y.; Wang, P.; Liu, F.; Tang, C. Y., Omniphobic nanofibrous membrane with pine-needle-like hierarchical nanostructures: toward enhanced performance for membrane distillation. *ACS Appl. Mater. Interfaces* **2019**, *11*, 47963-47971.
175. Xiao, Z.; Guo, H.; He, H.; Liu, Y.; Li, X.; Zhang, Y.; Yin, H.; Volkov, A. V.; He, T., Unprecedented scaling/fouling resistance of omniphobic polyvinylidene fluoride membrane with silica nanoparticle coated micropillars in direct contact membrane distillation. *J. Membr. Sci.* **2020**, *599*, 117819.
176. Chen, Y.; Lu, K. J.; Chung, T. S., An omniphobic slippery membrane with simultaneous anti-wetting and anti-scaling properties for robust membrane distillation. *J. Membr. Sci.* **2020**, *595*, 117572.
177. Wang, Z.; Chen, Y.; Lin, S., Kinetic model for surfactant-induced pore wetting in membrane distillation. *J. Membr. Sci.* **2018**, *564*, 275-288.
178. Zhou, T.; Yao, Y.; Xiang, R.; Wu, Y., Formation and characterization of polytetrafluoroethylene nanofiber membranes for vacuum membrane distillation. *J. Membr. Sci.* **2014**, *453*, 402-408.
179. Lu, C.; Su, C.; Cao, H.; Ma, X.; Duan, F.; Chang, J.; Li, Y., F-POSS based omniphobic membrane for robust membrane distillation. *Mater. Lett.* **2018**, *228*, 85-88.

180. Woo, Y. C.; Kim, Y.; Yao, M.; Tijing, L. D.; Choi, J. S.; Lee, S.; Kim, S. H.; Shon, H. K., Hierarchical composite membranes with robust omniphobic surface using layer-by-layer assembly technique. *Environ. Sci. Technol.* **2018**, *52*, 2186-2196.
181. Farinelli, G., Cocha, M., Minella, M., Fabbri, D., Pazzi, M., Vione, D., Tiraferri, A., Evaluation of Fenton and modified Fenton oxidation coupled with membrane distillation for produced water treatment: Benefits, challenges, and effluent toxicity. *Sci. Total Environ.* **2021**, *796*, 148953.
182. Rajwade, K.; Barrios, A. C.; Garcia-Segura, S.; Perreault, F., Pore wetting in membrane distillation treatment of municipal wastewater desalination brine and its mitigation by foam fractionation. *Chemosphere* **2020**, *257*, 127214.
183. Meng, S.; Hsu, Y. C.; Ye, Y.; Chen, V., Submerged membrane distillation for inland desalination applications. *Desalination* **2015**, *361*, 72-80.
184. Deshmukh, A.; Boo, C.; Karanikola, V.; Lin, S.; Straub, A. P.; Tong, T.; Warsinger, D. M.; Elimelech, M., Membrane distillation at the water-energy nexus: limits, opportunities, and challenges. *Energy Environ. Sci.* **2018**, *11*, 1177-1196.
185. Shao, Y.; Han, M.; Wang, Y.; Li, G.; Xiao, W.; Li, X.; Wu, X.; Ruan, X.; Yan, X.; He, G.; Jiang, X., Superhydrophobic polypropylene membrane with fabricated antifouling interface for vacuum membrane distillation treating high concentration sodium/magnesium saline water. *J. Membr. Sci.* **2019**, *579*, 240-252.
186. Khayet, M., Membranes and theoretical modeling of membrane distillation: a review. *Adv. Colloid Interface Sci.* **2011**, *164*, 56-88.
187. Thomas, N.; Mavukkandy, M. O.; Loutatidou, S.; Arafat, H. A., Membrane distillation research & implementation: Lessons from the past five decades. *Sep. Purif. Technol.* **2017**, *189*, 108-127.
188. Bonyadi, S.; Chung, T. S., Flux enhancement in membrane distillation by fabrication of dual layer hydrophilic-hydrophobic hollow fiber membranes. *J. Membr. Sci.* **2007**, *306*, 134-146.
189. Li, Z.; Liu, Y.; Yan, J.; Wang, K.; Xie, B.; Hu, Y.; Kang, W.; Cheng, B., Electrospun polyvinylidene fluoride/fluorinated acrylate copolymer tree-like nanofiber membrane with high flux and salt rejection ratio for direct contact membrane distillation. *Desalination* **2019**, *466*, 68-76.

190. Leitch, M. E.; Li, C.; Ikkala, O.; Mauter, M. S.; Lowry, G. V., Bacterial nanocellulose aerogel membranes: novel high-porosity materials for membrane distillation. *Environ. Sci. Technol. Lett.* **2016**, *3*, 85-91.
191. Qtaishat, M.; Rana, D.; Khayet, M.; Matsuura, T., Preparation and characterization of novel hydrophobic/hydrophilic polyetherimide composite membranes for desalination by direct contact membrane distillation. *J. Membr. Sci.* **2009**, *327*, 264-273.
192. Amooghin, A. E.; Mashhadikhan, S.; Sanaeepur, H.; Moghadassi, A.; Matsuura, T.; Ramakrishna, S., Substantial breakthroughs on function-led design of advanced materials used in mixed matrix membranes (MMMs): A new horizon for efficient CO<sub>2</sub> separation. *Prog. Mater. Sci.* **2019**, *102*, 222-295.
193. Laghaei, M.; Sadeghi, M.; Ghalei, B.; Shahrooz, M., The role of compatibility between polymeric matrix and silane coupling agents on the performance of mixed matrix membranes: polyethersulfone/MCM-41. *J. Membr. Sci.* **2016**, *513*, 20-32
194. Zhao, L.; Lu, X.; Wu, C.; Zhang, Q., Flux enhancement in membrane distillation by incorporating AC particles into PVDF polymer matrix. *J. Membr. Sci.* **2016**, *500*, 46-54.
195. Su, H. L.; Hsu, J. M.; Pan, J. P.; Chern, C. S., Silica nanoparticles modified with vinyltriethoxysilane and their copolymerization with N,N'-bismaleimide-4,4'-diphenylmethane. *J. Appl. Polym. Sci.* **2007**, *103*(6), 3600-3608.
196. Liu, L.; Zhu, G.; Liu, Z.; Gao, C., Effect of MCM-48 nanoparticles on the performance of thin film nanocomposite membranes for reverse osmosis application. *Desalination* **2016**, *394*, 72-82.
197. Cheng, D.; Zhao, L.; Li, N.; Smith, S. J.; Wu, D.; Zhang, J.; Ng, D.; Wu, C.; Martinez, M. R.; Batten, M. P.; Xie, Z., Aluminum fumarate MOF/PVDF hollow fiber membrane for enhancement of water flux and thermal efficiency in direct contact membrane distillation. *J. Membr. Sci.* **2019**, *588*, 117204.
198. Kim, S.; Marand, E.; Ida, J.; Gulians, V. V., Polysulfone and mesoporous molecular sieve MCM-48 mixed matrix membranes for gas separation. *Chem. Mater.* **2006**, *18*, 1149-1155.
199. Gibson, L. T., Mesosilica materials and organic pollutant adsorption: part A removal from air. *Chem. Soc. Rev.* **2014**, *43*, 5163-5172.
200. Zornoza, B.; Tellez, C.; Coronas, J., Mixed matrix membranes comprising glassy polymers and dispersed mesoporous silica spheres for gas separation, *J. Membr. Sci.* **2011**, *368*, 100-109.

201. Zornoza, B.; Irusta, S.; Tellez, C.; Coronas, J., Mesoporous silica sphere-polysulfone mixed matrix membranes for gas separation, *Langmuir* **2009**, *25*, 5903-5909.
202. García-Payo, M. D. C.; Essalhi, M.; Khayet, M., Preparation and characterization of PVDF-HFP copolymer hollow fiber membranes for membrane distillation. *Desalination* **2009**, *245*, 469-473.
203. Ghaee, A.; Ghadimi, A.; Sadatnia, B.; Ismail, A. F.; Mansourpour, Z.; Khosravi, M., Synthesis and characterization of poly (vinylidene fluoride) membrane containing hydrophobic silica nanoparticles for CO<sub>2</sub> absorption from CO<sub>2</sub>/N<sub>2</sub> using membrane contactor. *Chem. Eng. Res. Des.* **2017**, *120*, 47-57.
204. Nik, O. G.; Chen, X. Y.; Kaliaguine, S., Amine-functionalized zeolite FAU/EMT polyimide mixed matrix membranes for CO<sub>2</sub>/CH<sub>4</sub> separation. *J. Membr. Sci.* **2011**, *379*, 468-478.
205. Rahaman, M.S., Islam, M.S., Chen, T., Ma, W., Membranes for forward osmosis and membrane distillation and process for treating fracking wastewater. PCT patent application, PCT/CA2019/051324, 2019.
206. Kim, T. W.; Chung, P. W.; Lin, V. S. Y., Facile synthesis of monodisperse spherical MCM-48 mesoporous silica nanoparticles with controlled particle size. *Chem. Mater.* **2010**, *22*, 5093-5104.
207. Suzuki, K.; Ikari, K.; Imai, H., Synthesis of silica nanoparticles having a well-ordered mesostructure using a double surfactant system. *J. Am. Chem. Soc.* **2004**, *126*, 462-463.
208. Zou, H.; Wu, S.; Shen, J., Polymer/silica nanocomposites: preparation, characterization, properties, and applications. *Chem. Rev.* **2008**, *108*, 3893-3957.
209. Effati, E.; Pourabbas, B., One-pot synthesis of sub-50 nm vinyl-and acrylate-modified silica nanoparticles. *Powder Technol.* **2012**, *219*, 276-283.
210. Xue, L.; Li, J.; Fu, J.; Han, Y., Super-hydrophobicity of silica nanoparticles modified with vinyl groups. *Colloids Surf. A: Physicochem. Eng. Asp.* **2009**, *338*, 15-19.
211. Hou, D.; Wang, Z.; Wang, K.; Wang, J.; Lin, S., Composite membrane with electrospun multiscale-textured surface for robust oil-fouling resistance in membrane distillation. *J. Membr. Sci.* **2018**, *546*, 179-187.
212. Efome, J. E.; Baghbanzadeh, M.; Rana, D.; Matsuura, T.; Lan, C. Q., Effects of superhydrophobic SiO<sub>2</sub> nanoparticles on the performance of PVDF flat sheet membranes for vacuum membrane distillation. *Desalination* **2015**, *373*, 47-57.

213. Tong, W.; Zhang, Y.; Zhang, Q.; Luan, X.; Lv, F.; Liu, L.; An, Q., An all-solid-state flexible piezoelectric high-k film functioning as both a generator and in situ storage unit. *Adv. Funct. Mater.* **2015**, *25*, 7029-7037.
214. Li, W.; Xing, Y.; Xing, X.; Li, Y.; Yang, G.; Xu, L., PVDF-based composite microporous gel polymer electrolytes containing a novel single ionic conductor  $\text{SiO}_2(\text{Li}^+)$ . *Electrochim. Acta* **2013**, *112*, 183-190.
215. Liu, M.; Zheng, Y.; Zhai, J.; Jiang, L., Bioinspired super-antiwetting interfaces with special liquid-solid adhesion. *Acc. Chem. Res.* **2010**, *43*, 368-377.
216. Y. Bao, X. Yan, W. Du, X. Xie, Z. Pan, J. Zhou, L., Li Application of amine-functionalized MCM-41 modified ultrafiltration membrane to remove chromium (VI) and copper (II). *Chem. Eng. J.* **2015**, *281*, 460-467.
217. Li, T., Wang, C., Cheng, J., Guo, J., Xiao, A., Hou, H., Wang, Q., Wang B., Chen, X., Cui, G., Janus polymer composite electrolytes improve the cycling performance of lithium-oxygen battery. *ACS Appl. Mater. Interfaces* **2020**, *12*, 12857-12866.
218. Leo, C. J., Thakur, A. K., Rao, G. V. S., Chowdari, B. V. R., Effect of glass-ceramic filler on properties of polyethylene oxide– $\text{LiCF}_3\text{SO}_3$  complex. *J. Power Sources* **2003**, *115*, 295.
219. Hou, D.; Lin, D.; Ding, C.; Wang, D.; Wang, J., Fabrication and characterization of electrospun superhydrophobic PVDF-HFP/SiNPs hybrid membrane for membrane distillation. *Sep. Purif. Technol.* **2017**, *189*, 82-89.
220. Yang, F.; Efome, J. E.; Rana, D.; Matsuura, T.; Lan, C., Metal-organic frameworks supported on nanofiber for desalination by direct contact membrane distillation. *ACS Appl. Mater. Interfaces* **2018**, *10*, 11251-11260.
221. Guo, J.; Lee, J. G.; Tan, T.; Yeo, J.; Wong, P. W.; Ghaffour, N.; An, A. K., Enhanced ammonia recovery from wastewater by Nafion membrane with highly porous honeycomb nanostructure and its mechanism in membrane distillation. *J. Membr. Sci.* **2019**, *590*, 117265.
222. Wang, Z.; Sun, L.; Wang, Q.; Li, B.; Wang, S., A novel approach to fabricate interconnected sponge-like and highly permeable polyvinylidene fluoride hollow fiber membranes for direct contact membrane distillation. *Eur. Polym. J.* **2014**, *60*, 262-272.

## Appendices

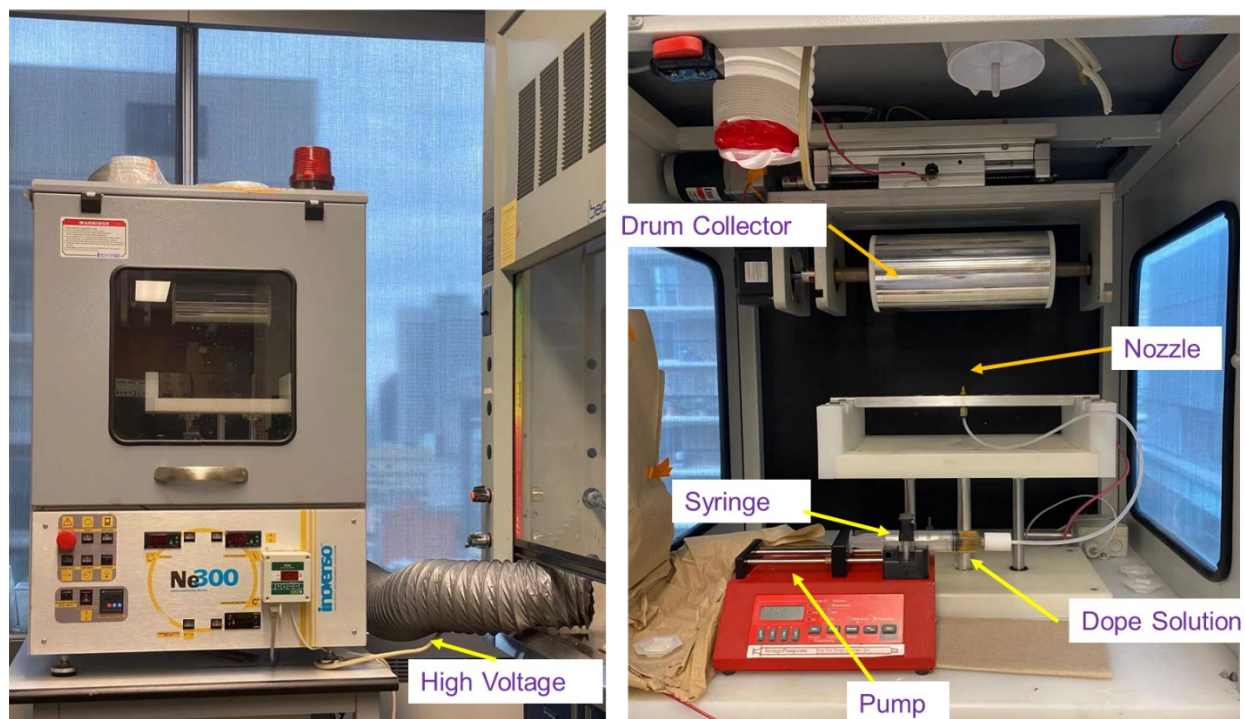


**Figure A-1.** Image of the electrospinning machine. The dope solution in the syringe is pumped to the nozzle, under the influence of electric field provided by the high voltage power supply, the polymer solution is positively charged. Once the electrostatic force overcomes the surface tension, the polymer will be ejected from the nozzle and move towards the negatively charged collector. Solvents start to evaporate and solidified fibers will be deposited on the collector as non-woven mat. The membrane morphology and properties are determined by the operation parameters like voltage and pump rate; the polymer concentration or solvents in the dope solution will also affect the nanofibers formation.

**Table A-1. Optimization of dope solution for the PH-rGO electrospun membrane**

<b>Ratio</b> (DMAc/Acetone, v/v)	<b>Description</b>
8:2	many beads, bumpy surface
6:4	discontinuous fibers produced, fragile
2:3	continuous fibers, smooth surface

The solvent ratio of DMAc:Acetone varied from 8:2 (v:v) to 2:3 (v:v) to generate uniform nanofibers. Only under the ratio of 2:3, continuous fibers ejected from the nozzle and finally formed a smooth nanofibrous mat on the collector.

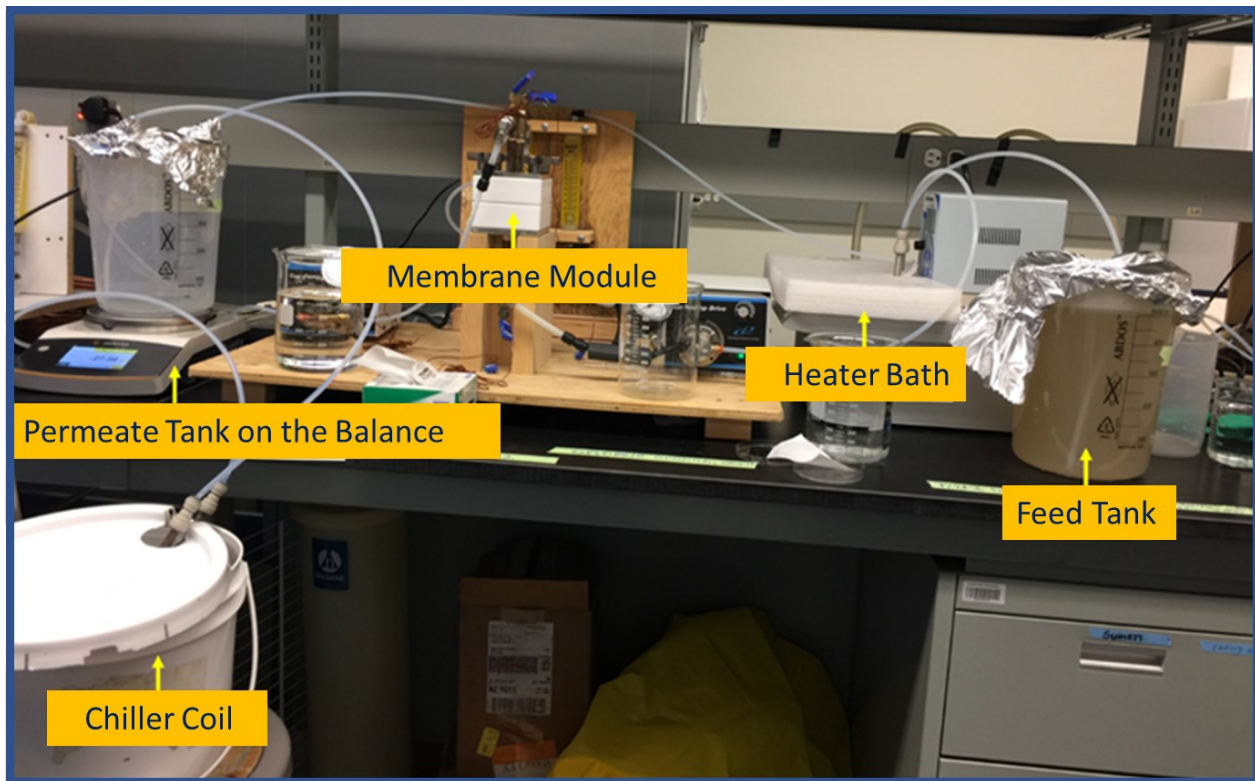


**Figure A-2.** Image of the laboratory scale DCMD setup. The flat-sheet membrane, with an effective area of  $34 \text{ cm}^2$ , was tightly affixed into the PTFE membrane cell (CF042P-FO, Sterlitech Corporation, USA). The hot feed solution was maintained in a constant temperature water bath. The feed solution and the cold solution were circulated at the same speed across the lower and upper face of the membrane cell respectively with two gear pumps (GH-75211-10, Cole-parmer, Canada). The circulation feed rate and permeate rate were measured by two flowmeters (0.1-1 LPM, McMaster-CARR, Canada). Operational temperature was monitored at the inlet and outlet of the module using four thermocouples (SCPSS-032u-6, OMEGA, Canada) connected to a thermometer (EW-91427-00, Cole-Parmer, Canada).

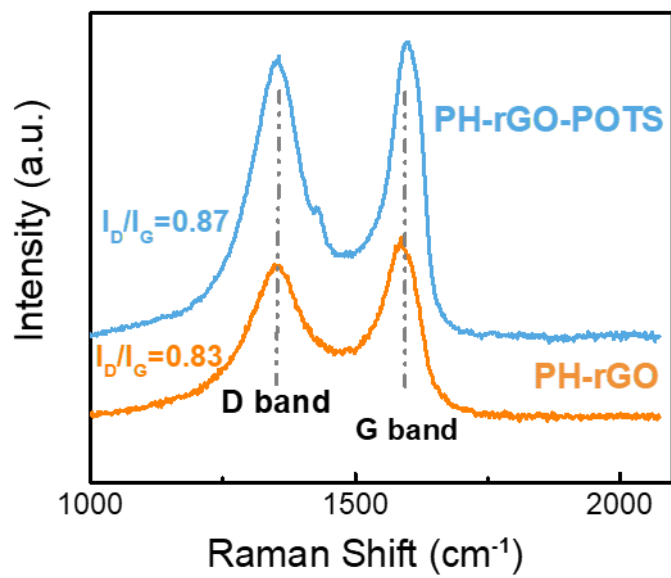


**Figure A-3.** Raman spectra of (A) PH-rGO membrane and (B) PH-rGO-POTS membrane.

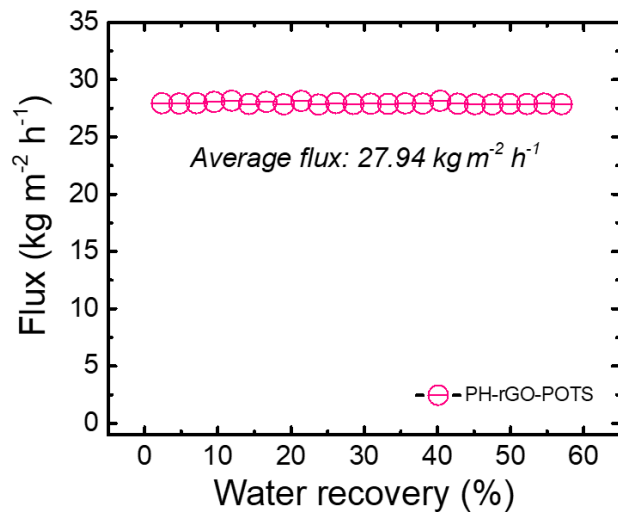


**Figure A-4.** Water flux as the function of the water recovery for the PH-rGO-POTS membrane during the long-term stability in presence of mixed foulants (35 g/L NaCl, 20 mM CaCl<sub>2</sub>, 20 mM Na<sub>2</sub>SO<sub>4</sub>, 100 mg/L humic acid sodium salt, 10 mg/L machine oil, and 0.05 mM SDS). The feed solution was maintained at 65 °C and the permeate was maintained at 15 °C. The flow rate of feed and permeate streams were both 0.7 LPM.

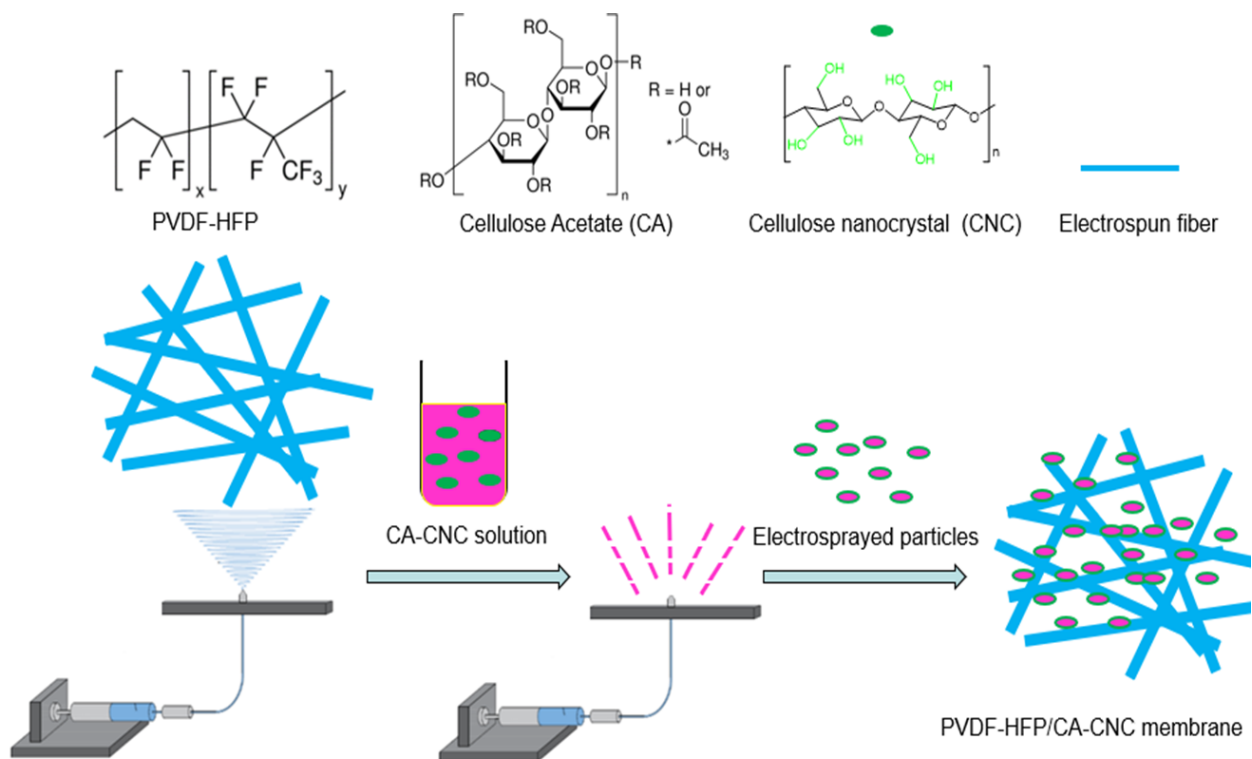


**Figure A-5.** Schematic illustration of the procedure for fabricating the hydrophilic/hydrophobic composite membrane. Hydrophobic membranes used in MD are easily wetted or fouled by oils due to hydrophobic-hydrophobic interactions, which hinders the application of MD in the treatment of oily wastewater. To overcome this, a thin in-air hydrophilic and underwater oleophobic top layer of cellulose acetate (CA) - cellulose nanocrystals (CNCs) could be deposited by electrospinning process on a hydrophobic electrospun PVDF-HFP substrate. The hydrophilic hydroxyl groups of the CA and CNCs would interact with water and provide a hydration layer that help to prevent the attachment of oil substances. As the ester form of natural polymer cellulose, CA can be easily processed into fibers, films and membranes from either solutions or melts. CA is widely used as a hydrophilic material for the preparation of semipermeable membranes applicable to microfiltration, ultrafiltration, and reverse osmosis with high thermal stability. To electrospin a hydrophilic composite coating, bio-nanoparticles, CNC, are chosen as the inorganic phase of the electrospayed particles because its high surface area, high aspect ratio, high mechanical strength, and large-scale availability. Here, the CA is mainly responsible for imparting the hydrophilicity, while the CNC is added to enhance the surface roughness required to increase the in-air hydrophilicity and underwater oleophobicity.

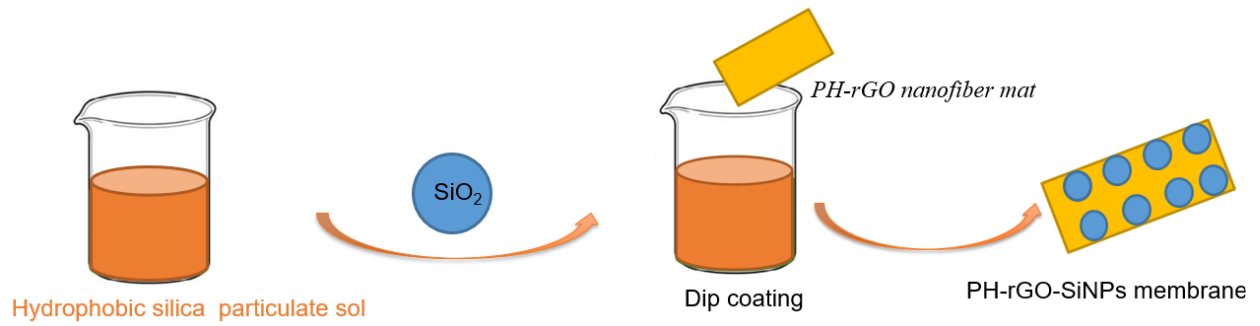


**Figure A-6.** The schematic procedure for the preparation of PH-rGO-SiNPs functionalized membrane through a dip-coating strategy. The electrospun nanofiber mat PH-rGO was immersed in the hydrophobic silica particulate solution for 36 h to affix silica nanoparticles to the membrane surface, then dried at 120 °C for 45 min after rinsing with DI water.

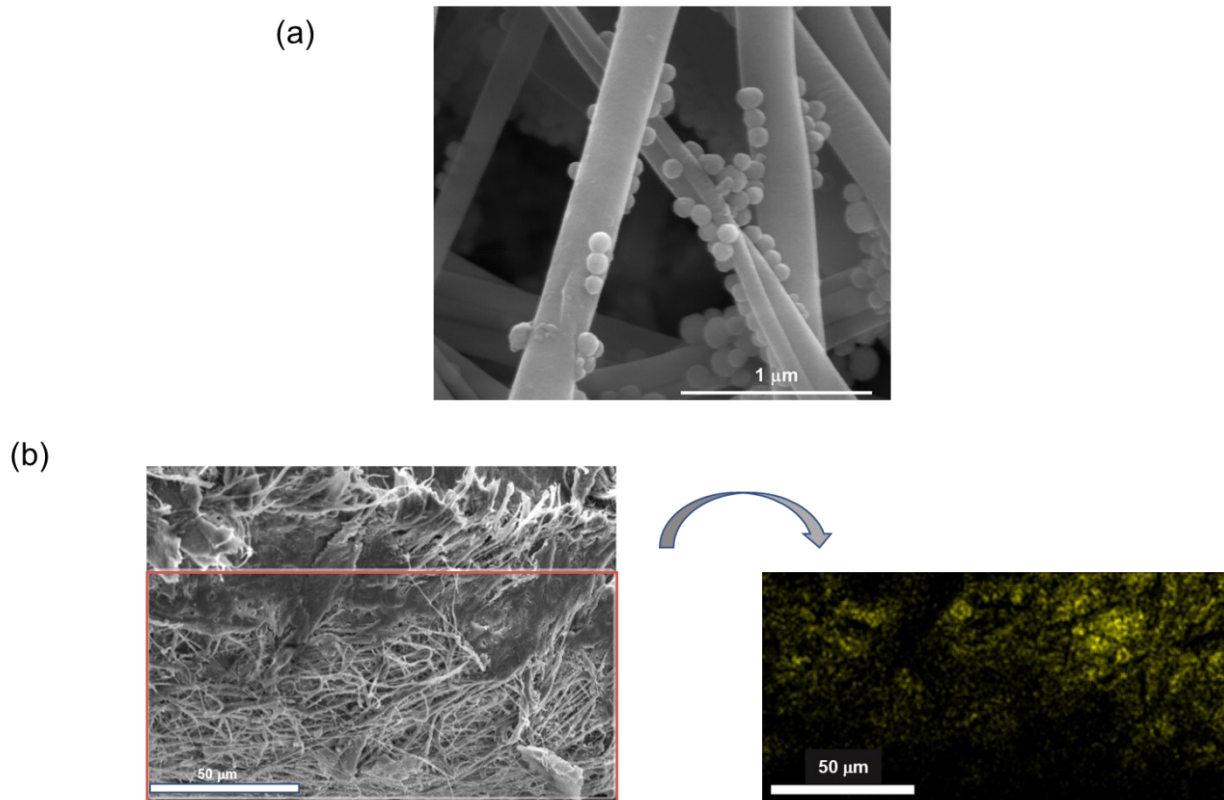


**Figure A-7.** (a) SEM images of PH-rGO-SiNPs membrane modified by hydrophobic silica particles. Nanofibers are rougher after modification with hydrophobic SiO<sub>2</sub> nanoparticles. Aggregated SiO<sub>2</sub> nanoparticles randomly distributed on the fibers, exhibiting a number of re-entrant geometries. (b) Cross-sectional EDS mapping images of Si on the PH-rGO-SiNPs membrane. Si distributed across the membrane, with the volume decreasing with depth for the PH-rGO-SiNPs membrane. The coating layers enter into the texture of the PH-rGO substrate and increases adhesion.

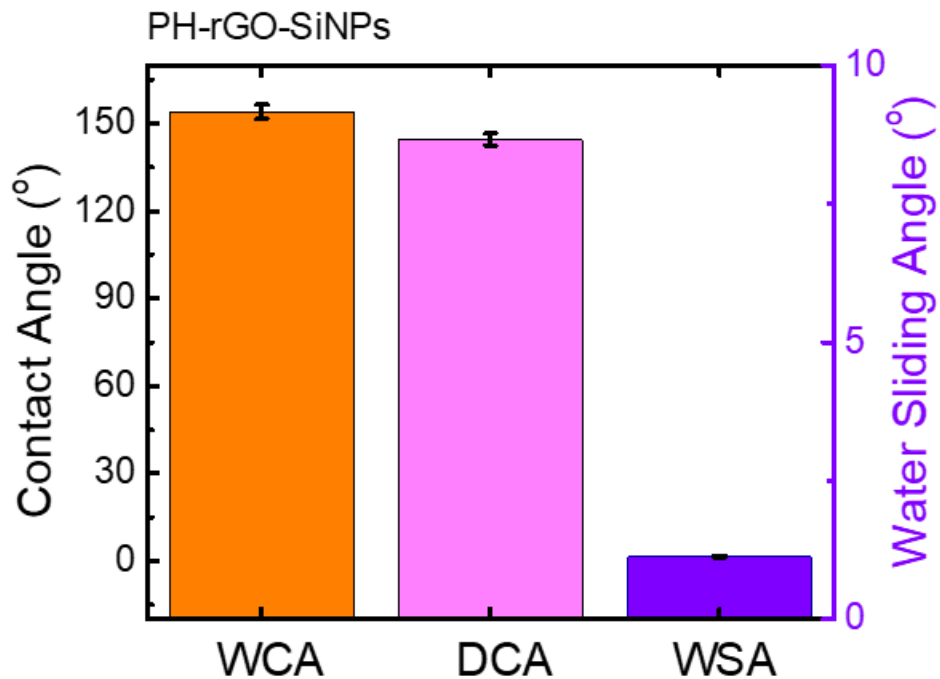


**Figure A-8.** Water contact angle (WCA), Diiodomethane contact angle (DCA), and water sliding angle (WSA) of the as-prepared PH-rGO-SiNPs membrane. Surface wettability is characterized by the static contact angle using water, diiodomethane. The value was calculated by averaging three measurements at different locations. The WCA and DCA is 154.0° and 144.5°, respectively. Moreover, it exhibited a low contact angle hysteresis with sliding angle lower than 2°.

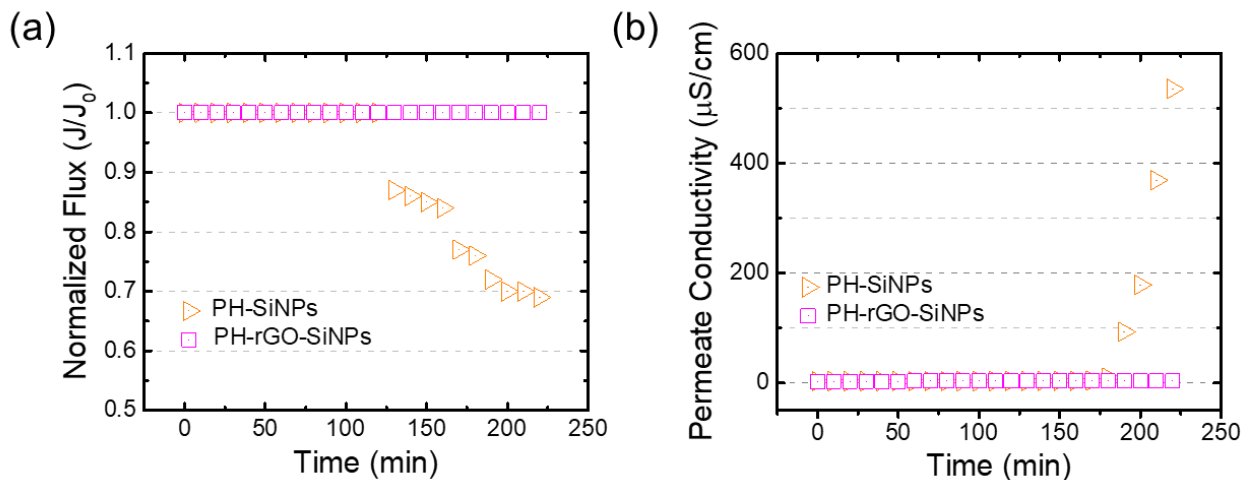


**Figure A-9.** (a) Water flux and (b) permeate conductivity of control membrane PH-SiNPs membrane (PH-SiNPs membrane was obtained by coating hydrophobic SiNPs directly on the PVDF-HFP electrospun nanofibrous mat to illustrate the influence of rGO addition into the substrate) and superamphiphobic PH-rGO-SiNPs membranes in DCMD process. 3.5 wt% NaCl with addition of 0.3 mM SDS solution was used as a feed solution maintaining at 75 °C and deionized water was used as a permeate cooling solution maintaining at 25 °C. The flow rate of feed and permeate streams were both 0.7 LPM.

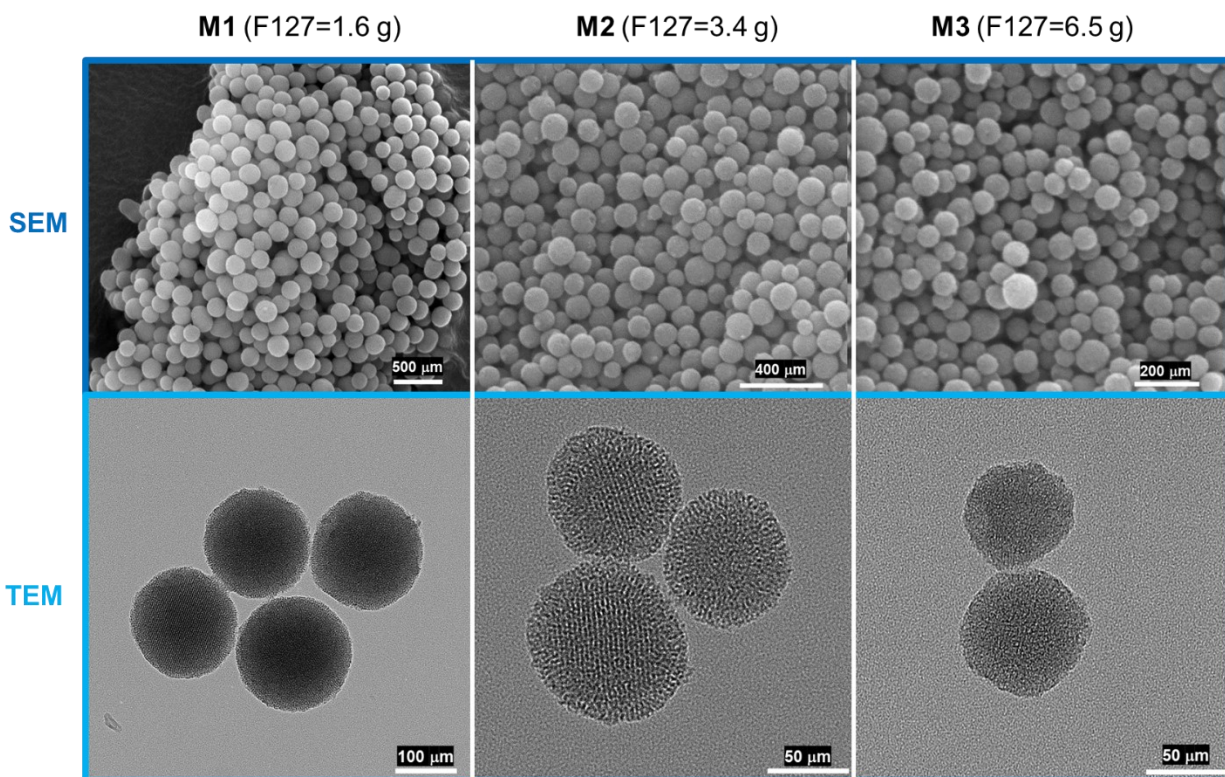


**Figure A-10.** SEM images and TEM images of prepared MCM-48 nanoparticles using various amounts of F127 as the particle dispersion agent. Through use of triblock copolymer F127 as a good dispersing agent, monodisperse MCM-48 materials without the deformation of structural properties were obtained, and the particle size was efficiently controlled in the binary surfactant system. The nonionic surfactant F127 interacts with silicates through hydrogen bonds during the assembly of silicates, which limit the growth of particle grains, resulting in different sizes of MCM-48 spheres.

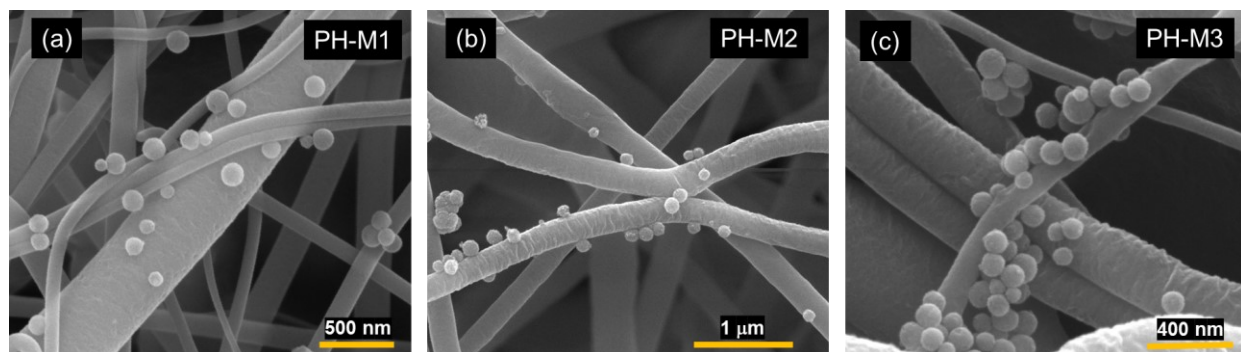


**Figure A-11.** SEM images of hybrid membranes with different sizes of MCM-48. All the hybrid membranes exhibited a surface morphology with micro/nano bumps. Hydrophobic MCM-48 nanoparticles were found randomly distributed on the fibers of the PVDF-HFP/MCM-48 hybrid membranes, with no obvious agglomeration of particles, and do not block the membrane pores.

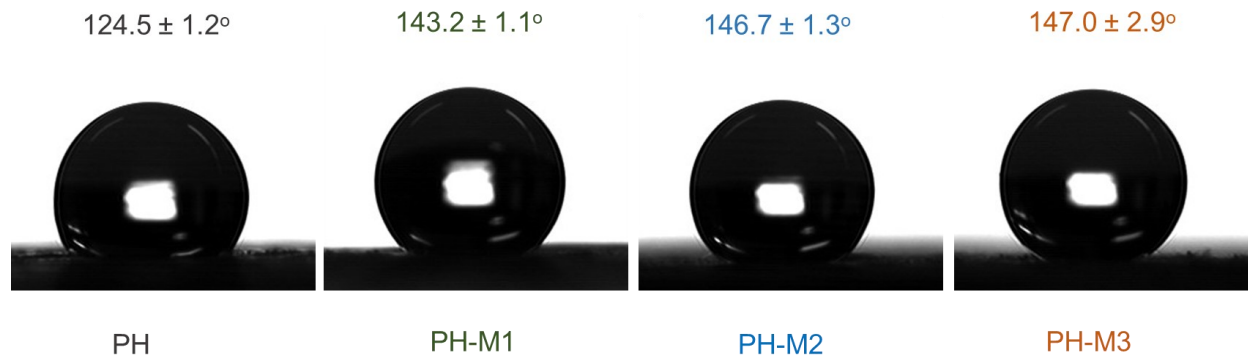


**Figure A-12.** Water contact angle of pristine and various hybrid membranes. It was observed that the addition of MCM-48 spheres promoted membrane hydrophobicity resulting from the surface geometry effect. It is possible that the micro/nanostructure evident in the hybrid membrane introduce hierarchical roughness and rendered the membrane surface more hydrophobic.

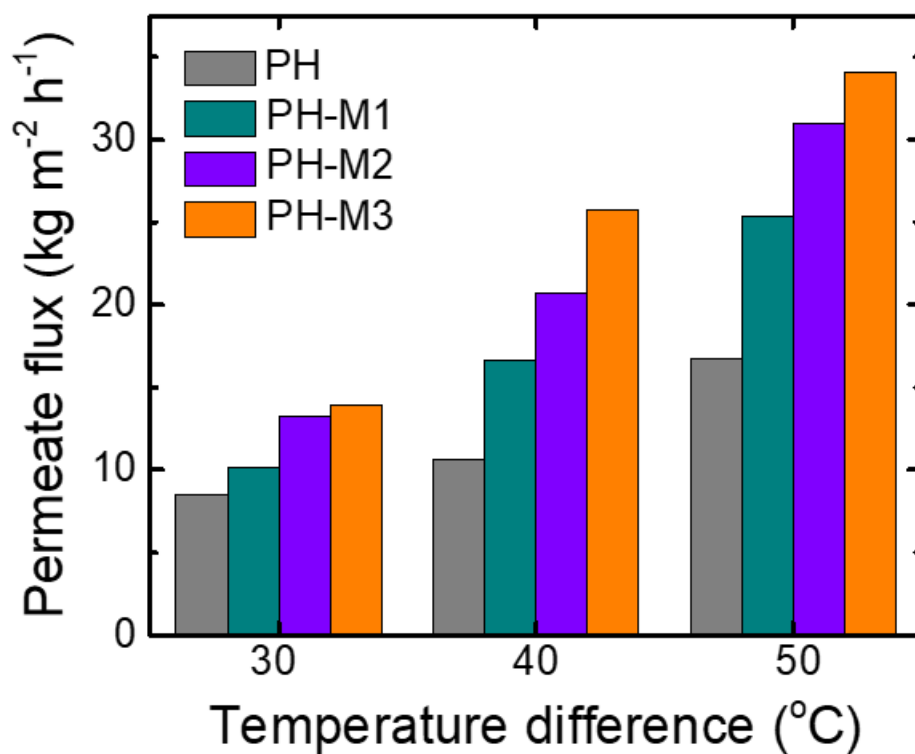


**Figure A-13.** Water flux versus temperature difference of pristine and various hybrid membranes in DCMD process. A 35 g/L NaCl solution was used as feed solution maintained at 45 °C, 55 °C, and 65 °C; deionized water was used as a permeate cooling solution maintained at 15 °C. The flow rate of feed and permeate streams were both 0.7 LPM.